Summer 2024

INVESTIGATION OF BONE STRUCTURE AND COMPOSITION DIFFERENCES IN OSTEOFIBROUS DYSPLASIA AND NEUROFIBROMATOSIS TYPE 1

Farzaneh Fereidouni
University of Texas at Arlington

INVESTIGATION OF BONE STRUCTURE AND COMPOSITION DIFFERENCES IN OSTEOFIBROUS DYSPLASIA AND NEUROFIBROMATOSIS TYPE 1

By

FARZANEH FEREIDOUNI

DISSERTATION

Submitted in partial fulfillment of the requirements

For the Degree of Doctor of Philosophy

In Materials Science and Engineering

At The University of Texas at Arlington

August 2024

Arlington, Texas

Acknowledgments

I want to express my deepest gratitude to my parents for their unwavering support and encouragement, which have shaped my life. I am also incredibly thankful for my devoted and supportive husband and my wonderful son, whose love and understanding have been crucial to my success in completing my PhD journey.

I would like to sincerely thank my advisor, Professor Harry Fred Tibbals, for his continued guidance, patience, motivation, enthusiasm, and vast knowledge during my PhD study and research. His unwavering support has been invaluable to me throughout my research and thesis writing. I am immensely grateful to him for his mentorship.

I also want to express my gratitude to Professor Efstathios Meletis, the Chair of the MSE Department, for his encouragement, insightful feedback, and guidance throughout my research. This research was supported in the last semester with a Dean's Graduate Assistantship; I would like to extend my thanks to Professor Meletis for nominating me for this award

Acknowledgment with thanks to Dr. Jonathan Rios, Professor in Eugene McDermott Center for Human Growth and Development at UT Southwestern and Scientist at Texas Scottish Rite Children's Hospital, for initiating this study, for providing necessary samples and background data, financial support for laboratory work, and advice and guidance. I also appreciate Professor Rhonda Prisby, Distinguished Professor and Kinesiology Director at the Bone Vascular Microcirculation Laboratory Department, for making the Micro-CT instrument in her department available for this study and providing invaluable time in guidance and data interpretation in Micro-CT, as well as in histology. I am very thankful to Dr. Kamal Awad for his invaluable help, generous advice, and unwavering support throughout this study.

I am also thankful to Dr. Venu G. Veranasi, Associate Professor in Bioengineering, and Dr Erika La Plante, now with the Department of Materials Science and Engineering at UC Davis, California, for being supportive and sharing their knowledge throughout my research. My sincere acknowledgment to Dr. Jeichao Jiang and Dr. Yi Shen for all the support and training at the CCMB facility. My sincere acknowledgment to William Pierce, Texas Scottish Rite Hospital for Children Research Institute, for advice on bone sample preparation and loan of diamond cutting instrument. My deepest words of appreciation to Lashonda Davis for helping me through all the official matters and for their good wishes through all five years of my graduate studies. Also, sincere acknowledgment to Engineer Cam Macisaac, from the Thermo Fisher Scientists for his continuous support and training on the Raman DXR3 instrument.

Dedication

This Dissertation is Dedicated with Love and Affection to

My Nobly Parents

“Ardeshir Fereidouni”

“Mahnaz Dehghani”

My Lovely Husband

“Farhad Dehghani”

And

My Precious Son

“Sean Amir Dehghani”

Abstract

Investigation of Bone Structure and Composition Differences in Osteofibrous Dysplasia and Neurofibromatosis Type 1

Farzaneh Fereidouni, Ph.D.

The University of Texas at Arlington, 2024

Supervising Professor: Harry F. Tibbals

Bone genetic diseases such as Osteofibrous Dysplasia (OFD) and Neurofibromatosis type 1 (NF1) present significant challenges, particularly in children, due to their effects on skeletal homeostasis. This study aims to apply advanced material analysis to elucidate the biological disparities associated with OFD and NF1 bone dysplasia and contribute to developing diagnostic protocols and remediation approaches for these and similar bone disorders.

By employing various analytical methods, including analysis of mineral-to-matrix ratio, bone mineral density, bone hardness, and micromechanical architecture, this study compares normal rat bones with those affected by OFD and NF1. The pre-clinical mouse models of these disorders investigate potential mechanisms and pathways involved in these conditions.

The findings suggest that OFD and NF1 significantly alter bone composition and mineral-to-matrix structure, leading to decreased trabecular bone score, bone mineralization, and bone mineral density. These diseases are hypothesized to involve a common mechanism related to the MEK pathway and mineral phosphate disruption. The mineral-to-matrix ratio, in combination with bone density, is proposed as a potential diagnostic marker for these diseases.

To achieve these objectives, several techniques are employed, including Micro-CT, Raman spectroscopy, Raman 2D mapping, Scanning Electron Microscopy with Energy Dispersive Spectroscopy (SEM/EDS), Micro Hardness Testing, and staining to identify abnormalities in composition and structure. We examined knockout bone which is defined as OFD and NF1 Bone. The collected data indicates that the mineral-to-matrix ratio is significantly lower in knockout mice affected by OFD and NF1, while microhardness test results show higher values in normal bones. Additionally, bone density was lower in knockout bones as compared to normal bones; furthermore, histology results

showed that the OFD knockout bones are weaker and have a higher risk of fracture compared to normal bones due to the increased percentage of empty lacunae and trabeculation of cortical bone.

This research yields three significant findings: evidence of abnormalities in apatite mineralization in OFD and NF1 knockout bones from Raman spectra, elevated inorganic mineral forms of calcium and phosphorous in OFD and NF1 knockout bones from Raman and EDS/SEM analyses, and disorganization of bone microstructure in OFD and NF1 knockout bones revealed by 2D Raman mapping. These results support reported differences in bone density and mineral-to-matrix ratios between normal, OFD, and NF1-affected bone, demonstrating the potential utility of 2D Raman for high-resolution mapping of bone microstructure.

Overall, this study provides valuable insights into the pathophysiology of OFD and NF1, offering potential diagnostic techniques for early detection and quantification of bone morphology and composition in these and similar bone diseases.

Keywords: Bone; Mineral-to-matrix Ratio; Bone Density; Raman Spectroscopy; SEM/EDS; Micro-CT; Hardness Test; Histology.

Table of Contents

Acknowledgments I
Dedication III
Abstract IV
Chapter 1 Introduction 1
1.1 Introduction 1
Chapter 2 Literature Review 6
2.1 Bone Morphology 6
2.2 Bone Components and Structure 7
2.3 Bone Histology 9
2.4 Bone Development and Mineralization 10
2.5 Bone Disease and Disorders 12
2.6 Potential Applications in Bone Research 13
2.7 Osteofibrous Dysplasia (OFD) bone disorder 14
2.8 Osteofibrous Bone Disorder in Previous Studies 15
2.9 Neurofibromatosis Type 1 (NF1) bone disorder 17
2.10 NF1 Bone Disorder in Previous Studies 18
2.11 Underlying mechanism of NF1 and possible relation to OFD 19
Chapter 3 Experimental Methods 21
3.1 Description of Animal Specimens 21
3.2 Sample Preparation 23
3.3 Micro-CT Analysis 24
3.3.1 Micro-CT Analysis in Bone 25
3.4 Raman Spectroscopy 28
3.4.1. Raman spectroscopy in bone 30
3.4.2 Characteristic Raman Peak Ratios for Mineral and Matrix 32
3.4.3 2D Raman mapping 37
3.5 Scanning Electron Microscopy 38
3.5.1 Scanning Electron Microscopy with Energy Dispersive Spectroscopy (EDS) 39
3.5.2 Scanning Electron Microscopy in Bone 40

3.5.2 Bone Elemental Composition 41
3.6 Micro Hardness Test 43
3.6.1 Vicker Hardness Test in Bone 45
3.7 Histology Staining Study 47
3.7.1 Histology in Bone 48
Chapter 4 Results and Discussion 51
4.1 Results Discussion of Micro-T Characterization 51
4.2 Result Discussion of Raman Spectroscopy Characterization 57
4.3 Results Discussion of 2D Raman Mapping 61
4.3 Result Discussion of Scanning Electron Microscopy Characterization 65
4.4 Result Discussion of Micro Hardness Test Characterization 72
4.5 Result Discussion of Histology Characterization 72
4.6 Results Summary 78
Chapter 5 Conclusion 80
5.1 Conclusion 80
References 82

List of Tables

Table 3-1. Bone samples information. 23
Table 3-2. Definition and description of 3D outcomes for bone. 28
Table 3-3. Important ratio indices derived from Raman peaks. 32
Table 3-4. Important Raman peaks from mice bone. 33
Table 3-5. Bone Elemental Composition. 41
Table 4-6. Mn/Mx Data details for femur mid-shaft diaphysis from Raman spectra. 59
Table 4-7. Average of elemental composition from EDS for Normal, OFD, and NF1 Knockout bones cross-section. 68
Table 4-8. Vicker hardness microhardness value of Normal, OFD, and NF1 Knockout bones. 72
Table 4-9. Work model diagnosis test related to NF1 Knockout bones. 78
Table 4-10. Work model diagnosis test related to OFD Knockout bones. 79

List of Figures

Figure 2-1. The two basic types of bone tissues are trabecular and Cortical.[9] 7
Figure 2-2. Structural levels of the bone from macro to sub-nanometer scale.[21] 8
Figure 2-3. A perspective of bone anatomy, histology, and cellular/molecular components.[31] 10
Figure 2-4. Endochondral ossification is the process of bone development from hyaline cartilage.[46] 12
Figure 2-5. A radiograph of the OFD in the tibia.[81] 15
Figure 2-6. Management strategies for OFD.[85] 16
Figure 2-7. Photograph of the leg of a child with NF1 with tibial pseudarthrosis and radiograph of the affected leg pictured.[117] 19
Figure 3-8. Normal, OFD, and NF1 bone samples under the microscope. 22
Figure 3-9. Whole body CT scan images showed clear differences in skeletal between normal and genetically modified NF1 mice. 22
Figure 3-10. The principal component of a microcomputed tomography scanner.[119] 24
Figure 3-11. SCANCO Medical Micro-CT 45. 26
Figure 3-12. Diagram of the Rayleigh and Raman scattering processes.[126] 29
Figure 3-13. Schematic diagram of DXR Raman microscope.[127] 30
Figure 3-14. Standard Raman spectrum of bone.[129] 31
Figure 3-15. Images of different positions along the bone were spectra taken. (Related to the OFD knockout bones) 35
Figure 3-16. Example of different positions of taken Raman spectra of femur bone cross-section. 35
Figure 3-17. Baseline subtraction method using Origin Pro software on the bone spectrum. 36
Figure 3-18. Bone spectra show areas under the peaks. 36
Figure 3-19. Example of 2D mapping area peak calculation. 38
Figure 3-20. Scheme of electron-matter interactions arising from the impact of an electron beam onto a specimen. A signal below the specimen is only observable if the thickness is small enough to allow some electrons to pass through.[139] 39
Figure 3-21. SEM/EDS Hitachi model S-3000N. 42
Figure 3-22. Measurement of impression diagonals. 44
Figure 3-23. Sample indentation during Vickers hardness testing and illustration of the two indentation diagonals d 1 and d 2.[151] 45
Figure 3-24. Leco LM AT 300 micro hardness tests. 46
Figure 4-25. Micro-CT images of whole bones of normal, OFD, and NF1 knockouts. 52
Figure 4-26.Bone Mineral Density of normal, OFD, and NF1 knockout bones. For normal vs OFD at the 0.05 level, the population means are significantly different. 52
Figure 4-27. Micro-CT images of the cortical shell thickness of midshaft of normal, OFD, and NF1 knockout bones. 53

Figure 4-28. Cortical bone parameters (Cr. Th, Cr. Density) across the midshaft of normal, OFD, and NF1 knockout bone. For normal vs OFD at the 0.05 level, the population means are significantly different. 54
Figure 4-29. Cortical bone Porosity across the midshaft of normal, OFD, and NF1 knockout bone. For normal vs OFD at the 0.05 level, the population means are significantly different. 54
Figure 4-30. Micro-CT images of trabecular norma, OFD, and NF1 knockout bones.... 54
Figure 4-31. Trabecular bone microstructure BV/TV and Trabecular N of normal to NF1 knockout bones. For normal vs OFD at the 0.05 level, the population means are significantly different. 55
Figure 4-32. Trabecular bone microstructure (Tb. Density, Tb. Th, and Tb. S) of normal and NF1 knockout bones. 56
Figure4-33.Comparison of Bone Mineral Density, Trabecular Bone density, and Cortical Bone Density of Normal, OFD, and NF1 Knockout bones..... 57
Figure 4-34. Comparison of average Mn/Mx ratio for Normal, OFD, and NF1 bones cross-section. 59
Figure 4-35. Comparison of average Carbonate to Amide I for normal, OFD, and NF1 bone cross-section. 60
Figure 4-36. Raman spectra for Normal, OFD, and NF1 bones. 60
Figure 4-37. Comparison average of Mn/Mx Ratio of Normal, OFD, and NF1 bones cross-section. 62
Figure 4-38. Comparison average of Carbonate to Amide I of Normal, OFD, and NF1 bones of cross-section. 62
Figure 4-39. 2D Raman intensity maps for Normal, OFD, and NF1 bone cross-sections. The intensity maps show; (**a, b, c**) the selected area under the microscope; (**d,e,f**) the Mn/Mx ratio 2d map; (**g,h, i**) the CO/Amide I ratio 2D map. 63
Figure 4-40. 2D Raman particle analysis identification map for Normal bones. 64
Figure 4-41. 2D Raman particle analysis identification map for OFD knockout bones.. 64
Figure 4-42. 2D Raman particle analysis identification map for NF1 knockout bones... 64
Figure 4-43. SEM Images of a) normal, b) OFD, and c) NF1 bone cross-sections. 66
Figure 4-44. Images from cortical midshaft diaphysis(a) Image of surface from OFD sample (b) Image of distinguished the cortical bone from trabecular bone of normal bone (c, d,e, f) Image of microregion of cortical bone (This SEM micrograph pores feature in the image may correspond to microanatomical and structural features, such as cells and haversian channels, osteon or osteocyte lacune) (g) Image of distinguished the cortical bone from trabecular bone (h) Image of distinguished the cortical bone from periosteum bone,(I) Image of surface of NF1 sample. 67
Figure 4-45. Average elemental composition in cortical cross-section of the femur for Normal, OFD, and NF1 bones. 68
Figure 4-46. Elemental mapping image of Normal bone 69
Figure 4-47. Elemental mapping images of OFD Knockout bone. 70
Figure 4-48. Elemental mapping images of NF1 Knockout bone. 71

Figure 4-49. Presence of empty osteocyte lacunae in cortical bone. a) Section of Normal bone. b) Section of OFD Knockout bone. 73
Figure 4-50. Cross section of Normal sample. 73
Figure 4-51. Cross-section of OFD Knockout bone (left) and higher magnification of selected area(right). (H&E Stain). 74
Figure 52.Cross-section of Normal bone. (H&E Stain) 75
Figure 4-53. Osteon, Haversian canal, and associated structures in Normal bone. (H&E Stain) 75
Figure 4-54. The fibrous lesion presented in OFD Knockout bone (left) vs Normal bone (right). 76
Figure 4-55. Trabecula bone in OFD Knockout (left) vs Normal bone (right). 76
Figure 4-56. Growth plate of OFD bone. 77
Figure 4-57. The cartilage of OFD bone. 77

Chapter 1 Introduction

1.1 Introduction

The primary objective of this research was to investigate the effects of Osteofibrous dysplasia OFD and Neurofibromatosis NF1 diseases on the composition and structure of bone in mice. Specifically, the focus was on examining the mineral-to-matrix ratio and mineral density in the bone. The underlying hypothesis was that these markers could provide insights into the impact of OFD and NF1 diseases on bone structure, which has not been fully understood in previous research. To test this hypothesis, the study involved using advanced material analysis techniques to identify any biological variances associated with OFD and NF1 bone dysplasia. Additionally, various methods were employed to analyze bone composition and to establish diagnostic protocols and indices for bone disorders. The research also sought to gain a comprehensive understanding of the micromechanical architecture, structural composition, and mineralization to contribute to potential treatment strategies. To carry out this investigation, the research team had access to genetically modified knockout bone samples from mice, knockout bones affected by OFD and NF1, as provided by the University of Texas Southwest study, enabling a direct comparison between normal and diseased (OFD, NF1) bone samples.

The study highlights the significant challenges posed by genetic disorders, especially in children, as they impact skeletal health. Children with these conditions are at a heightened risk of fractures and associated complications, including osteoporosis. Furthermore, important aspects of bone health such as microarchitecture, mineralization levels, microdamage extent, and skeletal mineral and matrix composition are not thoroughly investigated. Currently, monitoring recommendations and treatment options are available limited. Most of the published studies on OFD and NF1 are clinical, with only a few focusing on the histology and mineral disruption of these conditions.

The following specific aims are intended in this study to get a fundamental understanding of the involved mechanisms:

i. **Study the bone composition with a focus on the mineral-to-matrix ratio in normal and knockout bone.** The investigator aimed to compare the bone composition of normal bones to OFD and NF1 knockout bones. The hypothesis was that knockout bones had a lower Mineral-to-Matrix ratio compared to normal bones. The study focused on comparing Raman spectra and 2D Raman spectra of normal and knockout bones, as well as studying the SEM/EDS elemental composition differences. The goal was to quantify the Mineral-to-Matrix ratio using various techniques.

ii. **Study the bone density in normal and knockout bones.** The investigator studied the bone density of normal bones compared to knockout bones. The hypothesis is that OFD and NF1 affect bone density, with knockout bones having lower bone density and higher trabecular density, but lower cortical density compared to normal bones. Micro-CT was used to quantify these differences. The parameters analyzed will include trabecular bone microarchitecture and density, as well as cortical bone parameters.

iii. **Study the bone mechanical properties in normal and knockout bone.** Investigator studied bone properties using the Vicker hardness test to assess mineralization and composition's impact on bone hardness. The hypothesis was that knockout bones were weaker due to fewer minerals compared to normal bones. The Vicker hardness test provides accurate and repeatable results for various materials, involving the dropping of a load onto a bone surface to leave a mark.

iv. **Correlate the results to optimize a potential working model for OFD and NF1 diagnosis.** In this study, the Investigator tried to correlate results to create a model for diagnosing normal, OFD, and NF1 knockout bones. I hypothesized that combining mineral-to-matrix ratio with bone density and mechanical hardness would accurately identify OFD and NF1 knockout bones compared to normal ones. I utilized correlation techniques to combine results from Raman spectroscopy, 2D Raman spectroscopy, Micro-CT, and Vicker Hardness tests to optimize a final working model. The final model was simplified into a score table for easy application.

Bone is the primary anatomical structure comprising the human skeletal system. Functionally, it assumes a significant mechanical role in the skeleton and represents a stock of mineral salts to mobilize to maintain calcium and phosphorus homeostasis.[1] It protects several vital organs (skull, vertebrae, and rib cage). The bone provides structural and functional support for hematopoiesis through the medullary spaces it hosts.

Several classifications can be proposed to separate bone subtypes. Overall, there are five generalized varieties of human bones (long, short, flat, sesamoid, and irregular) and two architectural subtypes, cortical and trabecular bones.[2] The focus of this topic is on the different microscopic structures and components of bone.

Bone can be disrupted in different ways, resulting in various bone diseases and disorders. These include problems that can occur at or before birth, such as genetic abnormalities and developmental defects. Many genetic and developmental disorders affect the skeleton, as well as diseases such as osteoporosis and Paget's disease of bone that damage the skeleton later in life. In addition to conditions that directly affect bone, many other disorders indirectly interfere with mineral metabolism.[3] Mineral and matrix disruption in the bone can be metabolic or genetic. Metabolism bone disorders include those associated with abnormalities in minerals (i.e., calcium and phosphorous), collectively called hydroxyapatite. Changes in mineral and matrix composition can also be related to genetic alterations.

Osteofibrous dysplasia (OFD) is a rare, non-cancerous tumor that mainly affects long bones, particularly in children and adolescents. It commonly occurs in the tibia but can also affect the fibula and long bones in the arms. Most cases are asymptomatic and discovered incidentally during imaging. Symptoms, when present, may include swelling, pain, fractures, or bowing of the affected limb. OFD's cause is unknown, and treatment usually involves observation until skeletal maturity, with the possibility of bracing or surgery, if necessary [4-7]. Furthermore, NF1 is a genetic disorder with rare, severe skeletal manifestations in children, affecting about 1 in 3000 live births per year. It can lead to a high risk of fracture and osteoporosis. It affects males and females equally, with no predilection for gender, and has a higher risk of inheriting the condition from the children of anyone with NF1. Complications may include vision loss, bone fractures, nerve damage, high blood pressure, tumor development, and decreased life expectancy.[8-10]

The bone-related symptoms of OFD and NF1 include skeletal malformations and reduced bone mineral density compared to the general population. Current monitoring and treatment options are limited. Dual-energy x-ray absorptiometry (DXA) may not accurately reflect the ongoing bone changes. Discovering shared underlying mechanisms between OFD and NF1 could lead to shared treatments for both conditions.

The research plan for this study aimed to establish the baseline for normal bone mineralization and assess the available methods for characterization. The plan also involved collecting and analyzing statistical data on normal and knockout bones, comparing the analysis of normal and knockout bones, and ultimately evaluating their relationship to diseases and pathway research. This dissertation offers a unique opportunity to explore differences in mineral-to-matrix (Mn/Mx) ratio, bone mineral density, bone hardness, and content between normal and abnormal rat bones using various analytical techniques.

I conducted measurements on the leg bones of both normal and genetically modified rats using Micro-Computed Tomography (Micro-CT), Raman Laser Spectroscopy, Scanning Electron Microscopy with Energy-Dispersive Spectroscopy (SEM/EDS), and Microhardness Testing. This research is particularly novel as it marks the first instance of comparing normal rat bone's Mn/Mx ratio with a specific type of genetically modified rat bone (OFD and NF1). The genetically modified rats were obtained from a research project at Texas Scottish Rite Children's Hospital.

I used Micro-CT to determine bone mineral density and conducted Raman Spectroscopy to calculate the Mn/Mx ratio. Scanning Electron Microscopy with Energy-Dispersive Spectroscopy was used to analyze bone microstructure, and Vickers hardness tests were performed for consistency. Decalcified bone histology and a histology study were also conducted to observe bone microarchitecture. My findings showed significantly higher mineral-to-matrix content, bone mineral density, and Vickers hardness number in normal bones compared to the knockout bones.

This study developed and validated a method for preparing and characterizing bones and obtained preliminary baseline data in normal and knockout mouse femurs. Furthermore, the results consistently indicate lower minerals to the matrix in knockouts which confirms other reports suggesting lower minerals to the matrix in knockouts. Ultimately, this study is the first detection of biophysical/chemical/crystal differences in OFD and NF1-related appetites, possible confirmation of the hypothesis of pyrophosphate (PPi) accumulation.

This dissertation is divided into five chapters, and the content is described briefly as follows:

Chapter 1 Introduction

The author introduces the general theme of the research project, focusing on the main idea, specific aims, and its significance in the field of bone.

Chapter 2 Literature Review

This chapter provides a comprehensive understanding of bone composition, structure, and development, along with an investigation into OFD and NF1 diseases. It provides a thorough review of the existing knowledge on the subject.

Chapter 3 Experimental and Methods

This chapter outlines the experimental details and methodology, including information about materials, solutions, equipment, and characterization techniques.

Chapter 4 Results Discussions

This chapter presents and discusses the obtained results on determining the differences in mineral and matrix (Mn/Mx) indices for normal and knockout mice. The

outcomes show that the Mn/Mx ratio is higher in normal bones compared to OFD and NF1 knockout bones. The data also reveals that the Mn/Mx ratio is significantly lower in knockout mice, consistent with higher microhardness test results in normal bones compared to OFD and NF1 bones. Additionally, the bone density of knockout bones is lower than that of normal bones. The chapter concludes by suggesting that these combined methods could be a potential diagnostic technique for early detection and quantification of bone morphology, mineral, and matrix composition, as well as for assessing bone diseases.

Chapter 5 Conclusion

This chapter summarizes the major conclusions drawn from the acquired results.

Chapter 2 Literature Review

Bone is a rigid organ that constitutes part of the skeleton in most vertebrate animals.[11] Bone makes up about 14% of the total body weight.[12] Bones protect the various other organs of the body, produce red and white blood cells, store minerals, provide structure and support for the body, and enable mobility. Bones come in a variety of shapes and sizes and have complex internal and external structures.[13] They are lightweight yet strong and hard and serve multiple functions. In this chapter, we provide a general understanding of the bone composition, structure, and development also OFD and NF1 disease and investigate a thorough review of the available knowledge on the subject.

2.1 Bone Morphology

From a morphological perspective, bones are categorized into two major groups, namely cortical bones, and cancellous (Trabecular) bones. Cortical bones are compact bones and are responsible for providing mechanical strength, structural rigidity, and movement. They account for 80% of the mass of the bones in the human body.[11] Vascular channels occupy about 30% of the volume. The surface-to-volume ratio in cortical bone is much lower than in trabecular bone. With aging or disease, the cortex becomes more porous, thus gaining surface area but losing strength. In the long bones, increased porosity near the periosteal surface causes more loss of strength than increased porosity near the endocortical surface. Slow periosteal expansion throughout life partially compensates for this loss of strength, because the bending strength is proportional to the radius of the fourth power.[14]

Cancellous bones, also known as trabecular bones, are soft, spongy bones and are responsible for providing structural support to the cortical bones, flexibility, and weight reduction.[15,16] In the trabecular compartment, 20% of the volume is composed of bone, and the remaining space is filled with marrow and fat. The trabecular bone transfers mechanical loads from the articular surface to the cortical bone. The hydraulic properties absorb shock. The material properties of the bone compartments differ trabecular bone has lower calcium content and more water content compared to cortical bone. Trabecular bone has a large surface exposed to the bone marrow and blood flow, and the turnover

is higher than in cortical bone.[17] Resorption takes place along bone surfaces in the trabecular bone, whereas in the cortical bone, resorption tunnels through the bone itself. The endocortical surface which is exposed to the marrow as well as the solid bone often has higher bone turnover than other trabecular or cortical surfaces.[18]

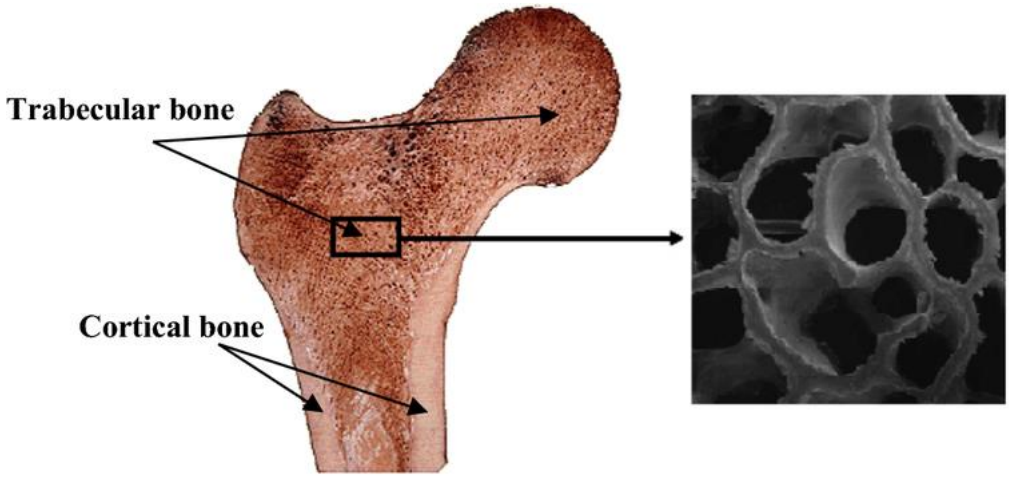

Figure 2-1. The two basic types of bone tissues are trabecular and Cortical.[19]

2.2 Bone Components and Structure

Bone is a mineralized tissue consisting of about 60% inorganic components, mainly hydroxyapatite, along with 10% water and 30% organic components, primarily proteins.[20] Because it combines inorganic and organic elements, it is one of the most rigid structures in the body.

The inorganic component of bone primarily consists of minerals, with calcium and phosphate being the most important minerals. These minerals form hydroxyapatite crystals ($Ca_{10}(PO_4)_6(OH)_2$), which are embedded in the collagen matrix. Calcium and phosphate provide hardness and much of the rigidity, providing structural strength, and they contribute to approximately 60–70% of the dry weight of bone.[20,21] Hydroxyapatite, as a vital component of the bone composition, plays an important role not only in maintaining bone structure but also in facilitating bone regeneration, especially in these two key processes: Osteo induction (refers to the mechanism responsible for the generation of new bone tissue and the conversion of immature cells into pre osteoblasts, crucial cellular units involved in the development of new bone) and Osteo conduction (refers to the ability of bone-forming cells to migrate across a bone structure and replace it with new bone tissue).[22,23]

The organic element of the bone matrix is primarily collagen, a fibrous protein that gives bone flexibility and tensile strength.[24] Collagen makes up a large portion of the

organic matrix, accounting for approximately 85 to 90% of the organic matrix of bone.[25] Collagen fibers are found in all types of connective tissue and are made up of protein collagen. These fibers are very tensile (an elongation of 10 to 20% may result in a fiber break) and flexible and can form either sparse networks of thin collagen fibrils or dense bundles depending on the function and placement. Non-collagenous proteins make up approximately 10 to 15% of the total protein content in bone.[26] These proteins play important roles in various biological processes, including mineralization, bone remodeling, cell signaling, and regulation of bone cell activity.[25]

Collagen has a triple helical structure, and specific points along the collagen fibers serve as nucleation sites for the bone mineral crystals. Bone has a complex hierarchical structure with structural integration from nm to cm.[27-29] The understanding of bone structure is developing rapidly due to improvements in available methodologies that allow unraveling structures across several length scales. These methods include advances in electron microscopy, in particular, focused ion beam scanning electron microscopy (FIB-SEM), confocal laser scanning microscopy techniques, X-ray imaging, X-ray diffraction tomography (XRD-CT), and tensor tomography (small angle X-ray scattering tensor tomography, SAXS-TT, and wide-angle X-ray scattering tensor tomography, WAXS-TT). Special emphasis is placed on the latter X-ray techniques that are emerging into powerful tools.[30] Figure 2-2 depicts the hierarchical structure of bone, which illustrates heterogeneous and anisotropic structure within a bone.

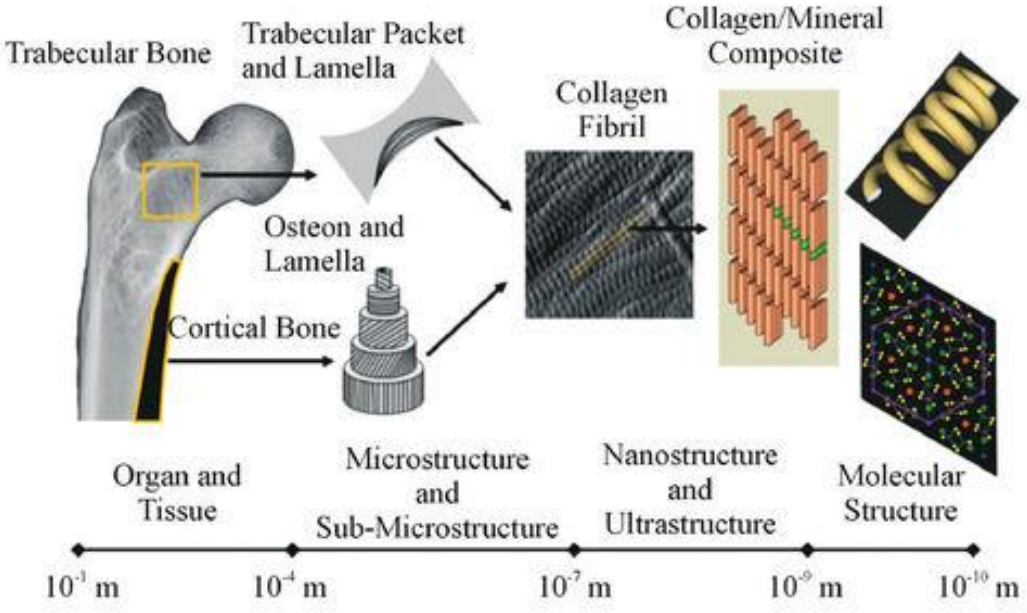

Figure 2-2. Structural levels of the bone from macro to sub-nanometer scale.[31]

Bone also contains exogenously derived proteins that may circulate in the blood and become locked up in the bone matrix itself. It is a rich source of cytokines (such as interleukin, tumor necrosis factor, and colony-stimulating factors) and growth factors (such as transforming growth factors, fibroblast growth factors, platelet-derived growth factors, and insulin-like growth factors) produced by a variety of cells associated with bone. These proteins play an important role in the biological activity of bone cells. When present within the bone, they are inactive but may become mobilized when bone is being resorbed by osteoclasts.[32]

Bone cells compose less than 2% of the bone mass, they are crucial to the function of bones.[33] Bone is composed of four different cell types: osteoblasts, osteocytes, osteoclasts, and bone lining cells. Osteoblasts, bone lining cells, and osteoclasts are present on bone surfaces and are derived from local mesenchymal cells called progenitor cells. Osteocytes permeate the interior of the bone and are produced from the fusion of mononuclear blood-borne precursor cells.[32]

2.3 Bone Histology

From a histological perspective, bone is composed of different parts. The periosteum is the most external structure present in almost all bones. It is composed of an outer fibrous layer, mainly characterized by low cell populations and a greater ECM. It could be subdivided into a highly vascularized superficial portion, mainly composed of collagen and a few elastic fibers, and a deep portion with many elastic fibers and collagen. Conversely, the inner cambium layer of the periosteum is highly cellular, with many MSCs, differentiated osteogenic progenitor cells, osteoblasts, fibroblasts, and a poor ECM.[34]

More internally, cortical (compact) bone and cancellous (trabecular) bone could be distinguished. The first represents approximately 80% of the total bone in the body, being notably stronger than the second one. Frequently, cortical bone is found in the shaft of long bones, also known as diaphysis, protecting the medullary cavity. In more detail, cortical bone is composed of osteons, which represent the structural and functional unit.[35] In contrast, cancellous bone is characterized by high porosity, which gives this structure significant mechanobiological properties.[36]

Indeed, cancellous bone responds eight times faster to changes in load and has ten times the surface/volume ratio of cortical bone.[37] In addition, cancellous bone is detected at the end of long bones, both at the metaphysis (below the growth plates) and the epiphysis (above the growth plates), where there is no medullary cavity.[38] Endosteum is an inner membrane that is notably thinner than the periosteum, revesting the bone marrow cavity, the osteons, and the trabecula near the developing part of the bone. It is an essential structure that is formed by osteoprogenitor cells and type III collagen fibers (reticular fibers).[39] Although bone marrow is considered part of the hematological rather than osseous tissue, it could also play important roles in the bone repair and regeneration

process, due to its abundance of MSCs.[40] Having integrative knowledge of bone cells and ECM components, the structures formed, and the function of each part will provide many benefits in the field of bone tissue engineering.[41] (Figure2-3)

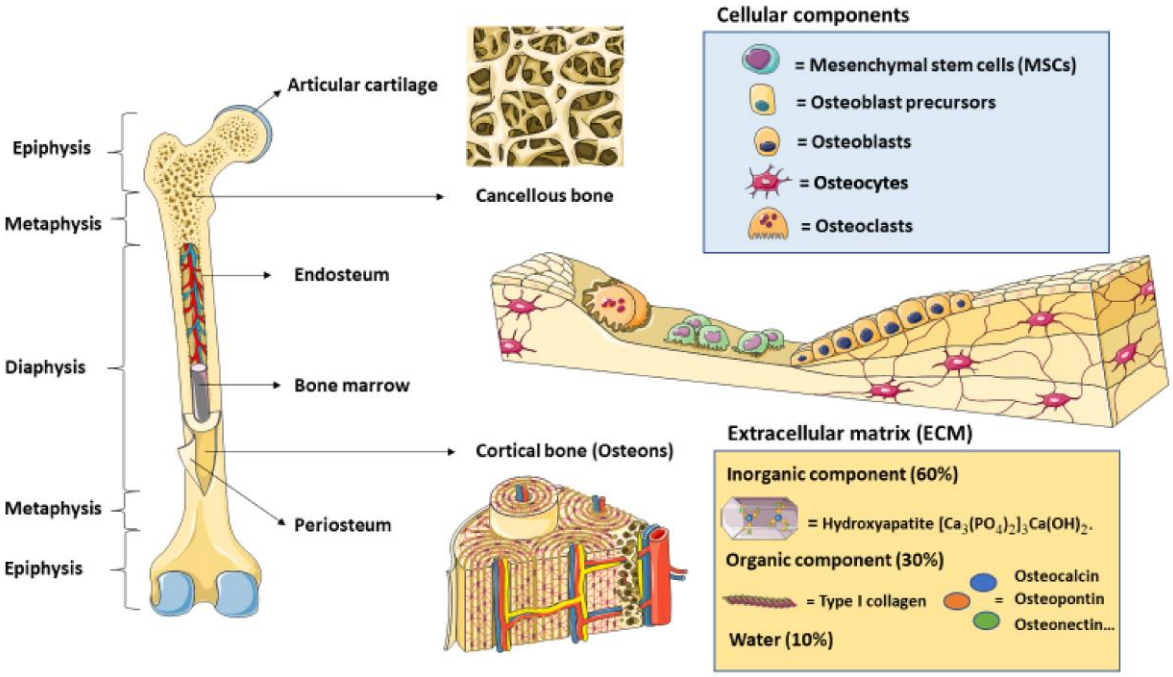

Figure 2-3. A perspective of bone anatomy, histology, and cellular/molecular components.[31]

In the above picture, the main anatomical structures of the long bones may be distinguished, including the epiphysis, metaphysis, and diaphysis, together with the main bone layers. These are, from outer to inner, periosteum, cortical bone (in diaphysis) or cancellous bone (in the epiphysis and metaphysis), endosteum, and bone marrow. The histological structure is also reviewed, with special emphasis on the cellular components, composed of mesenchymal stem cells, osteoblasts, and their precursors, osteocytes, and osteoclasts as well as the extracellular matrix, mainly formed by the inorganic element hydroxyapatite (60%) followed by the organic component (30%), prominently type I collagen although other proteins, such as Osteo nectin Osteo pontin or osteocalcin, must also be considered and water (10%).[42]

2.4 Bone Development and Mineralization

Collagen polymer underlies the structure of both cortical and trabecular bone. Collagens constitute the largest non-mineral component in bone. The mineral component is predominately hydroxyapatite (Ca10(PO4)6(OH)2), with some other salts and trace elements with important functions in the crystal lattice. During development and repair, bone formation begins with the growth of a collagen structure, into which mineral crystals are precipitated to form hard bone. In mature cortical bone, mineralized collagen fibers are organized in parallel layers (lamellar bone). In the newly formed skeleton, collagen fibers are visible under the microscope and arranged in random directions (woven bone). Their distribution during development guides the process of mineralization. Characterization at the nano level is helping the understanding of how these processes work, to guide improved healing and regeneration.[43]

Ossification, or osteogenesis, is the process of bone formation by osteoblasts. Ossification is distinct from the process of calcification; whereas calcification takes place during the ossification of bones, it can also occur in other tissues. Ossification begins approximately six weeks after fertilization in an embryo. Before this time, the embryonic skeleton consisted entirely of fibrous membranes and hyaline cartilage.[44] The development of bone from fibrous membranes is called intramembranous ossification; development from hyaline cartilage is called endochondral ossification. All the bones of the body, except for the flat bones of the skull, mandible, and clavicles, are formed through endochondral ossification. Bone growth continues until approximately age 25. Bones can grow in thickness throughout life, but after age 25, ossification functions primarily in bone remodeling and repair.[45]

Intramembranous ossification is involved in the formation of the flat bones of the skull, the mandible, and the clavicles. Ossification begins as mesenchymal cells form a template of the future bone. They then differentiate into osteoblasts at the ossification center.[44] Osteoblasts secrete the extracellular matrix and deposit calcium, which hardens the matrix. The non-mineralized portion of the bone or osteoid continues to form around blood vessels, forming spongy bone.[46] Connective tissue in the matrix differentiates into red bone marrow in the fetus. The spongy bone is remodeled into a thin layer of compact bone on the surface of the spongy bone.[47]

In long bones, chondrocytes form a template of the hyaline cartilage diaphysis. Responding to complex developmental signals, the matrix begins to calcify.[47] This calcification prevents diffusion of nutrients into the matrix, resulting in chondrocytes dying and the opening of cavities in the diaphysis cartilage. Blood vessels invade the cavities, and osteoblasts and osteoclasts modify the calcified cartilage matrix into spongy bone. Osteoclasts then break down some of the spongy bone to create a marrow, or medullary, cavity in the center of the diaphysis.[48] Dense, irregular connective tissue forms a sheath (periosteum) around the bones. The periosteum assists in attaching the bone to surrounding tissues, tendons, and ligaments. The bone continues to grow and elongate as the cartilage cells at the epiphyses divide.[49]

In the last stage of prenatal bone development, the centers of the epiphyses begin to calcify. Secondary ossification centers form in the epiphyses as blood vessels and

osteoblasts enter these areas and convert hyaline cartilage into spongy bone. Until adolescence, hyaline cartilage persists at the epiphyseal plate (growth plate), which is the region between the diaphysis and epiphysis that is responsible for the lengthwise growth of long bones.[50] (Figure 2-4).

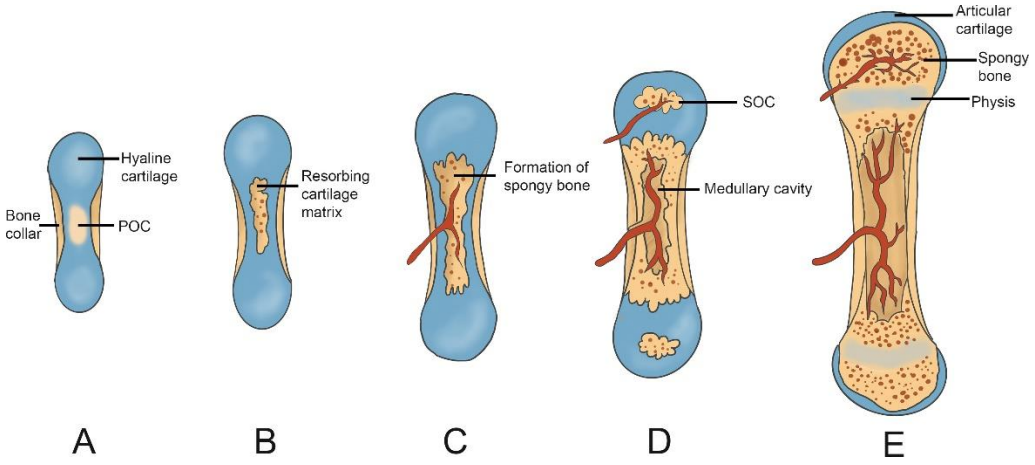

Figure 2-4. Endochondral ossification is the process of bone development from hyaline cartilage.[51]

2.5 Bone Disease and Disorders

Bone diseases and disorders are often related to the change in and function of mineral and matrix compositions. Mineral and matrix disruption in the bone can be metabolic or genetic. Metabolism bone disorders include those associated with abnormalities in minerals (i.e., calcium and phosphorous), collectively called hydroxyapatite. Changes in mineral and matrix composition can also be related to genetic alterations.

Bone and marrow contribute to the same organ in which bone and hematopoietic cells coexist and interact. Marrow and skeletal tissue influence each other, and a variety of genetic disorders directly target both, which may result in combined hematopoietic failure and skeletal malformations.[52] For instance, various forms of congenital anemias reduce bone mass and induce osteoporosis, while osteoclast failure in osteoporosis prevents marrow development, mitigating medullary cavities and causing anemia and pancytopenia. Diagnosis and management can be facilitated by understanding the pathophysiology of these conditions.[53] These diseases and disorders affect bone formation and resorption.

Despite recent progress, it is still unclear why and how these bone pathologies arise, raising uncertainty regarding optimal treatment. This thesis mainly focuses on how these modifications affect the mineral and matrix quality and quantity. Raman is an ideal technique for understanding the quality and quantity of minerals and matrix, which affect the porosity and fragility of bone. Widely used technologies like Digital X-ray Radiogram, Micro-CT, and Ultrasound analyze bone parameters. Radiation, cost, and space availability drove researchers to utilize new options such as FTIR and Raman Spectroscopy. These analysis methods are nondestructive, quick, and do not require sample preparation. Evaluation of bone quality and quantity is completed based on the mineral (Mn) to matrix ratio (Mx) (Mn/Mx), Mineral Maturity and Collagen maturity, and collagen crosslinks. The distribution of minerals over the matrix contained is a useful measure of bone quality. This study focused on the Mineral/Matrix (Mn/Mx) parameter to discriminate between normal and knockout bones.

2.6 Potential Applications in Bone Research

An active area in biomedical bone research is to learn how development, disease, and disorders affect bone failure. A goal is the elucidation of mechanisms in development and disease progression. Mechanical characterization of the bone microenvironment is recognized as important for understanding how bones function in health and disease. General relationships can be observed between clinical bone disorders and factors such as nutrition, genetics, infection, and hormone levels. A more detailed understanding of micromechanical architecture, structural composition, and mineralization may contribute to remediation approaches.[54-57]

Bone is a complex composite structure, which micro- and nano-architecture contributes to strength and resilience.[58] Components such as calcium, magnesium, phosphorous, and organic biopolymers such as collagens differ in relative abundances and distributions according to bone type and condition.[59-61] Growth-promoting and guiding proteins are important in the development, healing, and dynamic maintenance of bone's mineralized microstructures. Proteinaceous matrix polymers bind the mineral plates and halt crack propagation. Their presence contributes to an abundance of nitrogen seen in the elemental mapping of mineralized tissues.[62,63]

Trace metals can in some cases increase the resilience of crystalline lattices in the microscopic plates that make up the mineral component of bone. In addition, trace minerals and metallic elements may affect the adhesion of proteinaceous polymers to the plates, further increasing composite resilience.[64,65] Chemical composition is a necessary but not sufficient determinant of bone quality. Nevertheless, the characterization of bone at a fundamental level can start with the biochemical composition of the mineral and organic matrix.

Imaging techniques for bone such as dual-energy X-ray absorptiometry (DXA), high-resolution magnetic resonance imaging (MRI), computed tomography (CT), quantitative sonography, and texture analysis of radiographs are all capable of showing microstructure but are limited in providing information on composition.[66,67] Analysis of bone composition with Raman and other analytical techniques may contribute to the development of diagnostic protocols and indices for bone disorders. The penetration potential of Raman makes it promising for eventual clinical application to live bone.[68,69]

If we can find the same or closely related mechanism in different bone diseases, then the same treatment can be applied using the same drugs and therapy.

2.7 Osteofibrous Dysplasia (OFD) bone disorder

OFD is a benign fibro-osseous developmental condition of bone that commonly occurs in the cortical bone of the anterior mid-shaft of the tibia in children. [4] First described by Frangenheim in 1921, it is also called congenital fibrous dysplasia and ossifying fibroma of the long bones.[70] It is caused by genetic mutations, also known as pathogenic variants. Genetic mutations can be hereditary when parents pass them down to their children, or they may occur randomly when cells are dividing. Genetic mutations may also result from contracted viruses, environmental factors, such as UV radiation from sunlight exposure, or a combination of any of these.[71]

OFD was frequently found intra-cortical of the mid-shaft of the tibia, also occurs in other skeletal regions, including the fibula, ulna, radius, femur, humerus, ischium, rib, tarsus, metatarsals, vertebral, and capitate. OFD can present with asymptomatic, mass, pain, swelling, deformity, and even pathological fracture and might be misdiagnosed as adamantinoma (AD) because they are three subtypes origin from the same family of bone tumors and have similar imaging features. Moreover, pathology could provide evidence for an accurate diagnosis of OFD, but misdiagnosis may occur due to small sampling materials.[72]

OFD can be classified as monostotic, polyostotic, and McCune Albright syndrome. Most cases of monostotic lesions present with no significant symptoms and are often found incidentally on X-rays. The condition mainly affects patients in their third decade.[73] The typical radiographic findings of OFD show eccentric, well-circumscribed osteolytic lesions with a sclerotic border in the anterior cortex of the tibial diaphysis. As the tumor progresses, it shows a longitudinal spread to the metaphysis.[74] Cortical expansion and intramedullary extension may occur and can lead to an anterior bowing deformity of the tibia. While radiographic findings of OFD are well-known, magnetic resonance imaging (MRI) findings of OFD have not been fully described in the literature. The most important complication of OFD is the pathological fracture, which usually occurs after mild trauma.[75]

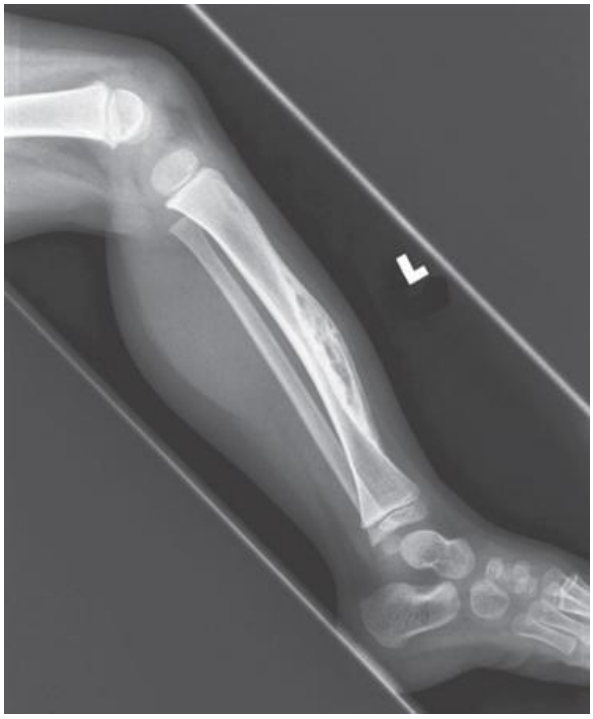

Figure 2-5. A radiograph of the OFD in the tibia.[76]

2.8 Osteofibrous Bone Disorder in Previous Studies

To date, few studies have comprehensively introduced epidemiology, clinical manifestations, pathogenesis, radiological features, pathology, and treatment for OFD. OFD is rare, and because most of the published literature is limited to case reports and small case series, definitive management recommendations are difficult to establish, and the management continues to be controversial. Because it is a benign lesion that seldom progresses during childhood and never progresses after skeletal maturity, some surgeons recommend observation without surgical intervention other than obtaining a biopsy. Bracing may be indicated to minimize deformity and prevent fracture. Surgical intervention in OFD (e.g., curettage or excision) before puberty may result in a high recurrence incidence. Surgical intervention is reserved for massive or deforming lesions or pathological fractures.[7]

The treatment for OFD-like adamantinoma is not well established due to the scarcity of cases. Careful observation and symptomatic treatment have been suggested. Surgery does not increase the risk of recurrence or the development of metastases. The aggressive nature of OFD-like adamantinoma compared to OFD is noticed not only histologically and radiologically but also clinically, especially in the degree of pain.[77] As

there is no clear evidence of progression from OFD to adamantinoma, conservative management with observation or curettage is often successful for patients with OFD and OFD-like adamantinoma. Resection with clear margins is required for patients with adamantinoma. Late tumor recurrence is not uncommon in adamantinoma, and prolonged follow-up should be considered.[77]

OFD is seen in the first or second decades of life. More than half of all the patients are under 5 years of age. Even neonates may be affected. Osteofibrous dysplasia has a characteristic natural course. The lesion grows progressively until the patient reaches the age of 15 years. After the cessation of skeletal maturation, the lesion becomes stable or may even regress spontaneously. It is infrequent to see a patient with OFD over the age of 35 years. Management should include an interprofessional team approach with clinicians, radiologists, nurses, and possibly an oncologist, to improve outcomes.[75]

OFD is a congenital disorder of osteogenesis and is typically sporadic and characterized by radiolucent lesions affecting the cortical bone immediately under the periosteum of the tibia and fibula. It was identified germline mutations in MET, encoding a receptor tyrosine kinase, that segregates with an autosomal-dominant form of OFD in three families and a mutation in a fourth affected subject from a simplex family and with bilateral disease. A mutation has been identified but the mechanism has not been fully investigated.[78]

Almost all the published studies about OFD are clinical studies and there are a few published studies about the cause histology and mineral disruption of OFD. The work by the Rios group did not test for phosphate (Rios et al in preparation, personal communication).

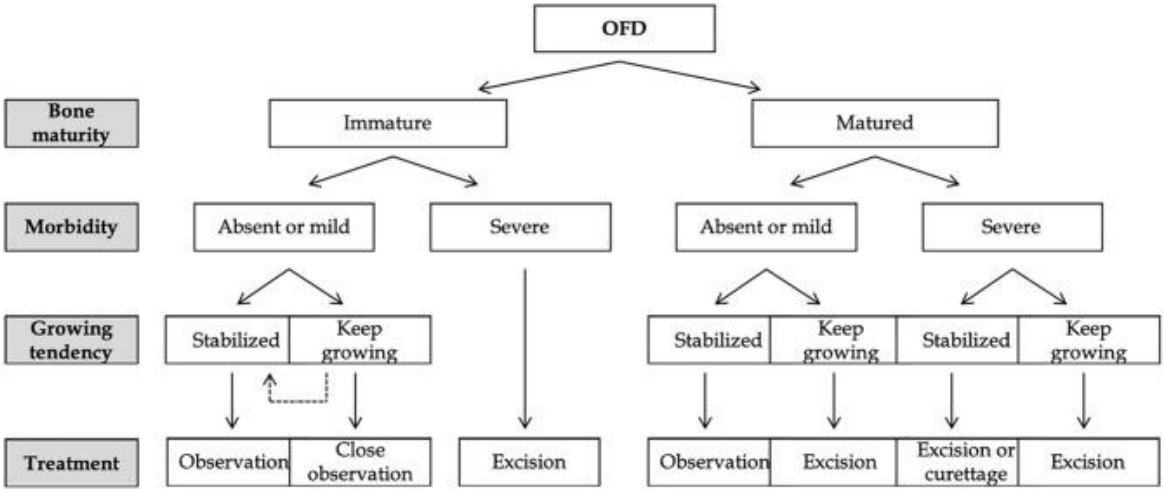

Figure 2-6. Management strategies for OFD.[79]

2.9 Neurofibromatosis Type 1 (NF1) bone disorder

NF1 is one of the inheritable neurocutaneous disorders that also harbors the risk for bone abnormalities, vasculopathy, and cognitive impairment.[80] NF1 is a complex multi-system human disorder caused by the mutation of neurofibromin 1, a gene on chromosome 17 that is responsible for the production of a protein (neurofibromin) which is needed for normal function in many human cell types.[81-83] NF1 causes tumors along the nervous system which can grow anywhere on the body. NF1 is one of the most common genetic disorders and is not limited to any person's race or sex and it is an age-specific disease; most signs of NF1 are visible after birth.[84,85]

NF1 harbingers the risk for bone abnormalities, vasculopathy, and cognitive impairment. The tibia is the bone most affected and bowing of the tibia is one of the first signs of the disease.[86] The bowing of the tibia makes it more vulnerable to a break, or fracture.[87] Often, this fracture does not heal well due to the deformity of the bone and may lead to a persistence of the fracture, known as pseudarthrosis.[88] Prevention of this sort of break is very important, as pseudarthrosis of the tibia is very difficult to treat and requires surgery. In people with NF1, histomorphometric analyses of bone biopsies have shown an overall decreased mineral content compared with age and sex-matched controls, in addition to reduced trabecular bone volume, increased osteoid volume, and increased osteoblast and osteoclast numbers.[89,90] In mice, osteoblast dysfunction following NF1 loss results in an increased generation of pyrophosphate, which inhibits bone mineral (hydroxyapatite) production and bone mineralization, causing reduced bone density and a higher risk of bone fracture.[91,92]

NF1 patients are shorter than healthy subjects: several studies highlight proportionated short stature between 8 and 15% of patients affected by NF1, thus suggesting a generalized skeleton bone growth decrease.[93-95] Previous studies, performed in NF1 patients, showed local and general dysregulation in bone resorption and remodeling[96,97] and increased formation of osteoclasts. An increased bone fracture rate was observed in NF1 adults and NF1 postmenopausal women. Reduced bone mineral density (BMD), osteoporosis, and increased fracture risk were also found in young NF1 patients.[98-100] Osteoporosis is the most common disease of bone and a major public health concern. Osteoporotic bone exhibits decreased mass, deteriorated tissue, and disrupted architecture that results in compromised strength.

In short, resorption becomes greater than formation. The diagnosis is by measuring bone mineral density (BMD) with a dual-energy X-ray absorptiometry (DEXA) scan or after a vertebral or hip fragility fracture in the absence of significant trauma. Two methods serve to calculate BMD.[101]

2.10 NF1 Bone Disorder in Previous Studies

Genetic studies during the past decades have established that bone mineralization is controlled by multiple genetic pathways, regulating the homeostasis of calcium and phosphate required for bone mineral formation. These pathways are not fully elucidated. Fully elucidating these pathways requires understanding physicochemical mineralization in organelles and its relationship with the deposition of Ca and P (Intra- and inter-cellular). The therapy for NF1 disorders will derive from understanding and controlling these pathways. Characterization of mineral distributions will aid pathway elucidation. Overall, the etiology of NF-associated skeletal manifestations remains unknown.[102-105]

Sophisticated analyses of bone minerals using Raman spectra, Fourier-transform infrared spectroscopy (FTIR), and synchrotron-generated X-ray diffraction techniques have been performed; however, a consensus on the issue is still elusive. Concerns have been raised about this latter finding on the grounds of technical limitations, including possible mineral phase transition during sample collection and processing.[106-108] The precise mechanisms underlying intracellular processes remain unclear, and they cannot be fully integrated with the extracellular mineralization mechanism and the physicochemical structure development of the mineralization particles.[109]

Research from Scottish Rite Children's Hospital indicates that NF-associated skeletal pathologies in NF1 are associated with dysregulated pyrophosphate homeostasis in adjacent NF tumors and suggests that treatment of NFs with MEK inhibitors may improve skeletal manifestations of the disease. The samples that they already used in this research will be used in this study.[110] Previous studies reported low levels of serum 25-hydroxy vitamin D3 (25OHD) and reduced bone mineral density and trabecular bone density in both adults and children NF1 patients. Although skeletal involvement in patients with NF1 is well known, and osteoporosis has been reported in adult NF1 patients, there is limited knowledge about bone metabolism in NF1 children.

The above-cited recent work [110] found evidence to support a proposed mechanism for steps in the pathway of bone formation disrupted by NF1 gene knockout. The steps in this mechanism are: 1) NF1 suppresses the formation of inorganic mineral pyrophosphate, which is a strong inhibitor of normal apatite formation. 2) Loss of NF1 (knockout) results in excess pyrophosphate, 3) which lowers mineralization in knockout bones. The pyrophosphate enrichment in the knockout would not contribute to mineral to matrix measurements by the standard Raman method, since the spectral peaks for the phosphorous are shifted. However, phosphorous and calcium would be detected in any chemical form by EDS/SEM analysis.

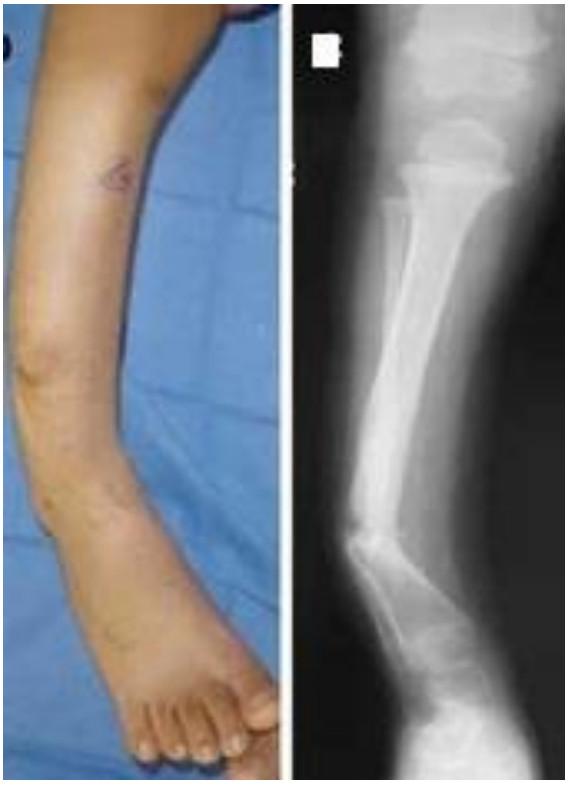

Figure 2-7. Photograph of the leg of a child with NF1 with tibial pseudarthrosis and radiograph of the affected leg pictured.[111]

2.11 Underlying mechanism of NF1 and possible relation to OFD

Individuals with neurofibromatosis type-1 (NF1) may develop a specific bone disorder that is very challenging to treat. NF1 is caused by mutations in the NF1 gene, which produces the RAS GTPase–activating protein neurofibromin. When the Nf1 gene is removed from bone-forming cells, it results in an excessive accumulation of pyrophosphate (PPi), a strong inhibitor of hydroxyapatite formation. This happens because of a constant increase in the activation of extracellular signal-regulated kinase (ERK), leading to elevated expression of Enpp1 and Ank genes, which encourage PPi production and transport. Nf1 removal also prevents osteoprogenitor differentiation, alkaline phosphatase expression, and PPi breakdown, which further contributes to PPi accumulation. Mice lacking Nf1 in bone-forming cells exhibit short stature and impaired bone mineralization and strength, but these symptoms can be improved with enzyme therapy aimed at reducing PPi concentration. These findings demonstrate the crucial role of neurofibromin in bone mineralization and suggest that imbalanced PPi levels contribute to the bone disorders seen in NF1. It also implies that some skeletal conditions associated with NF1 could potentially be prevented with medication.

We investigated the disruption of the Mn/Mx ratio in knockout bones using Raman spectroscopy. We compared the Raman peaks to identify any differences or similarities between the knockout bones and normal bones. Additionally, we calculated the changes in manganese and matrix appetite in phosphate using 2D Raman mapping. We also looked for higher total phosphate in knockout bones due to the contribution of PPi using EDS/SEM. Finally, we studied the disruption of the microstructure of the knockout bones through histology and 2D Raman mapping.

Chapter 3 Experimental Methods

The primary objective of this research is to explore the composition of both normal and genetically modified mice bone samples to identify and measure the variations in mineral-to-matrix content and bone mineral density. This in-depth study will involve utilizing cutting-edge techniques such as Micro-CT, Raman spectroscopy, Raman 2D mapping, and Scanning Electron Microscopy with Energy Dispersive Spectroscopy (SEM/EDS) to generate detailed chemical images and elemental composition maps of the bone cross sections to visualize their structural and morphological features. Additionally, Micro Hardness Testing will be conducted to assess the quality of both normal and genetically modified bone samples.

3.1 Description of Animal Specimens

The strength of bone is largely determined by the condition of the cortical bone. Analysis of excised femoral necks has revealed that the cortex contributes to 40–60% of the overall strength of the femur. Furthermore, finite element modeling has indicated that cortical bone in the femoral neck region may bear 50% of the stresses associated with normal gait. Therefore, our research focused on evaluating elemental ratio maps of the cortical bone.

Our study utilized 14 bone samples, consisting of 2 knockout bones with NF1 disorder, 8 normal bones, and 6 knockout bones with OFD bone disorder. These samples were excised femur bones from both normal and genetically altered mice (knockout). The genetically modified mice were developed as part of a research project at UT Southwestern Medical Center and Texas Scottish Rite Children's Hospital’s Research Center, to understand the causes of bone disorders in humans.

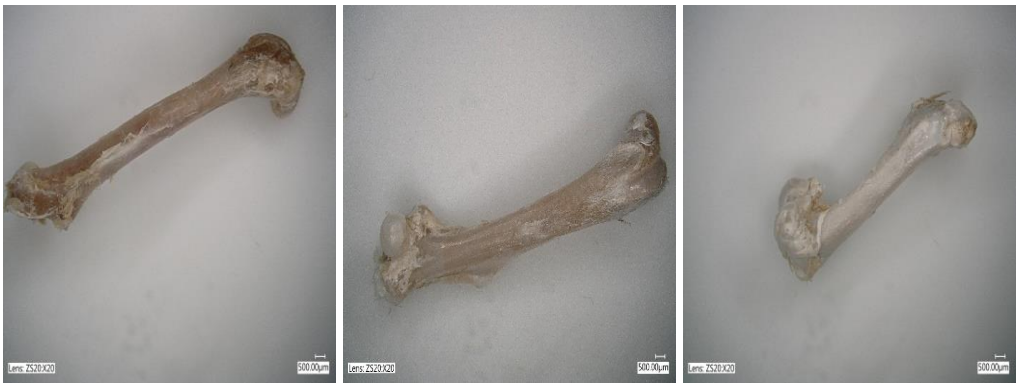

Figure 3-8. Normal, OFD and NF1 bone samples under the microscope.

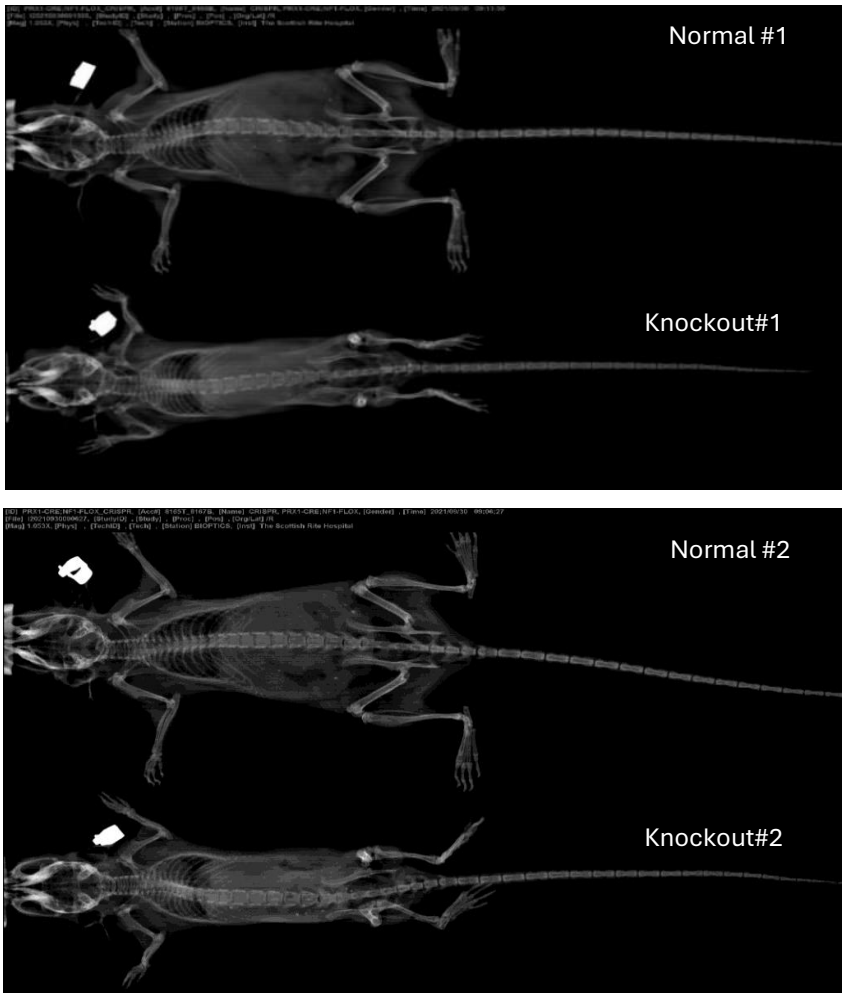

Figure 3-9. Whole body CT scan images that showed clearly differences in skeletal between normal and genetically modified NF1 mice.

Table 3-1. Bone samples information.

Sample #	Bone Type	limb	Sex	Age (Month)	Length (mm)	Bone Density (mg/cm^3)
1	Normal	Femur	Female	4	17	1050
2	Normal	Femur	Female	4	16	1069
3	Normal	Femur	Female	4	16	1044
4	Normal	Femur	Female	4	17	1062
5	Normal	Femur	Female	4	16	1073
6	Normal	Femur	Female	4	16	1059
7	Normal	Femur	Female	4	16	1081
8	Normal	Femur	Female	4	15	1075
1	OFD Knockout	Femur	Female	4	16	1021
2	OFD Knockout	Femur	Female	4	15	1002
3	OFD Knockout	Femur	Female	4	15	1020
4	OFD Knockout	Femur	Female	4	14	1027
5	OFD Knockout	Femur	Female	4	15	1018
6	OFD Knockout	Femur	Female	4	16	1024
1	NF1 Knockout	Femur	Female	4	11	984
2	NF1 Knockout	Femur	Female	4	12	982

3.2 Sample Preparation

The femur bone samples were removed from the tissue and prepared for histology after micro-CT. To ensure proper infiltration of solutions, the muscle was removed. The bones were fixed in natural buffer formalin for three days, then soaked in 70% ethanol for two days, followed by 80% ethanol for two days, 90% ethanol for two days, and finally 100% ethanol for two days, a process called dehydration. After dehydration, the samples were embedded in resin Embed-812 for preservation, easy sectioning, and stability under the electron beam. Then, the samples were sectioned with a microtome from the mid-shaft diaphysis and Metaphysis cross-section for scanning by Raman spectroscopy.

Additionally, bone slices were sputter coated with silver, following standard SEM protocol, to prepare them for high vacuum SEM.

3.3 Micro-CT Analysis

Experimental and preclinical bone and dental research has employed micro-computed tomography (Micro-CT) increasingly over the last two decades which is currently being utilized in various fields such as biomedical research, materials science, pharmaceutical medicine development and manufacturing, composites, dental research, electronic components, geology, zoology, botany, construction materials, and paper production. From a technical point of view, micro-CT indeed is a cone beam computed tomography technique that utilizes geometrically cone-shaped beams for reconstruction and back-projection processes. Micro-CT is a nondestructive technique that visualizes interior features within specimens with 3D imaging. This effective characterization method can alter the focus size from micro to macro to obtain reliable image data.[112]

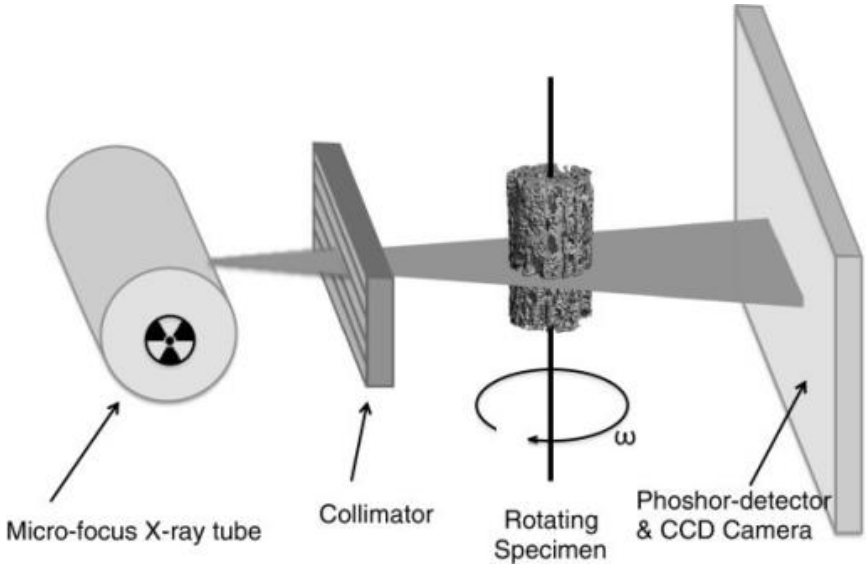

Figure 3-10.Principal component of a microcomputed tomography scanner.[113]

A micro-focus x-ray tube, or synchrotron emitter for monochromatic beam generation, produces radiation, which is collimated and passed through the object. The radiation is attenuated by the sample, and this attenuation is measured by a charge-coupled device (CCD) camera with a phosphor layer coating to convert X-rays to visible light. A three-dimensional rendering of the sample is achieved by scanning at different

angles of rotation and reconstructing through the transformation of two-dimensional projections.[113]

3.3.1 Micro-CT Analysis in Bone

Micro-CT is an X-ray imaging method capable of visualizing bone at the microstructural scale, that is, 1–100 μm resolution. It is like clinical CT but achieves higher resolution by combining a smaller field-of-view, micro-focus X-ray source, and higher resolution detector. Micro-CT is the gold-standard method for the assessment of 3D bone morphology in studies of small animals. As applied to the small bones of mice or rats, micro-CT can efficiently and accurately assess bone structure (e.g., cortical bone) and micro-structure (e.g., trabecular bone).[114]

Because bone minerals are relatively dense, they attenuate X-ray energy much more than marrow or soft tissue, and thus CT provides a clear contrast between bone and adjacent nonmineralized tissue. Likewise, bone regions of lower density have less X-ray attenuation than regions of higher density, allowing for discrimination of variations in bone mineral density. For bone micro-CT, the standard practice is that the linear attenuation is converted to mineral density based on hydroxyapatite (HA) calibration phantom, as the bone mineral is like hydroxyapatite. Thus, the units of bone mineral density (BMD) from micro-CT are [mg HA/cm3]. In summary, micro-CT attenuation values may be expressed per mille or as BMD [mg HA/cm3].[115]

In this study, the author conducted micro-CT scans under the guidance of Dr. Rhonda Prisby in her laboratory (UTA Bone Vascular and Microcirculation Laboratory). The entire femur bones were scanned ex vivo at a high resolution of 3 μm using a Scanco Micro CT 45 (SCANCO Medical AG) at 55 kV.

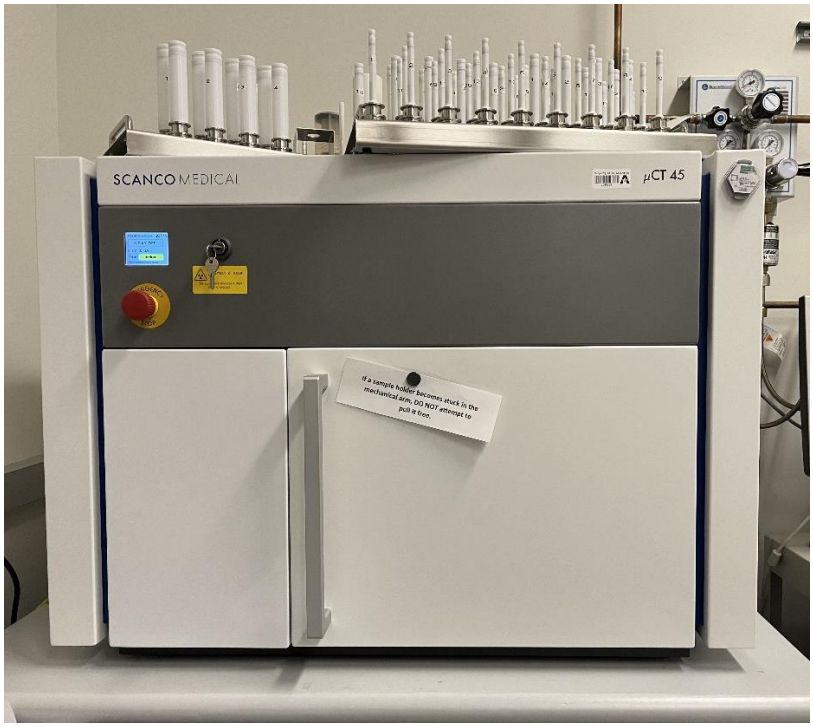

Figure 3-11. SCANCO Medical Micro-CT 45.

The decision on which morphometric indices should be reported depends largely on the research question. In long bones, it is recommended to focus on the femur because there is already a relatively large number of studies reporting results for the femur, and values for the accuracy and reproducibility of these measures have been assessed for murine femurs. Also, both trabecular and cortical parameters can be evaluated from the distal metaphysis and mid-diaphysis, respectively. The tibia is also acceptable for trabecular bone measurements at the proximal metaphysis and cortical bone measurements at the diaphysis.

The other recommended standard site is the vertebral body, which traditionally has been used for trabecular bone measurements, but it also can be used for cortical bone measurements. It is recommended to use lumbar rather than thoracic or caudal spinal segments because the volume of the lumbar vertebral bodies is the greatest, and therefore, more bone is sampled.

The minimal set of variables that should be reported for trabecular regions includes bone volume fraction (BV/TV), trabecular thickness (Tb. Th), trabecular separation (Tb. Sp), and trabecular number (Tb. N) because these can be found in most publications and also can be compared to some extent with classical histomorphometry variables. Depending on the research question, additional variables, such as the structure model index (SMI), connectivity density (Conn.D), degree of anisotropy (DA), and many others,

can be reported, but typically only variables that are critically discussed in the paper should be reported to avoid a long list of variables that are not put into perspective.

The minimal set of variables that should be reported for cortical regions includes total cross-sectional area (Tt. Ar), cortical bone area (Ct. Ar), cortical thickness (Ct. Th), and cortical bone fraction (Ct. Ar/Tt.Ar). Area moments of inertia, cortical porosity (Cortical porosity was calculated with the following equation: 1 − Ct.BV/TV. Cortical thickness and porosity examine whether the cortical shell becomes thinner and/or more porous in different types of bones, pore morphology, tissue mineral density, and other measurements also may be of interest depending on the research question and ability of the imaging approach to assess these variables accurately.

For all of the samples, normal, OFD, and NF1 knockout bones, the bone mineral density was calculated *(Figures 4-20 and 4-21)* and the following cortical bone parameters were determined from 90 slices at the femoral mid-shaft: Cortical shell thickness (μm), and cortical bone density (mg/cm^3). (*Figures 4-22 and 4-23).*

Trabecular bone microarchitecture; BV/TV (%), Tb.The [μm], Tb. N [/mm], and Tb. Sp [μm] and trabecular bone density(mg/cm3), were determined from 150 slices in the femoral metaphysis. Trabecular BV/TV allows for the assessment of bone mass, Tb. Th and Tb. N assesses the thickness and number of individual trabeculae, respectively, and Tb. Sp analyzes the distance between individuals. Alterations in Tb.Th, Tb. N, and Tb. Sp often reflects changes in BV/TV. For example, increases in Tb. Th and Tb. N often coincides with augmented BV/TV (*Figures 4-24 to 4-26*).

A one-way ANOVA analysis was used to determine statistical differences between the two types of bone samples. Data are presented as Means ± SD. Significance was defined a priori at $P \leq 0.05$. Statistical analyses were run with Origin Lab Pro software.

Table 3-2. Definition and description of 3D outcomes for bone.

Abbreviation	Variable	Unit	Description
Cr. Th	Cortical Thickness	mm	Average of cortical thickness
BV/TV	Bone volume fraction	%	The ratio of the segmented bone volume to the total volume of the region of interest
Tb. N	Trabecular number	1/mm	Measure of the average number of trabeculae per unit length
Tb.Th	Trabecular Thickness	1/mm	Mean thickness of trabeculae, assessed using direct 3D methods
Tb.Sp	Trabecular separation	mm	The mean distance between trabeculae, assessed using direct 3D methods

3.4 Raman Spectroscopy

Raman spectroscopy is one of the vibrational spectroscopic techniques used to provide information on molecular vibrations and crystal structures. This technique uses a laser light source to irradiate a sample and generates an infinitesimal amount of Raman scattered light, which is detected as a Raman spectrum.[116]

Raman spectroscopy is a scattering technique. It is based on the Raman Effect, i.e., the frequency of a small fraction of scattered radiation is different from the frequency of monochromatic incident radiation. It is based on the inelastic scattering of incident radiation through its interaction with vibrating molecules. It probes molecular vibrations.[117]

In Raman spectroscopy, a sample is illuminated with a monochromatic laser beam which interacts with the molecules of the sample and originates scattered light. The scattered light having a frequency different from that of incident light (inelastic scattering) is used to construct a Raman spectrum. Raman spectra arise due to an inelastic collision between incident monochromatic radiation and molecules of the sample. When monochromatic radiation strikes a sample, it scatters in all directions after its interaction with sample molecules. Much of this scattered radiation has a frequency that is equal to the frequency of incident radiation and constitutes Rayleigh scattering. Only a small fraction of scattered radiation has a frequency different from the frequency of incident radiation and constitutes Raman scattering. When the frequency of incident radiation is

higher than the frequency of scattered radiation, Stokes lines appear in the Raman spectrum. But when the frequency of incident radiation is lower than the frequency of scattered radiation, anti-Stokes lines appear in the Raman spectrum. Scattered radiation is usually measured at a right angle to incident radiation.[118]

Stokes-shifted Raman bands involve the transitions from lower to higher energy vibrational levels and therefore, Stokes bands are more intense than anti-Stokes bands and hence are measured in conventional Raman spectroscopy, while anti-Stokes bands are measured with fluorescing samples because fluorescence causes interference with Stokes bands. The magnitude of Raman shifts does not depend on the wavelength of incident radiation. Raman scattering depends on the wavelength of incident radiation. A change in polarizability during molecular vibration is an essential requirement to obtain the Raman spectrum of the sample. Since Raman scattering due to water is low, water is an ideal solvent for dissolving samples. Glass can be used for optical components (mirror, lens, sample cell) in Raman spectrophotometer.[119]

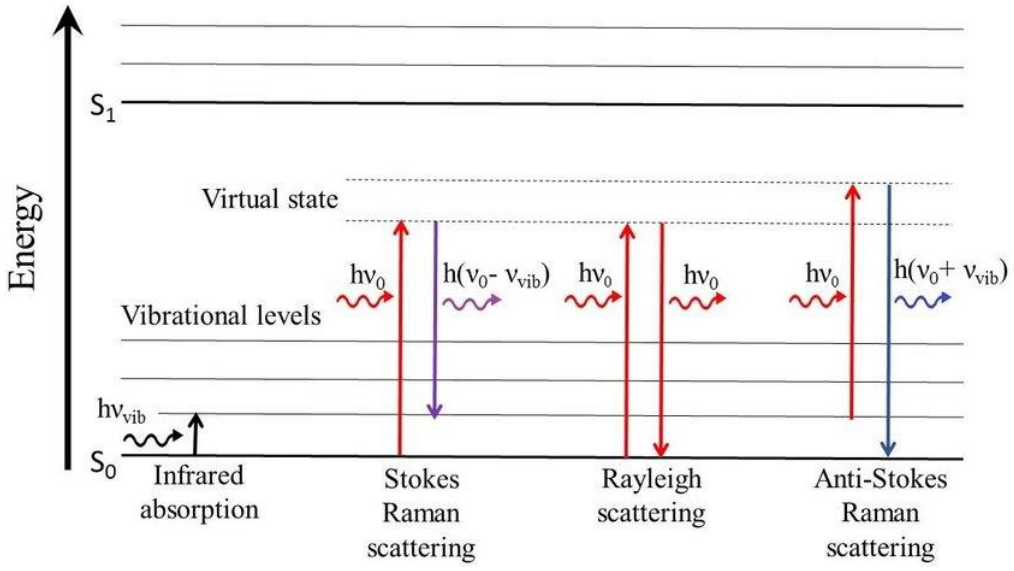

Figure 3-12. Diagram of the Rayleigh and Raman scattering processes.[120]

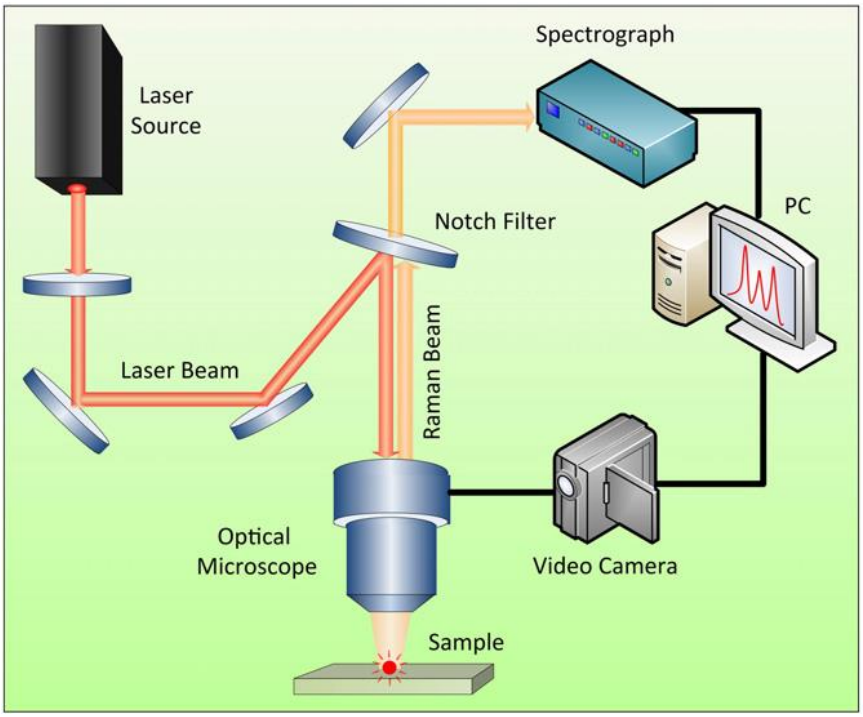

Figure 3-13. Schematic diagram of DXR Raman microscope.[121]

3.4.1. Raman spectroscopy in bone

Raman spectroscopy is increasingly commonly used to understand how changes in bone composition and structure influence tissue-level bone mechanical properties. The spectroscopic technique provides information on bone mineral and matrix collagen components and on the effects of various matrix proteins on bone material properties as well. The Raman spectrum of bone not only contains information on bone mineral crystallinity that is related to bone hardness but also provides information on the orientation of mineral crystallites concerning the collagen fibril axis.

Raman uses a selected laser excitation wavelength (conventionally denoted in nanometers = nm) and measures a resulting scattering spectrum (conventionally presented in terms of wavenumbers = cm^{-1}). With Raman, it is important to decide the right laser excitation wavelength. Because Raman scattering is an event with very low probability, other signals may obscure the Raman signal, especially from fluorescence. The efficiency of fluorescence excitation from protein and other tissue is generally higher than the efficiency of Raman scattering. So, suppressing the fluorescence signal provides significant improvement. To lessen this issue, working in a diagnostic window with excitation between 600 nm and 1100 nm is preferred. Fluorescence efficiencies are generally significantly lower in the higher end of this range. There is a tradeoff since Raman signals are also lower at longer wavelengths and other interferences come into

effect for selected index peaks. Hence, a 780 nm laser excitation was used for an optimal result.[122]

Figure 3-14 shows a standard Raman spectrum of bone which represents the inorganic and organic functional groups. Different peaks are characteristic for various entities such as PO_4^{3-}, carbonate (CO_3^{2-}), amides, praline, etc., which predominate in either organic matrix or inorganic mineral phases. In this spectral plot, the baseline has been leveled by subtraction of fluorescence signals.

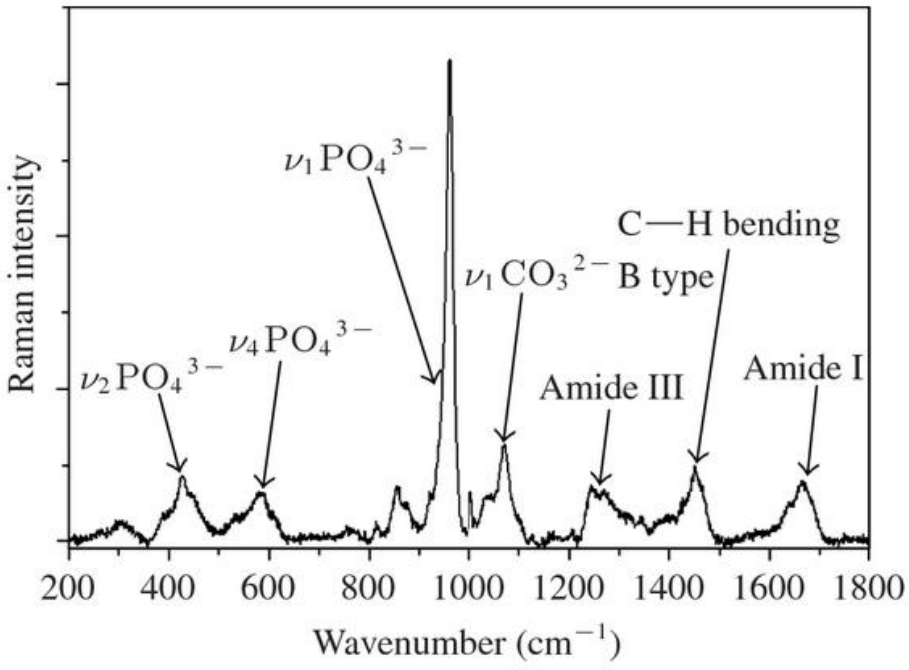

Figure 3-14. Standard Raman spectrum of bone.[123]

Here, the most intense peak is the PO_4^{3-} at 959 cm^{-1}. Some factors can alter the peak position for a few wavenumbers such as mineral carbonate (CO_3^{2-}) and monohydrate phosphate (HPO_4^{2-}). An increase in HPO_4^{2-} may result in the peak shift towards the lower wave number, which can be seen in newly deposited minerals. There is more than one peak generated by phosphates, and there are some sub-peaks as well, resulting in an intense but broader peak. The v_2 and v_4 shown in Figure 10 are substitute peaks of the phosphates. And there is one more substitute peak of phosphates obtained at 1076 cm^{-1} designated v_3. Another mineral band is the CO_3^{2-} symmetric stretch v_1 (C-O stretch) at 1070 cm^{-1}. This small difference in wavenumbers of these peaks (v_3 and v_1) leads them to overlap with each other. So, care must be taken in the process of peak fitting for accurate measurements. Similarly, as for minerals, there are different peaks for the matrix. All the amide peaks represent collagen, which makes up more than 90% of

the matrix. Amide III (C-N stretches, and N-H bends) at 1250 cm^{-1} and amide I at 1660 cm^{-1} (C=0 stretch) are due to collagen backbone vibrations. In this study, the amide I peak was chosen for matrix estimation because of its intensity and relative lack of overlap. Other studies have used the bands for proline and hydroxyproline, which fall around 855 cm^{-1} and 875 cm^{-1} respectively. The lower intensity amide III band in the region of 1250 cm^{-1} is not as useful because of overlaps.[124,125]

This standard literature spectrum from deproteinized powdered dry bone has a very flat baseline, unlike spectra of less treated bone, which has more protein. There can be a distortion that arises when more protein is present. One protein indicator is the peak at wavenumber 1450 cm^{-1} which shows the CH_2 scissoring mode, but this mode can also include contributions from other organic components.

3.4.2 Characteristic Raman Peak Ratios for Mineral and Matrix

Raman measurements are usually taken as ratios because, in a complex phase like bone, it is challenging to take absolute measurements. Raman scattering in the standard bone spectrum falls in the range between 400 cm-1 and 1700 cm^{-1} and includes peaks defining mineral and matrix content. This region excludes the C-H and N-H bonds, found in the 2900 cm^{-1} to 3300 cm^{-1} range, which give little extractable information for distinguishing between mineral and matrix.[126] four most common ratios are calculated for the different measurements of the bone. Those are 1) mineral-to-matrix Ratio (Mn/Mx); 2) carbonate (CO_3^{2-}) to phosphate (PO_4^{3-}) ratio; 3) collagen-cross link ratio; and 4) crystallinity.[127] These ratios and their significance are summarized in Table 3-2.

Table 3-3. Important ratio indices derived from Raman peaks.

Most used Raman	Calculations Ratios
Mineral to Matrix	(959- to-Pro, Hype, or 959-to-amide I) a measure of mineral content
Carbonate /phosphate	(1070-to-959) a measure of carbonate substitution in apatite lattice
Crystallinity	(inverse width 959) a measure of crystal size and/or perfection
Collagen cross-link	(1685-to-1665) a measure of collagen fibril maturity

This work was focused on the Mineral Matrix ratio (Mn/Mx) and examined the CO_3^{2-} to PO_4^{3-} ratio because it directly relates to CO_3^{2-} substitution, which may be related to aging and/or disease. The ratio of the PO_4^{3-} and amid I peak was taken to give the Mn/Mx index. The PO_4^{3-} peak is generally accepted as the measure of minerals. The competitors for amide I peaks are proline, hydroxyproline, amide III, and CH_2 deformation peaks. Some studies suggest the hydroxyproline peak for the measure of the matrix. The reason is that the hydroxyproline scattering intensity depends less on the C-C stretching frequency than the amide I and is thus more specific for the structure of collagen.[128] However, this work takes amid I, due to its higher intensity and lower overlap, to represent the matrix part of the Mn/Mx ratio. This ratio defining the mineral content is more closely proportional to ash weight.[129]

All the ratio indices can be calculated using the heights and the areas of different peaks. The current study initially used software to compute both area and height and found insignificant differences. The data in the final reported results was calculated with the software using the area ratio.

The important peaks and their wavenumber ranges are shown by arrows and described in the accompanying Table 3-4.

Table 3-4. Important Raman peaks from mice bone.

Component	Wavenumber
Phosphate	957-961 cm^{-1}
Carbonate	1070 cm^{-1}
Amide III	1246 cm^{-1}
CH2	1450 cm^{-1}
Amide I	1657-1667 cm^{-1}

For the peak measurements for the Mn/Mx index, baseline corrections were made to remove effects due to fluorescence. Fluorescence comes mostly from organic material in the matrix portion of the bone. Fluorescence can give an overly high reading for the matrix, as well as interfere with the mineral peaks through overlap.

In this study, Raman spectroscopy (Thermo Fisher DXR3) was performed on bone samples using a 780 nm excitation laser. The objective magnification was 50X, the laser power was 100 mW, and the aperture was a 25 μm pinhole. The wave number range was

between 200 and 2000 cm^-1. Preceding the spectral collection, photobleaching was conducted for one minute with a 4-second exposure time and 32 sample exposures.

Figure 3-15. Thermo Fisher DXR3 Raman Spectroscopy

We obtained Raman spectra from the cross-section of the femur mid-shaft diaphysis. We collected 16 samples in total, comprising 8 normal bones, 6 OFD knockouts, and 2 NF1 knockout bones. The femur mid-diaphysis was chosen as the most consistent site for measurement. Multiple measurements were taken at the diaphysis position on each bone sample.

Additionally, Raman laser spot spectra were captured from six closely spaced locations in the mid-diaphysis of the femur for selected bones to investigate whether this could mitigate variance by compensating for sampling error.

Figure 3-15 displays the mid-shaft diaphysis cross-section of the cortical femoral bone sample under the microscope with a 500 μm resolution. This figure also shows the 6 positions from which spectra were obtained from the cross-section of the cortical femoral bone. It's important to note that the limited number of animals measured may limit the significance of this result.

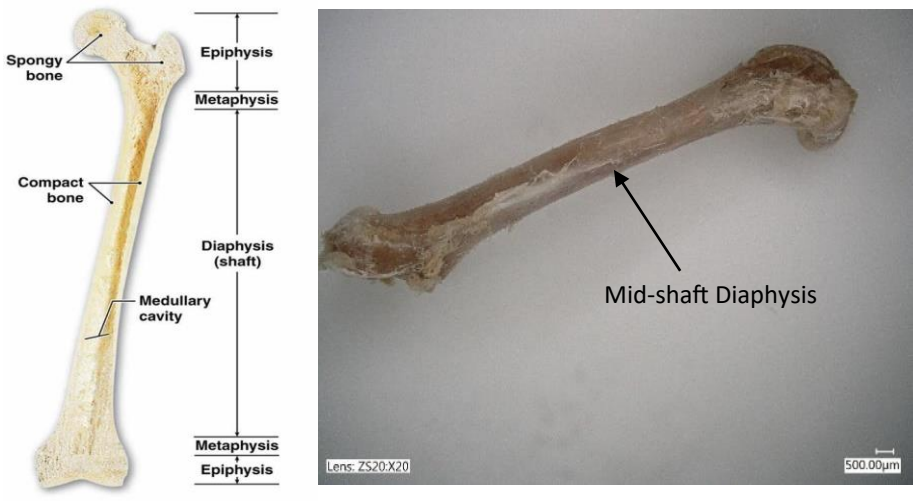

Figure 3-15.Images of different position along the bone were spectra taken. (Related to the OFD knockout bones)

Figure 3-16 displays detectable Raman signals captured at 6 different positions of the mid-shaft diaphysis cortical femoral cross-section of femur bones. In all femur samples, strong PO4-3 peaks were observed in the minerals, while a weaker Amide I signal was identified for the matrix. This aligns with the anticipated results for the highly mineralized cortical bone of the femur.

One-way ANOVAs (Origin Lab Pro) were used to determine statistical differences in the ratio of Mn/Mx for normal and knockout bones. Data are represented as mean ± SD. Significance was defined a priori at $P \leq 0.05$.

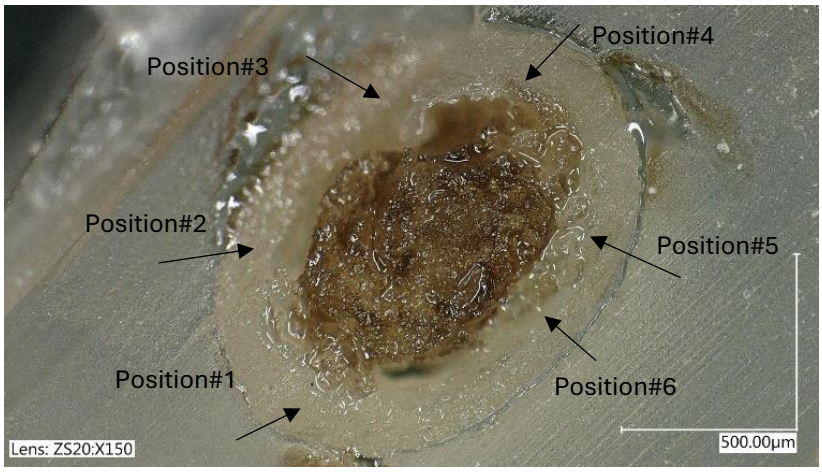

Figure 3-16. Example of different positions of taken Raman spectra of femur bone cross-section.

A baseline subtraction method was used to correct the fluorescence signal to measure the peak height and integral area under the selected Raman peaks. However,

this technique can potentially reduce the strength of the Raman organic phase signal. To ensure optimal removal of fluorescence and other noises, it is important to have a level baseline and ensure that the overall spectra conform to a standard shape. We used Origin Pro software to implement the baseline subtraction (Figure 3-17) on the spectra and obtained the corrected peak height estimate (Figure 3-18).

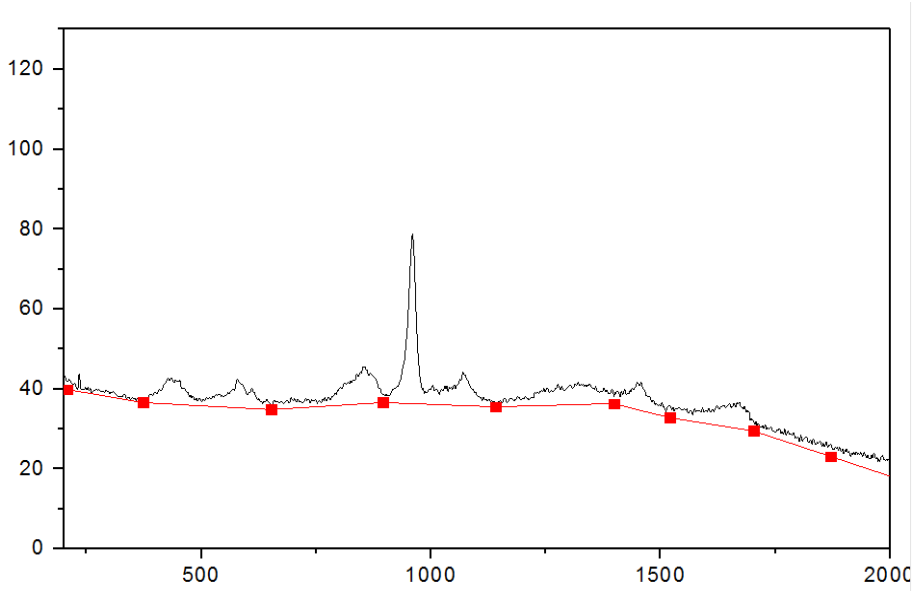

Figure 3-17. Baseline subtraction method using Origin Pro software on the bone spectrum.

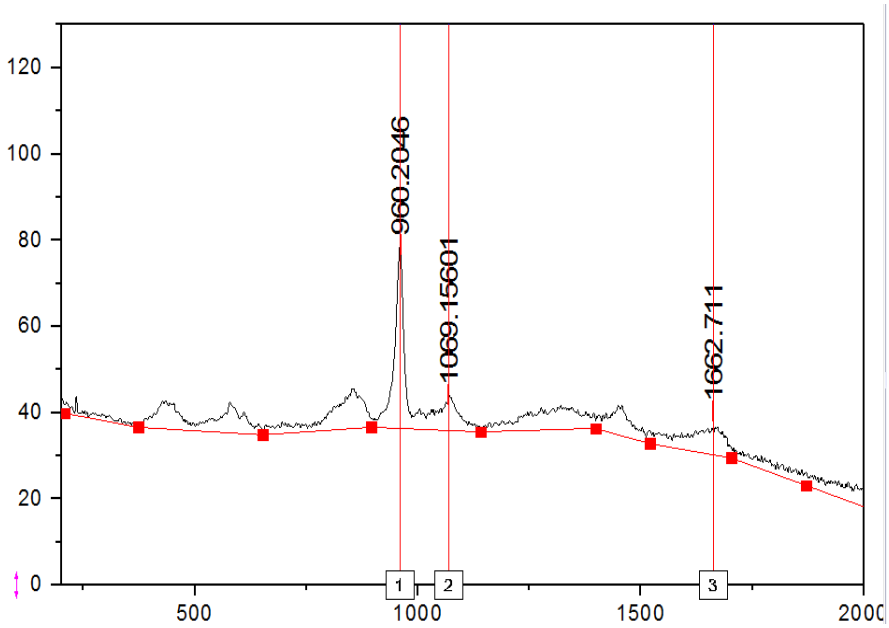

Figure 3-18. Bone spectra show areas under the peaks.

3.4.3 2D Raman mapping

Raman 2D mapping has been employed to generate detailed chemical images based on the sample's Raman spectrum, a complete spectrum is acquired at every pixel of the image and then examined to generate false color images based on materials composition and structure. Raman peak intensity images of concentration and distribution of materials. Raman peak position yields images of molecular structure and phase and material stress/strain. Raman peak width yields images of the crystallinity and phase of the material.

In this study, Raman microscopy was employed to demonstrate the accuracy of Raman spectroscopy in detecting potential differences in mineral and organic compositions between the knockout and normal specimens. Specifically, the study focused on the phosphate-to-amide I and carbonate-to-amide I ratios. The statistical analysis presented here provides valuable information about bone quality. Four cross-section samples from the mid-shaft diaphysis of femurs were used for both normal and knockout specimens. The Raman mapping technique was utilized to map the phosphate, carbonate, and amide I peaks, as well as the ratio of phosphate to amide I and carbonate to amide I. These parameters are commonly used for determining mineral and organic compositions.

Generating a Raman map can take anywhere from a couple of minutes to a couple of days, depending on the size of the area being mapped. Using a 100x objective magnification for flatter samples can significantly reduce the time required for 2D mapping collection. Additionally, eliminating the photo-bleaching time can help reduce the time required for collecting the map. For this study, 12 points were considered from each sample taken from the mid-shaft diaphysis cross-section of the cortical femur for 2D mapping, with a distance of 10 μm between each point.

The sample was placed under the Raman spectroscopy microscope, and an area of interest was selected and monitored using the Atlas window in the Raman spectroscopy software. A 2D map of the selected area was collected, and then the profile setup of the collected map was used to calculate the Mn/Mx ratio by determining the area under the peaks of mineral and matrix compositions. Figure 3-16 demonstrates how the software calculates the area under the peaks.

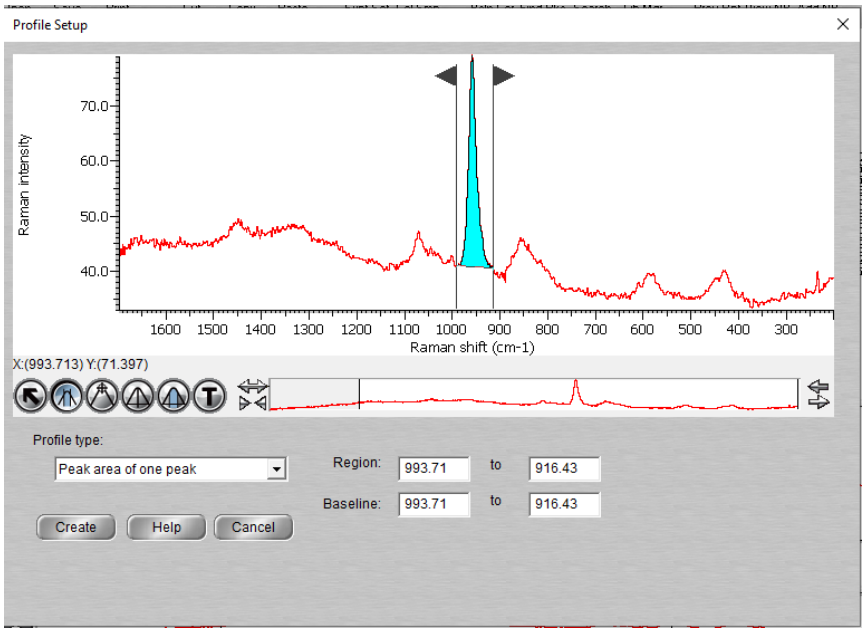

Figure 3-19. Example of 2D mapping area peak calculation.

Raman 2D mapping can calculate the Mn/Mx ratio of the samples so we do not need to calculate the ratios manually but to demonstrate how the Raman 2D mapping collected the different peaks.

3.5 Scanning Electron Microscopy

Scanning electron microscope (SEM), a type of electron microscope, designed for directly studying the surfaces of solid objects, utilizes a beam of focused electrons of relatively low energy as an electron probe that is scanned regularly over the specimen. Accelerated electrons in an SEM carry significant amounts of kinetic energy, and this energy is dissipated as a variety of signals produced by electron-sample interactions when the incident electrons are decelerated in the solid sample. These signals include secondary electrons (that produce SEM images), backscattered electrons (BSE), diffracted backscattered electrons (EBSD that are used to determine crystal structures and orientations of minerals), photons (characteristic X-rays that are used for elemental analysis and continuum X-rays), visible light (cathodoluminescence–CL), and heat. Secondary electrons and backscattered electrons are commonly used for imaging samples: secondary electrons are most valuable for showing morphology and topography on samples and backscattered electrons are most valuable for illustrating contrasts in composition in multiphase samples (i.e. for rapid phase discrimination).[130]

X-ray generation is produced by inelastic collisions of the incident electrons with electrons in discrete orbitals (shells) of atoms in the sample. As the excited electrons

return to lower energy states, they yield X-rays that are of a fixed wavelength (that is related to the difference in energy levels of electrons in different shells for a given element). Thus, characteristic X-rays are produced for each element in a mineral that is "excited" by the electron beam. SEM analysis is "non-destructive"; that is, x-rays generated by electron interactions do not lead to volume loss of the sample, so it is possible to analyze the same materials repeatedly.[131,132]

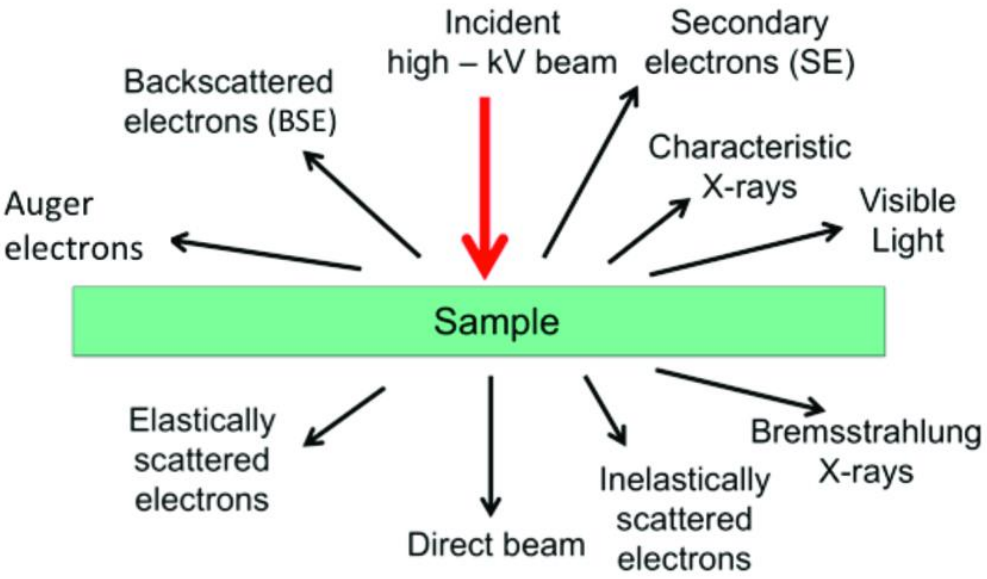

Figure 3-20. Scheme of electron-matter interactions arising from the impact of an electron beam onto a specimen. A signal below the specimen is only observable if the thickness is small enough to allow some electrons to pass through.[133]

3.5.1 Scanning Electron Microscopy with Energy Dispersive Spectroscopy (EDS)

EDS identifies the elemental composition of materials imaged in a scanning electron microscope by analyzing the energy of photons produced by X-ray fluorescence. When the scanning electron beam impacts the sample, characteristic X-rays, secondary electrons (SE), and backscattered electrons (BSE) are generated by the interaction of the electron beam with the atoms in the sample. Characteristic X-rays are used to determine the elemental composition of the sample. X-rays may be spectrally dispersed by energy or by wavelength, for identification of the contributing elements through their characteristic radiation. The X-ray fluorescence is analyzed and resolved according to the photon energy (EDS) or wavelength (WDS).

The effective working energy range of the electron beam used in electron microscopy is sufficiently high to excite inner shell electrons in the atoms of the sample under study. When an electron from another, outer, shell, fills the hole, the difference in energy between the two electron states is emitted as an X-ray with energy equal to the

difference between the two shell levels. This precise energy difference is characteristic of each elemental atomic species, so elements can be identified by their X-ray emission energies.

In EDS, the number (intensity) and energy of the emitted X-rays are measured by an energy-dispersive spectrometer. The specific spectral lines used for the analysis of elements depend on intensity, accessibility by the instrument, and lack of line overlaps.

The X-ray fluorescence photon energy used to identify specific elements is called the characteristic radiation, and varies from hundreds of eV (for first-row periodic elements C, N, O, F), to thousands of eV (for Mg, Al, Si, P, S, Ca, Fe, Zn, etc.), on up to more than ten thousand eV (for Ag, Pb, U, and a few other heavy elements).

EDS can typically yield results for all elements with an atomic number greater than boron. Most elements are detected at concentrations on the order of 0.1 percent. The composition measured is representative of atoms to a depth on the order of 10 μm, dependent on the density of the sample and the energy of the electron beam. EDS data averaged over a sample volume is plotted as a graph of X-ray photon intensity versus energy, and quantitative composition tables are produced. Additionally, an EDS image can be constructed which maps element distributions over the area of the SEM image.

3.5.2 Scanning Electron Microscopy in Bone

SEM/EDS is a well-established technique for elemental analysis, widely used in geophysics and materials science. SEM imaging of solid materials can display features as small as tens of nanometers. Combined with EDS, the technique can provide quantitative measurement of relative elemental abundances and map elemental chemical composition over an image. The SEM/EDS technique with elemental composition mapping can provide insights into the distribution of bone matrix and mineral components and differences between different states and types of bone.

Due to the complexity of bone histology, research on an index of bone strength has focused on mineral density, mineral-to-matrix ratios, structural complexity indices, and other measures, such as the FRAX® and Osteoporosis Risk Assessment Instrument (ORAI). These indices are algorithms that use mineral analysis and clinical inputs to predict fracture risk in patients. However, single average composition measurements and ratio indices have been found to have limitations in predicting bone strength and fracture risk. Thus, improved physical and imaging measurements are being sought to provide a basis for predicting bone strength. [134,135]

The relationships between BMD indices provided by DXA, bone strength, and fracture risk, have been evaluated in several studies, and additional scoring systems have been developed.[136] An additional factor is the desirability of reduction of radiation exposure involved with DXA, increasing patient safety and enabling more frequent

monitoring. Other methods that have been evaluated for clinical application include X-ray computed tomography (CT), magnetic resonance (MRI), digital X-ray radiogram (DXR), various ultrasound modalities, impedance, infrared/microwave, and photoacoustic measurements.[137-139]

Measurements of human bone from living patients with SEM/EDS would only be feasible on biopsy samples or endoscopic probes, and thus would not provide a practical alternative to non-invasive measurement modalities. However, SEM/EDS elemental morphological mapping has the potential to provide complementary guidance for interpretation of elemental analysis results from non-invasive methods such as handheld X-ray fluorescence (XRF) and photoacoustic spectroscopy.[140]

3.5.2 Bone Elemental Composition

Calcium is present throughout the vertebrate body, playing a key role in a wide range of biological functions, both as the free ion or bound in complexes. Most of the total body calcium is in the skeleton as calcium-phosphate complexes, mainly as hydroxyapatite mineral plates. The calcium in bone serves two main purposes: it contributes to skeletal strength and provides dynamic storage to maintain the intra- and extracellular calcium pools.

Table 3-5. Bone Elemental Composition.

	ELEMENT	ROLE	ABUNDANCE
Ca	Calcium	Mineral: Hydroxyapatite	Major, Predominant
P	Phosphorous	Mineral, Matrix: Phosphates, organics	Major
C	Carbon	Mineral, Matrix: Phosphates, organics	Major
N	Nitrogen	Matrix: proteins	Major
O	Oxygen	Mineral, Matrix: Phosphates, organics	Major

Bone calcium represents 99% of total body calcium in most vertebrates. Calcium is in constant and rapid exchange between bone and other calcium pools where it is involved in a wide range of essential functions. Calcium in cells and serum is regulated to a narrow concentration range, outside of which it has toxic effects. The main calcium-binding proteins include albumin and globulin in serum and calmodulin and other calcium-binding proteins in the cell. The major ionic forms in serum are calcium phosphate, calcium carbonate, and calcium oxalate.[141,142]

The SEM/EDS methods employed in this study cannot match the sensitivity and three-dimensional resolution of the intense and highly focused X-ray beams produced by synchrotron XRF; but SEM/EDS can offer a lower cost and more easily utilized complementary method to obtain trace element mapping for a wide range of elements in bone, as shown in this work.

In this study, SEM/EDS was used to demonstrate the possibility of mapping bone morphology, which can be combined with traditional microscopy to supplement histological studies. The SEM/EDS composition mapping was performed on prepared bone samples from two strains of rats with differing genetics that influence bone development.

SEM/EDS can display elemental mappings of key atomic constituents, including carbon, oxygen, nitrogen, calcium, phosphorus, magnesium, chlorine, fluorine, potassium, and sodium. It can also show trace elements such as copper, zinc, manganese, strontium, sulfur, boron, silicon, and others. The abundances and distributions of elemental components are presented in a map of bone microstructure with SEM/EDS, which may provide indications of different stages and conditions of bone development and health.

The study utilized the SEM/EDS instrument at the University of Texas at Arlington CCMB (Hitachi model S-3000N), which is a variable pressure SEM attached to a NORAN 7 integrated EDS/EBSD system. It operated using a high voltage of 20 kV and a working distance of 15 mm.

Figure 3-21. SEM/EDS Hitachi model S-3000N.

Our objective was to determine whether the levels of calcium and phosphorus in minerals and nitrogen in the bone matrix are directly linked to the data obtained from Raman spectroscopy. To achieve this, we examined 14 different samples using SEM/EDS. Since bone has low conductivity and high vacuum imaging for the best resolution requires a conductive sample, we coated the samples with silver using the sputtering process.

The initial data indicates that SEM/EDS maps can visualize the microstructure of bone, providing additional information compared to conventional grayscale SEM images. We were able to differentiate elemental composition variances in different microhistology regions and different bones.

Elements were chosen for mapping based on their ability to reveal the relative presence of minerals and matrix. Carbon and oxygen are found in both minerals and matrix. Nitrogen is more abundant in the matrix proteins. Phosphorous and calcium are predominantly present in minerals due to their presence in hydroxyapatite. Comparing the relative abundances of the selected elemental species does not rely on establishing their absolute quantities present in terms of mg/g, etc.

In an application to bone, we generated elemental composition maps from electron microscopy specimens of a cross-section of the femur. Figure 4-40 displays a micrograph image of various bone samples.

Figure 4.40 shows maps of the X-ray dispersion emission intensities for Ca (calcium), P (phosphorous), C (carbon), N (nitrogen), and O (oxygen). These images illustrate the X-ray dispersion emission intensities for the respective elements. The elemental densities correspond to the color intensity in the images.

The scale bars in the images represent 25 microns, with image magnifications ranging from 35x to 900x. The color bars on the intensity scale indicate the amplitude of the emission for each element, which is approximately proportional to the atomic concentration. The concentration relationship is not precise due to differences in emission probabilities, depth of atoms in the sample, and other effects, which can be calculated and partially compensated for in future studies. The different elemental mappings reveal aspects of the bone microstructure. Various microstructural features are displayed to varying extents in the different elemental mappings, revealing boundaries and regions that are not delineated in the grayscale micrograph images.

3.6 Micro Hardness Test

Researchers have been studying the abrasion-resistant properties of materials for centuries, but diamond scratch-testing was first introduced in the early 19th Century. This

led to the rise of the Mohs scale, which is still widely used today. As needs and requirements changed, hardness testing became much more sophisticated. Indentation hardness became the new standard, leading to a series of advanced test methods including the Brinell, Vickers, and eventually Rockwell hardness tests.

The Vickers hardness test method can also be used as a microhardness test method, mostly used for small parts, thin sections, or case depth work. Since the test indentation is very small in a Vickers microhardness test, it is useful for a variety of applications such as: testing very thin materials like foils or measuring the surface of a part, small parts, or small areas.[143]

In the Vickers hardness test, a four-sided diamond pyramid is pressed into the material. The indentation surface serves as a measure of the hardness. For the Vickers hardness test, a square base pyramid with an opening angle of 136° is used as the indenter (opening angle = angle between two opposite surfaces of the pyramid). The angle was chosen so that the Vickers hardness values are comparable to a certain degree with the Brinell hardness values (applies to approx. 400 HBW or 400 HV). The diamond pyramid is pressed into the material surface with increasing force and maintained for about 10 to 15 seconds when the desired test force is reached.[144] As with the Brinell hardness test, the ratio of test force F and indentation surface A (pyramid surface area) serves as the hardness value for the Vickers method:

$$HV=0.102\cdot F/A$$

The factor 0.102 again comes from the no longer used unit “kilopond”. The indentation surface can be determined from the diagonals of the indentation left behind. With this indentation diagonal d (in mm) and the test force F (in N), the Vickers hardness value HV is then determined as follows:

$$HV=0.1891\cdot Fd2 \quad \text{Vickers hardness}$$

The indentation diagonal d is determined by the mean value of the two diagonals d1 and d2 at right angles to each other: $d=(d1+d2)/2$

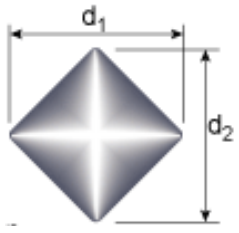

Figure 3-22. Measurement of impression diagonals.

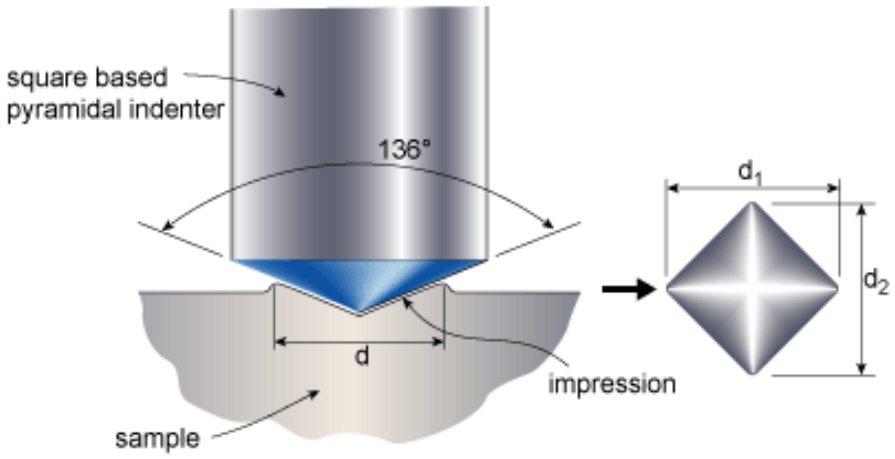

Figure 3-23. Sample indentation during Vickers hardness testing and illustration of the two indentation diagonals d 1 and d 2.[145]

3.6.1 Vicker Hardness Test in Bone

Bone hardness is one of the most important features of bone, which encompasses elastic deformation and plastic deformation. Macro hardness, microhardness, and nano hardness tests have been widely used to evaluate the properties of bone on these different scales. The macroscale mechanical properties of bone are controlled by both the structural organization of the microscale and nanoscale constituents as well as the intrinsic mechanical properties of these constituents across the different length scales8.

The Vickers hardness test is widely used and provides a convenient method for carrying out nondestructive measurements of the resistance of a material to plastic deformation9. It is believed that bone hardness measured by Vickers indentation is an important methodology for the evaluation of bone mechanical properties at the bone structural unit (BSU) level.

Some previous studies have focused on the hardness of bone. A study showed that the cortical bone hardness value was 10%–20% higher than that of trabecular bone. Another study reported similar results, in which the trabecular and cortical lamellae hardness values were measured by using nanoindentation technology. However, one study found that the hardness value of cortical bone was generally somewhat greater than that of trabecular bone, which differed from the findings of the current study. A study reported the distribution of the patellar bone hardness value. In their study, the hardness in the lateral facet and the proximal and central regions was higher than that in the medial facet and distal regions. Another investigated the hardness of the distal femur, and they demonstrated that bone hardness decreased sharply over the first two levels below the surface. Based on data obtained from one cadaver, Ohman et al. 15 found that cortical bone was harder than trabecular bone in the human radius.[146-150]

Although many studies have examined pullout strength, few studies have focused on the relationship between bone hardness and pullout strength. In addition, little is known about the relationship between bone hardness and the pullout strength of the human radius. Therefore, this study had two aims: (i) to determine whether there are certain distribution rules for the hardness and pullout strength of the radius; and (ii) to determine whether there is a positive correlation between bone hardness and screw pullout strength.

In this study, a microhardness test was performed on femur bone samples of normal and knockout mice. The cross-section of cortical bone samples was studied with microhardness tester Leco LM AT300 at the University of Texas at Arlington's Characterization Center for Materials and Biology.

Figure 3-24. Leco LM AT 300 micro hardness tests.

Measurements were taken in Vickers Hardness Number. All measurements are the average of three readings taken with different loads on the microhardness tester: 50, 100, 200, 300, and 500 gram-force. The dwell time was set to 10 seconds and a minimum distance was maintained between any two consecutive indentations. The tested sample was highly polished and flat.

3.7 Histology Staining Study

Because histology is considered the gold standard for evaluating pathology in bone disorders, we conducted a comprehensive histology profile on multiple samples of the OFD bone. This was done to establish a basis for comparison with the novel materials science evaluation methodology. Although histology was not performed on NF1 due to the small sample size, the conclusions drawn from comparing the results of OFD with 2D Raman should be similar.

Histology is the microscopic study of animal and plant cells and tissues through staining sectioning and examining them under a microscope (electron or light microscope). Various methods are used to study tissue characteristics and microscopic structures of cells. Histological studies are used in forensic investigations, autopsy, diagnosis, and education. In addition, histology is used extensively in medicine, especially in the study of diseased tissues to aid treatment. It is a series of technique processes undertaken in preparing sample tissues by staining using histological stains to aid in the microscope study.[151]

The process of histological staining takes five key stages which involve: fixation, processing, embedding, sectioning, and staining. Great changes have been made to techniques used for histological staining through chemical, molecular biology assays, and immunological techniques collectively and have facilitated greatly in the study of organs and tissues.

Decalcification is a crucial step in preparing calcified tissues like bone for histological examination. The key differences between calcified bone in histology are:

Calcified Bone

- Contains calcium salts and minerals, making it extremely hard and difficult to section.
- Cellular and structural details are obscured by the mineral content.
- Cannot be sectioned properly for microscopic examination without decalcification.
- Sectioning calcified bone can damage microtome knives and blades.

Decalcified Bone

- Calcium salts and minerals are removed through a chemical process using acids or chelating agents like Ethylenediamine tetraacetic acid (EDTA).
- Becomes soft and pliable, allowing thin sections to be cut for microscopic examination.
- Cellular details like osteocytes, osteoblasts, and osteoclasts become visible after decalcification
- Structural details like trabecular patterns, haversian canals, and canaliculi can be observed clearly.

- Preserves organic components like collagen while removing inorganic minerals.
- Allows proper staining and histochemical analysis of the tissue sections.

The choice of decalcifying agent (acid or EDTA) depends on factors like the degree of calcification, tissue type, and whether molecular studies are required later. Acids like nitric acid or formic acid decalcify rapidly but may damage cellular details, while EDTA is slower but better preserves nucleic acids for molecular testing. Decalcification removes minerals from calcified tissues like bone, transforming them into softened states suitable for high-quality histological examination and analysis while preserving cellular and structural integrity.

Staining highlights the important features of the tissue as well as enhances the tissue contrast. It is widely used in histopathology and diagnosis, as it allows for the identification of abnormalities in cell count and structure under the microscope. Hematoxylin is a basic dye that is commonly used in this process and stains the nuclei giving it a bluish color while eosin (another stain dye used in histology) stains the cell's nucleus giving it a pinkish stain. However, there are other several staining techniques used for cells and components. Staining is a commonly used medical process in the medical diagnosis of tumors in which a dye color is applied on the posterior and anterior border of the sample tissues to locate the diseased or tumorous cells or other pathological cells. In biological studies, staining is used to mark cells and to flag nucleic acids, proteins, or gel electrophoresis to aid in the microscopic examination. In some cases, various multiple staining methods are used such as differential staining, double staining, or multiple staining.[152-156]

3.7.1 Histology in Bone

Hematoxylin and eosin stain (often abbreviated as H&E stain or HE stain) is one of the principal tissue stains used in histology. It is the most widely used stain in medical diagnosis and is often the gold standard. For example, when a pathologist looks at a biopsy of a suspected cancer, the histological section is likely to be stained with H&E. The H&E staining procedure is the principal stain in histology in part because it can be done quickly, is not expensive, and stains tissues in such a way that a considerable amount of microscopic anatomy is revealed and can be used to diagnose a wide range of histopathologic conditions. The results from H&E staining are not overly dependent on the chemical used to fix the tissue or slight inconsistencies in laboratory protocol, and these factors contribute to its routine use in histology.[157-159]

H&E staining does not always provide enough contrast to differentiate all tissues, cellular structures, or the distribution of chemical substances, and in these cases, more specific stains and methods are used. There are many ways to prepare the hematoxylin solutions (formulation) used in the H&E procedure, in addition, there are many laboratory protocols for producing H&E-stained slides, some of which may be specific to a certain

laboratory. Although there is no standard procedure, the results by convention are reasonably consistent in that cell nuclei are stained blue, and the cytoplasm and extracellular matrix are stained pink. Histology laboratories may also adjust the amount or type of staining for a particular pathologist. Most cellular organelles and extracellular matrix are eosinophilic, while the nucleus, rough endoplasmic reticulum, and ribosomes are basophilic.[160,161]

After tissues have been collected (often as biopsies) and fixed, they are typically dehydrated and embedded in melted paraffin wax, the resulting block is mounted on a microtome and cut into thin slices. The slices are affixed to microscope slides at which point the wax is removed with a solvent and the tissue slices attached to the slides are rehydrated and are ready for staining. It is two stains done in subsequent steps. Hematoxylin is a basic dye that stains acidic structures. The resulting color is a purple/blue hue, and structures that are targeted with this dye are named Basophilic. Basophilic structures include DNA in cell nuclei, RNA in ribosomes, and the rough endoplasmic reticulum. Eosin is a counterstain done after hematoxylin and is an acidic dye that targets basic structures. The resulting color is a pink/red hue, and structures that attract eosin are called eosinophilic.[1] The cytoplasm is an example of an eosinophilic structure. In this study, we preferred to use H&E staining due to the capability of this staining for routine diagnosis of bone studies.[162]

The strength, shape, and stability of the human body are dependent on the musculoskeletal system. The most robust aspect of this unit is the underlying bony architecture. Bone is a modified form of connective tissue that is made of extracellular matrix, cells, and fibers. A high concentration of calcium and phosphate-based minerals throughout the connective tissue is responsible for its hard calcified nature. The histological structure, mode of ossification, cross-sectional appearance, and degree of maturity influence the classification of bony tissue.[163,164]

The best way to thoroughly observe the microarchitecture of bone is to perform decalcified bone histology, which can reveal the mineralized and cellular components of the bone as well as patterns regarding the physiological processes of bone formation and resorption. This process, in turn, allows for histological techniques such as fluorochrome analysis and histomorphometry to further probe and observe the specimens. By examining a thin slice of bone tissue under a microscope, colorized with special staining techniques, you see that these seemingly simple bones are a complex microworld containing an array of structures with various functions.[165]

At histology, OFD is characterized by the presence of osteoid tissue, fibrous tissue, and a small number of epidermoid cells. An immunohistochemical essay is mandatory in some cases to detect epidermoid cells, which are not visible on standard hematoxylin and eosin (H & E) because of their small number. OFD is characterized by a loose, often storiform fibrous background containing spicules of woven bony trabeculae lined by a layer of osteoblasts. Although this histologic appearance is quite like fibrous dysplasia (hence, their similar names), fibrous dysplasia typically lacks the distinctive osteoblastic

rimming of the bony trabeculae. Additionally, OFD demonstrates a zonal architecture, in which more immature woven bone trabeculae are located centrally. However, moving outwards toward the periphery of the lesion, the trabeculae become more numerous, larger, and more mature and lamellar.[7]

Due to the challenging nature of decalcifying resin-embedded samples and the limited number of NF1-related samples, we were only able to conduct histological studies on OFD samples. We used a total of 12 samples - six normal and six OFD samples - for this purpose.

The bones were fixed in 10% neutral buffered formalin for 3 days, with daily solution changes. Subsequently, the samples were transferred to phosphate-buffered saline (PBS) for a day to wash off the buffer. The bones were then placed in a 14% EDTA solution for 2 weeks, with the solution being changed every three days for the decalcification process. To prepare 150ml of 14% EDTA solution, 30 grams of EDTA disodium salt dihydrate was mixed with 150ml of distilled water, and the pH was adjusted to the range of 7.3-7.6 using glacial acetic acid and sodium hydroxide. After decalcification, the bones were rinsed four times and prepared for embedding in paraffin. Before embedding, the bones were transferred through a series of graded ethanol solutions (30%, 50%, and 70%) for at least 30 minutes each.

Following the decalcification and dehydration processes, xylene was used to clear the dehydrated specimens. The samples were then infiltrated with liquid paraffin wax, embedded in paraffin, and made ready for sectioning. The paraffin-embedded samples were sectioned using a microtome to a thickness of 5-20 µm. The paraffin sections were floated on a water bath, collected on glass slides, and dried. The mounted sections were then deparaffinized, rehydrated, and stained with hematoxylin and eosin.

Staining Method	Described color results	Identifiable tissues and structures	Suggestion application
H&E	Nuclei: Blue or dark purple Eosinophilic structures: Pink	Bone: Dark Pink Connective Tissue: Light Pink A vessel containing Erythrocyte: Bright Red Nuclei: Dark purple	General Overview

Chapter 4 Results and Discussion

4.1 Results Discussion of Micro-T Characterization

The use of micro-CT allows for the quantitative assessment of bone structure, which can be used to estimate bone strength through mathematical calculations. The overall bone mineral density was higher in normal bones compared to both types of knockout bones. Trabecular bone density was lower in normal bones in comparison to the knockout bones. Cortical Porosity increased in knockout bones; it could be suggested that the normal bones are smoother than knockout bones and knockout bones are more fragile than the normal bones.

In the analysis of trabecular bone, it was observed that the Femoral Bone Volume Fraction (BV/TV) was lower in normal mice. This decrease was accompanied by higher femoral Trabecular Separation, lower femoral Trabecular Thickness, and higher femoral Trabecular Number in normal bone. There was a significant difference in Trabecular Bone density between normal and knockout bones. Additionally, Cortical Density displayed a different pattern, higher in normal samples along with Cortical Thickness.

These findings are consistent with our central hypothesis, which states that OFD and NF1 diseases have a significant impact on bone composition and mineral-to-matrix structure. This results in a decrease in trabecular density and an increase in normal bone mineral density. Given the increased trabecular density in knockout bones compared to normal bones, it is expected that the bone strength of knockout bones would be lower. This was further supported by the results of the Vickers hardness test, which indicated a lower Vickers number for knockout bones compared to normal bones.

Overall, this study revealed that knockout bones exhibited significant differences from normal bones, with the knockout bones showing delayed development and changes in mass. The differences were attributed to variations in cortical parameters. Specifically, in normal samples, cortical density, and thickness were higher, while trabecular measures were lower. In contrast, knockout samples displayed lower cortical density and thickness but higher trabecular density measures. One possible explanation for these findings is that mineral deposition involved in bone growth is somehow inhibited in the knockout.

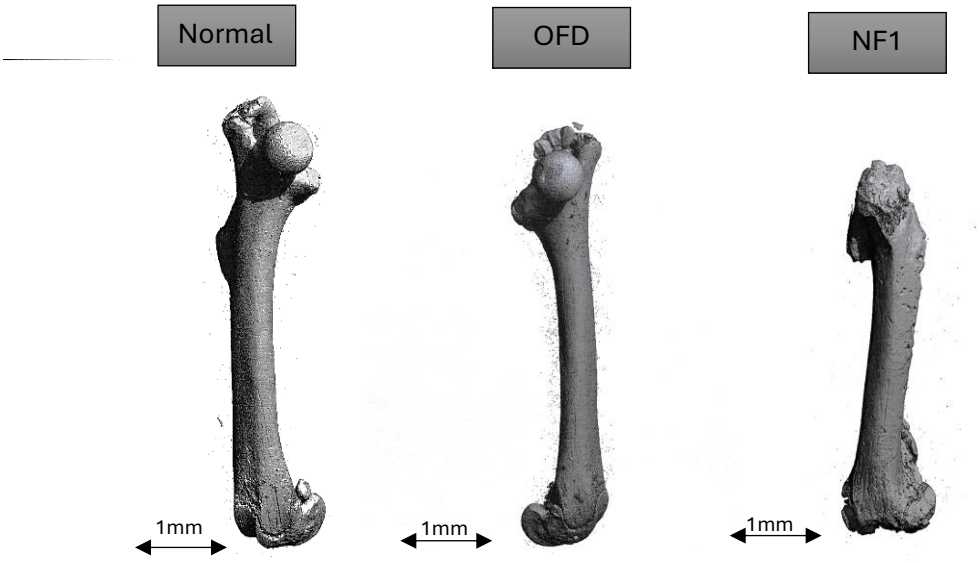

Figure 4-25. Micro-CT images of whole bones of normal, OFD and NF1 knockouts.

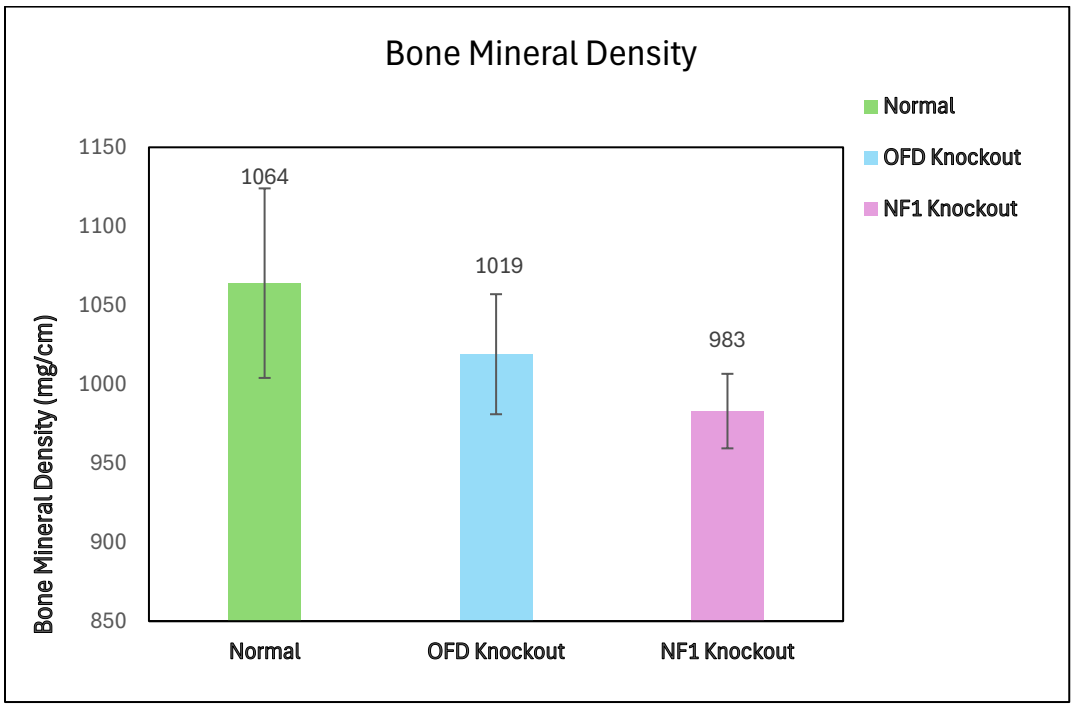

Figure 4-26.Bone Mineral Density of normal, OFD, and NF1 knockout bones. For normal vs OFD at the 0.05 level, the population means are significantly different.

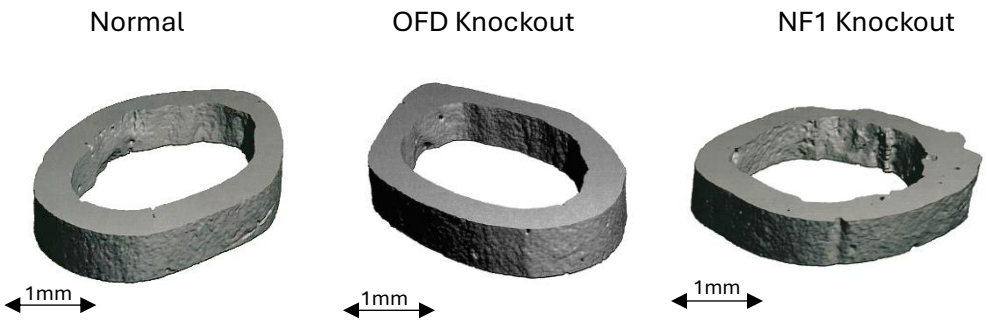

Figure 4-27. Micro-CT images of the cortical shell thickness of midshaft of normal, OFD and NF1 knockout bones.

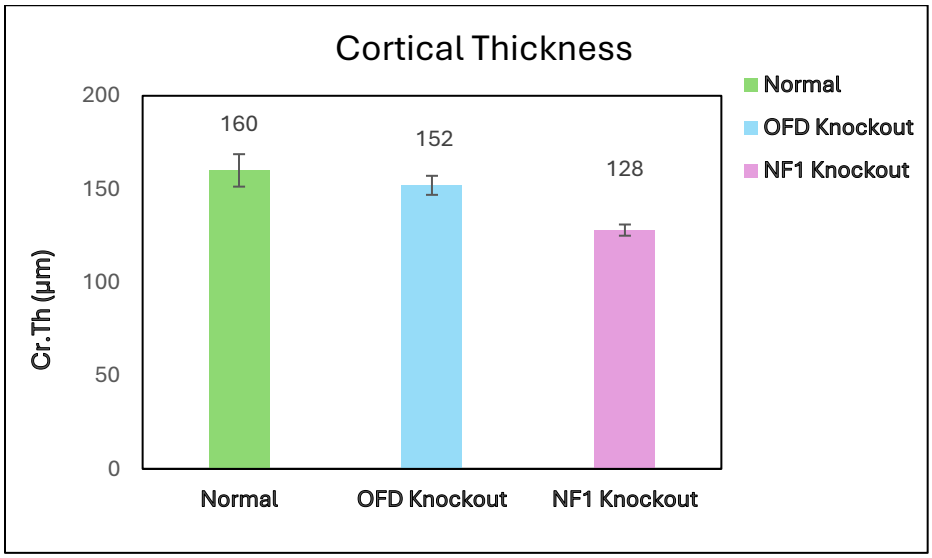

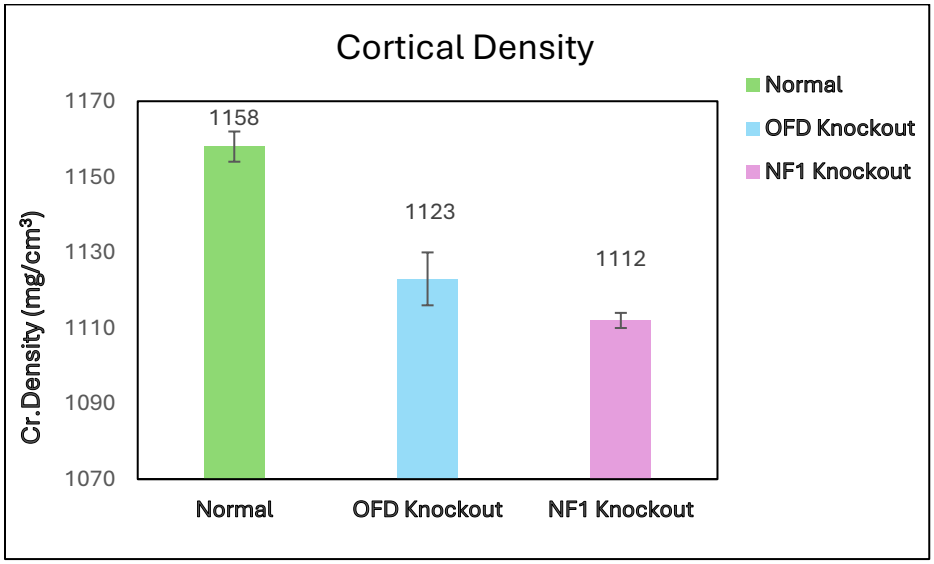

Figure 4-28. Cortical bone parameters (Cr. Th, Cr. Density) across the midshaft of normal, OFD, and NF1 knockout bone. For normal vs OFD at the 0.05 level, the population means are significantly different.

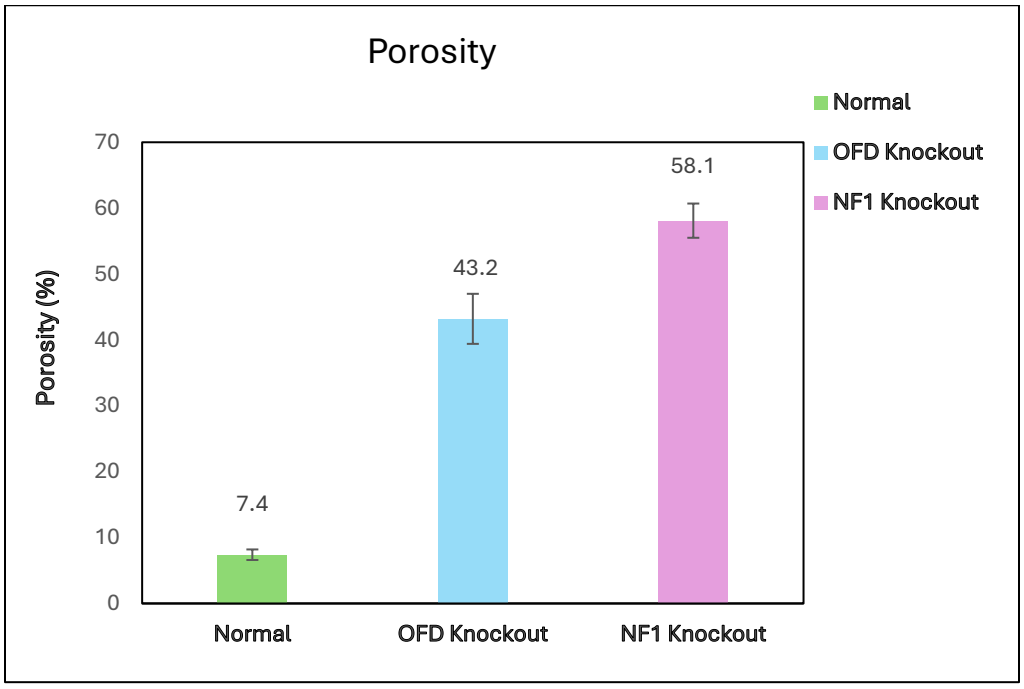

Figure 4-29. Cortical bone Porosity across the midshaft of normal, OFD, and NF1 knockout bone. For normal vs OFD at the 0.05 level, the population means are significantly different.

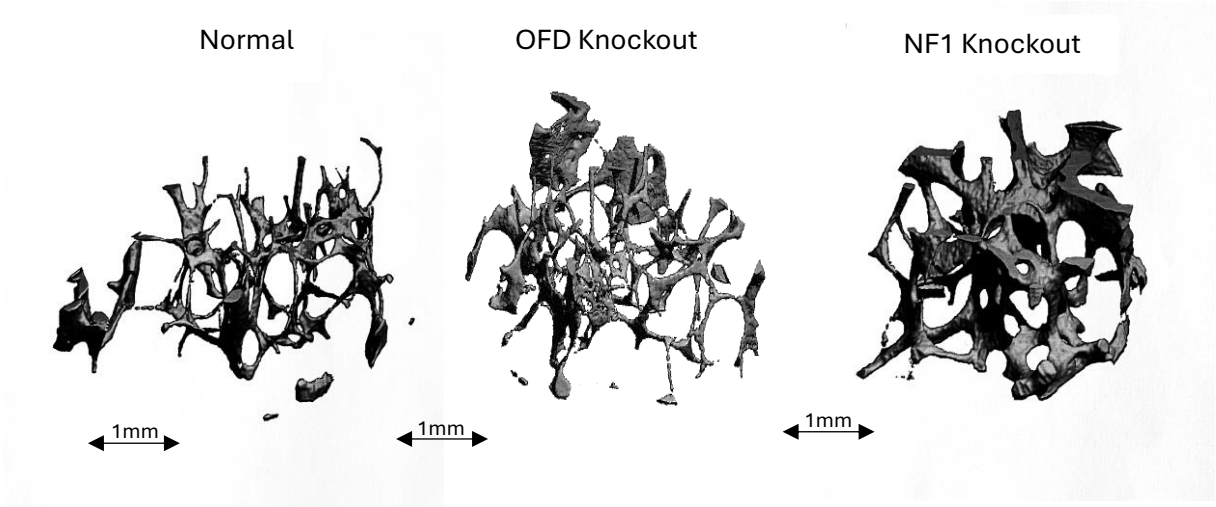

Figure 4-30. Micro-CT images of trabecular norma, OFD, and NF1 knockout bones.

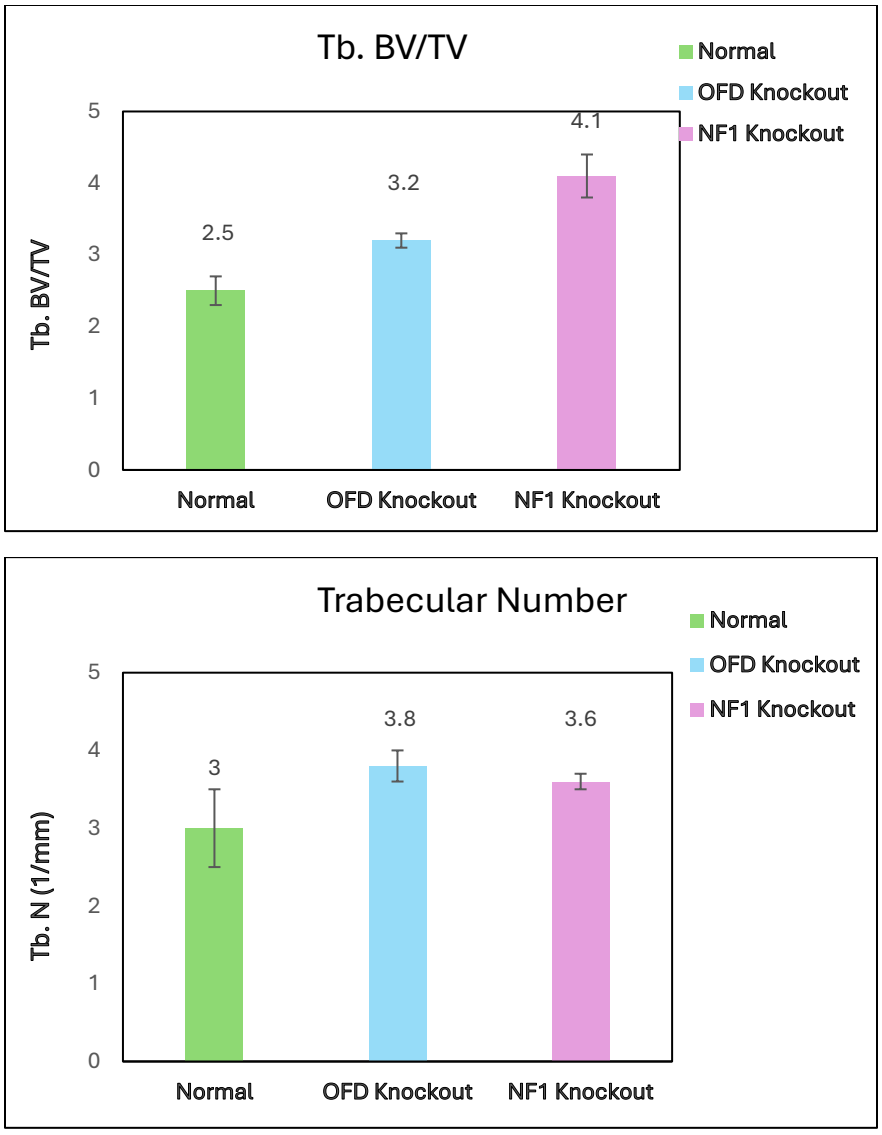

Figure 4-31. Trabecular bone microstructure BV/TV and Trabecular N of normal to NF1 knockout bones. For normal vs OFD at the 0.05 level, the population means are significantly different.

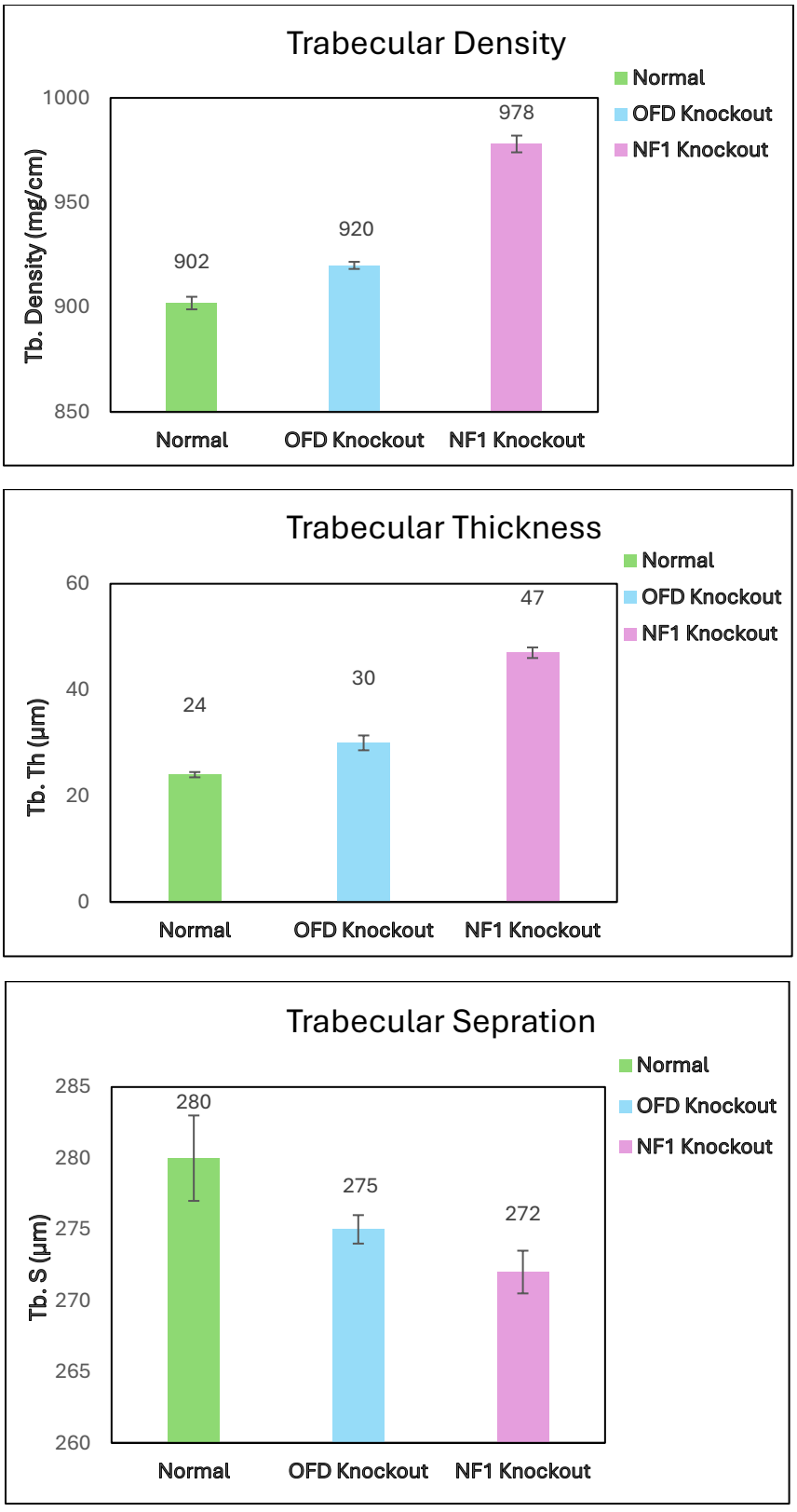

Figure 4-32. Trabecular bone microstructure (Tb. Density, Tb. Th, and Tb. S) of normal and NF1 knockout bones.

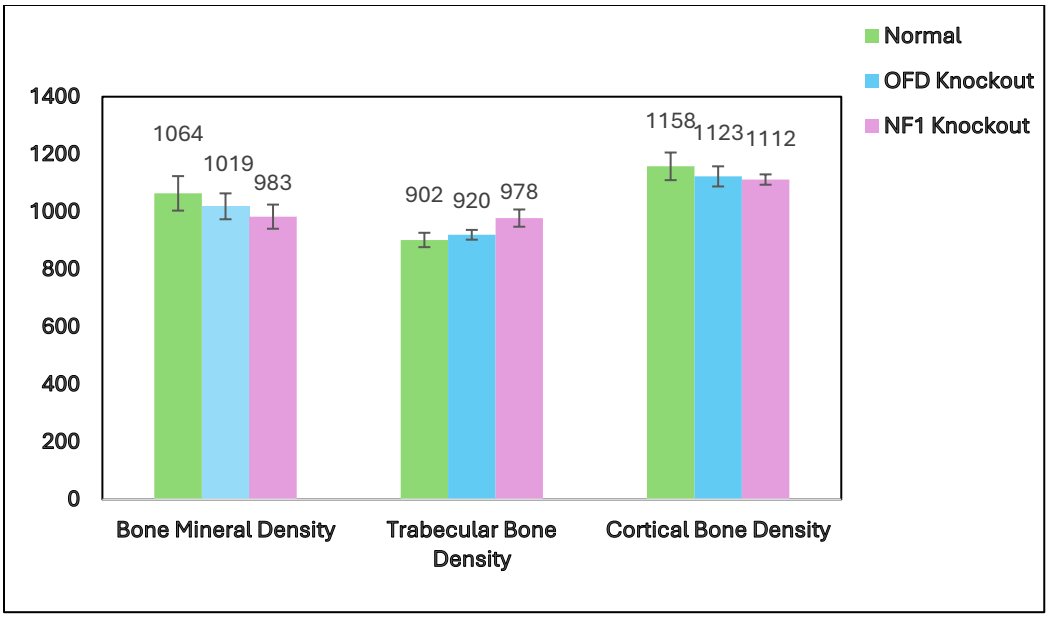

Figure4-33.Comparison of Bone Mineral Density, Trabecular Bone density, and Cortical Bone Density of Normal, OFD, and NF1 Knockout bones.

4.2 Result Discussion of Raman Spectroscopy Characterization

The work carried out in this research strongly verified that differences in mineral-to-matrix composition between normal and knockout bone can be measured using Raman spectroscopy. This was supported by data obtained from the femur, indicating that the mineral-to-matrix composition differs significantly for bone samples from different areas of microanatomy and bone structure. The hypothesis was reasonable and was supported by reduced variance in multiple bone mineral-to-matrix indices calculated from repeated Raman measurements over a small bone surface area, compared to single laser spot measurements.

The average mineral-to-matrix index for the normal specimens was significantly higher in the normal bones ($P < 0.05$). For all the samples, the signal strength of phosphate was very strong while the signal strength for the matrix marker (amide I) was very weak, consistent with the highly mineralized cortical bone of the femur. However, this led to errors in the peak height calculation and high variance in the index measurements for the femur.

With Raman spectroscopy, detecting a specific phase (mineral-to-matrix) is difficult as it does not show microstructure and surface morphology. The maximum magnification through DXR Raman is 100X. Spot detection means that the length covered by the laser is 1 μm with the 50X lens used at a single time. Therefore, relying on one spot does not give an accurate result, as it may contain more minerals or amide/protein. To address this limitation, 2D Raman mapping was used to collect several spectra from very near and

small areas, and averaging spots collected from the 2D Raman mapping area gave reliable mineral-to-matrix ratios.

This study evaluated different Raman modalities and measurement approaches but was inconclusive for biological conclusions due to limited sample size and scope. Additionally, the number of animals and the age range were limited, and only female mice were used for the samples.

Limitations and potential errors

There are several potential sources of variability and errors in the application of Raman microprobe techniques to bone. Interference from fluorescence is one of the greater sources of error and is difficult to control despite standard accepted procedures to reduce its effects. Examination of alternative peak frequencies may find improved signals with less interference. Selective cleaning of bone and removing periosteum residues while leaving the structural matrix intact may also reduce fluorescence signals. Alternative laser excitation frequencies may provide a deeper sampling of bone layers, while still providing acceptable signal levels for Raman shifted scattered signal frequencies.

Sample surface roughness may also affect the quantitative aspects of Raman. Polishing was used only lightly, to avoid disruption of bone microstructures. The bone samples are nominally dry, but not desiccated; some variable amount of residual and trapped water may be present in the samples, which could be a source of variation in some measurements.

For confirmation of biological significance, an examination of a larger number of different animals and samples would be carried out to determine the variability and statistical power needed for confidence levels.

Table 4-6. Mn/Mx Data details for femur mid-shaft diaphysis from Raman spectra.

Mn/Mx: FEMUR MID-SHAFT DIAPHYSIS – RAMAN						
	Normal		NF1 Knockout		OFD Knockout	
Mn/Mx	# 1	6	# 1	5.5	# 1	6.3
	# 2	6.5	# 2	7.3	# 2	5.1
	# 3	5.1	# 1 position 2	5.6	# 3	6.2
	# 4	7.2	# 1 position 3	5.9	# 4	4.9
	# 5	8.5	# 1 position 4	5	# 5	7.5
	# 6	6.3	# 1 position 5	6.1	# 6	6.4
	# 7	5.2	# 1 position 6	3.5	# 1 position 2	5.9
	# 8	7.4	# 2 Position 2	5.3	# 1 position 3	6.5
	#1 position 2	6.5	# 2 Position 3	5.2	# 1 position 4	6.2
	#1 position 3	7.3	# 2 position 4	3.3	# 1 position 5	5.7
	#1 position 4	5.8	# 2 position 5	5.5	# 1 position 6	4.8
	# 1 position 5	9	# 2 position 6	4.9	# 2 Position 1	5.3
	# 1 position 6	6.7			# 2 Position 2	5.7
	# 2 Position 2	5.8			# 2 Position 3	6.2
	# 2 Position 3	6.3			# 2 position 4	7.1
	# 2 position 4	8.7			# 2 position 5	6.1
	# 2 position 5	7.1			# 2 position 6	6
	# 2 position 6	6.5				
Mn/Mx AVG		6.8		5.3		6
Std Dev		1.2		1.07		0.95

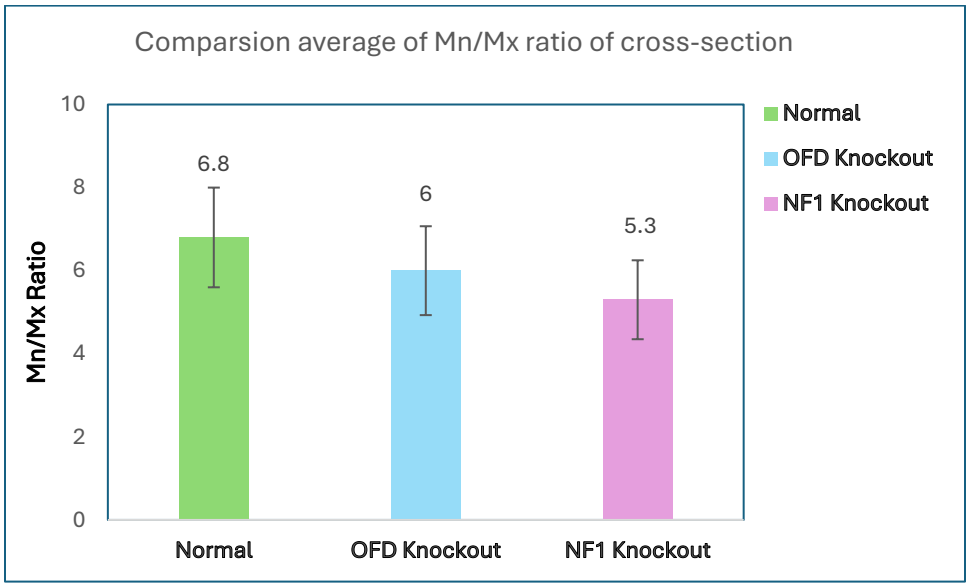

Figure 4-34. Comparison average of Mn/Mx ratio for Normal, OFD, and NF1 bones cross-section.

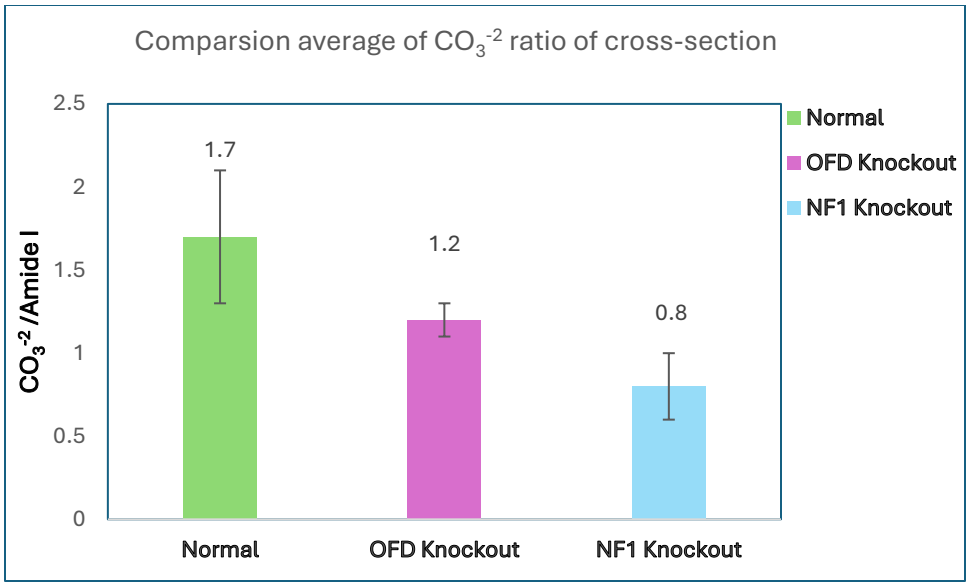

Figure 4-35. Comparison average of Carbonate to Amide I for normal, OFD, and NF1 bone cross-section.

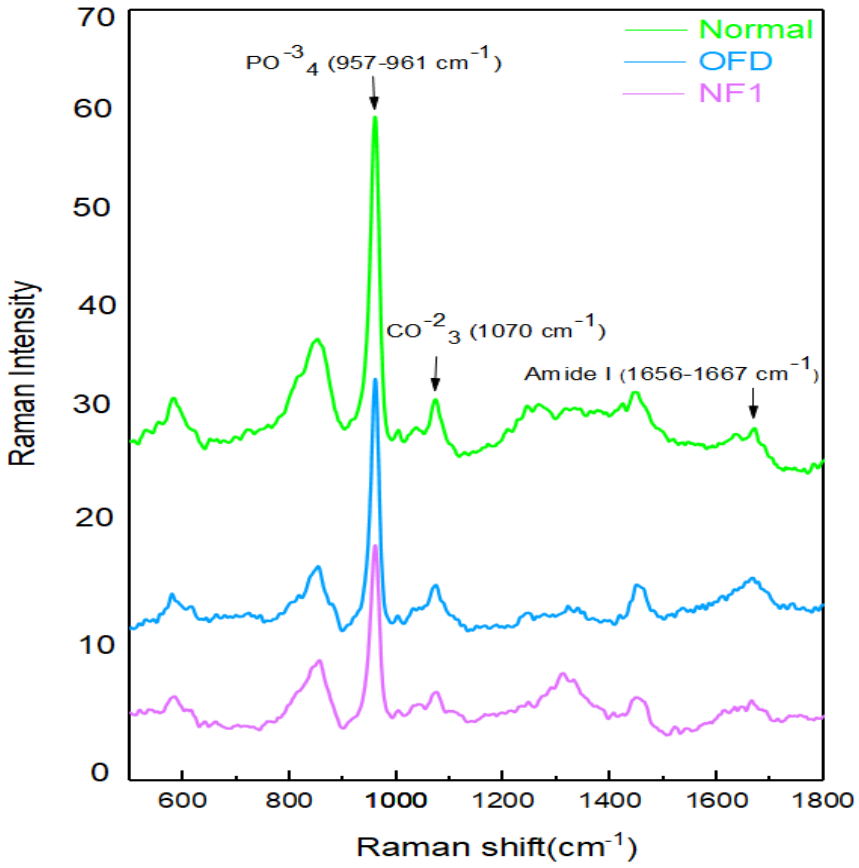

Figure 4-36. Raman spectra for Normal, OFD, and NF1 bones.

4.3 Results Discussion of 2D Raman Mapping

The mineral-to-matrix ratio of bone quality, a commonly reported measure, is often assessed using Raman spectroscopy. This technique measures the vibrational activity associated with specific chemical bonds in bone tissue. In the images obtained, the red and yellow colors represent high Raman activity, while the dark blue color corresponds to low Raman activity. Normal bone specimens show more extensive red and yellow regions, indicating higher Raman activity.

The PO_4^{-3}/amide I Raman activity ratio, which corresponds to the ratio of the area under the Raman band around 961 cm^{-1} (from 914 cm^{-1} to 990 cm^{-1}) to that under the peak around 1660 cm^{-1} (from 1640 cm^{-1} to 1690 cm^{-1}), was used for such analysis. Indeed, based on the overall presence of yellow, green, and light-blue regions, a lower PO_4^{-3}/amide I Raman activity ratio is observed in the image corresponding to Knockout bones than in that of normal bone.

We were also looking for a potential correlation between the CO_3^{-2}/amide I, Areas under the carbonate band around 1074 cm^{-1} (from 1038 cm^{-1} to1105 cm^{-1}), and under the amide I band around 1660 cm^{-1} (from 1640 cm^{-1} to 1690 cm^{-1}) were considered for this CO_3^{-2}/amide I ratios. The smaller amount of high CO_3^{-2}/amide I ratio is noticed in the Knockout images. 2D mapping verified that our results which we got from the Raman spectroscopy randomly selected spots from the surface of the bone and shows that in both methods they have the same behavior between normal and knockout samples.

The 2D mapping of Raman spectroscopy data confirms the consistent differences between normal and knockout bone samples. The intense colors in the 2D maps of normal bones are more organized and clustered, while those of knockout bones appear less organized, suggesting disorganization in the knockout bone structure.

The Raman 2D maps also provide valuable information about the composition of the bone samples. These maps indicate the matching percentages of each bone sample with reference chemical components. For instance, normal bone samples showed a 100% match with a component called Tinticite, while knockout bone samples showed matches with other apatite components like Chlorapatite (Ca5(PO4)3Cl) and Monetite (Ca (PO_3OH)). In the NF1 knockout bones, the statistical match was only 81.5% with Tinticite and 18.5 % with chlorapatite and in the OFD knockout bones the statistical match was 91.5% Tinticite and 8.5% Monetite, this suggests differences in the mineral composition between normal and knockout bones.

Furthermore, the intensity of peaks corresponding to certain chemical components, such as calcium and amide I, differs between normal and knockout bones. The differences observed in the Raman spectroscopy data align with the central hypothesis of our research, indicating potential development issues in knockout bones.

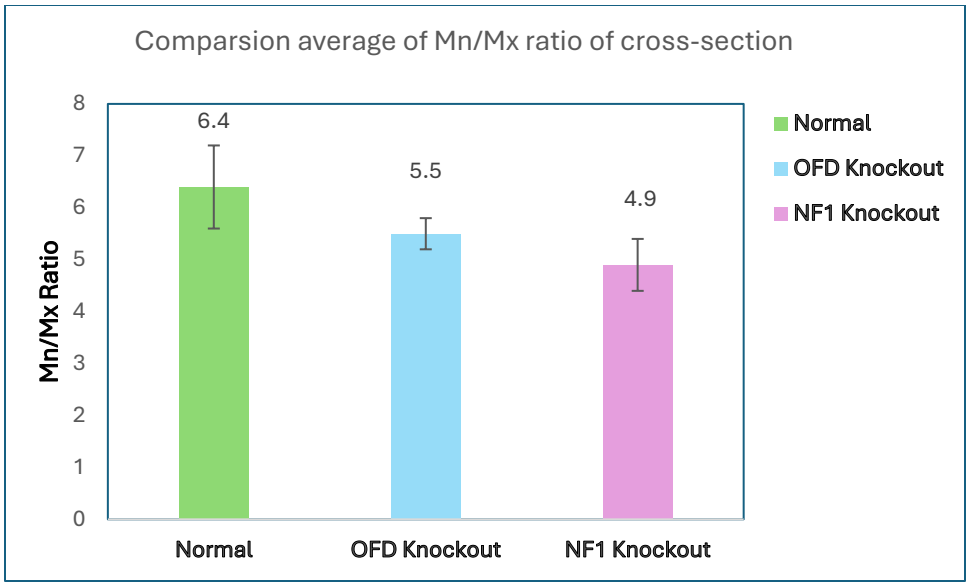

Figure 4-37. Comparison average of Mn/Mx Ratio of Normal, OFD, and NF1 bones cross-section.

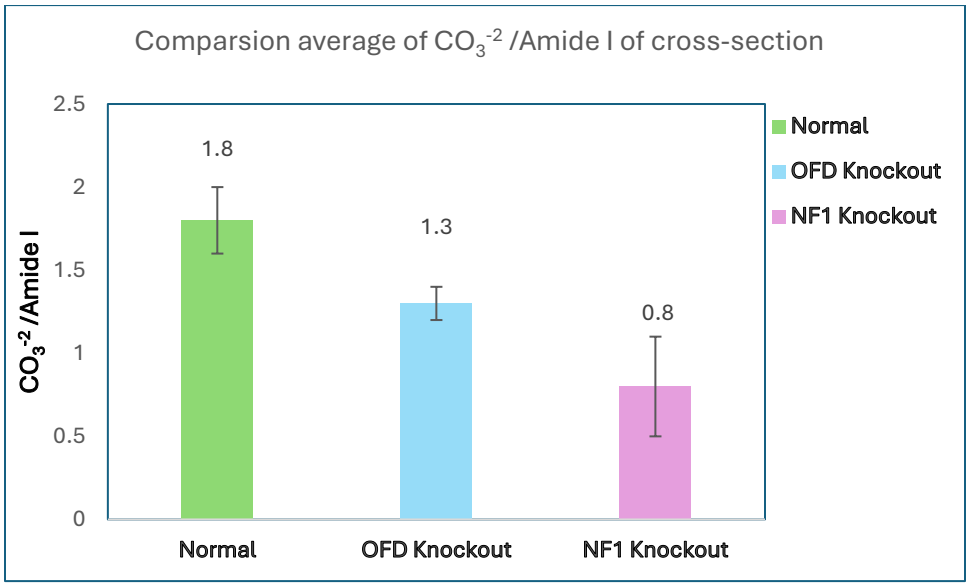

Figure 4-38. Comparison average of Carbonate to Amide I of Normal, OFD, and NF1 bones of cross-section.

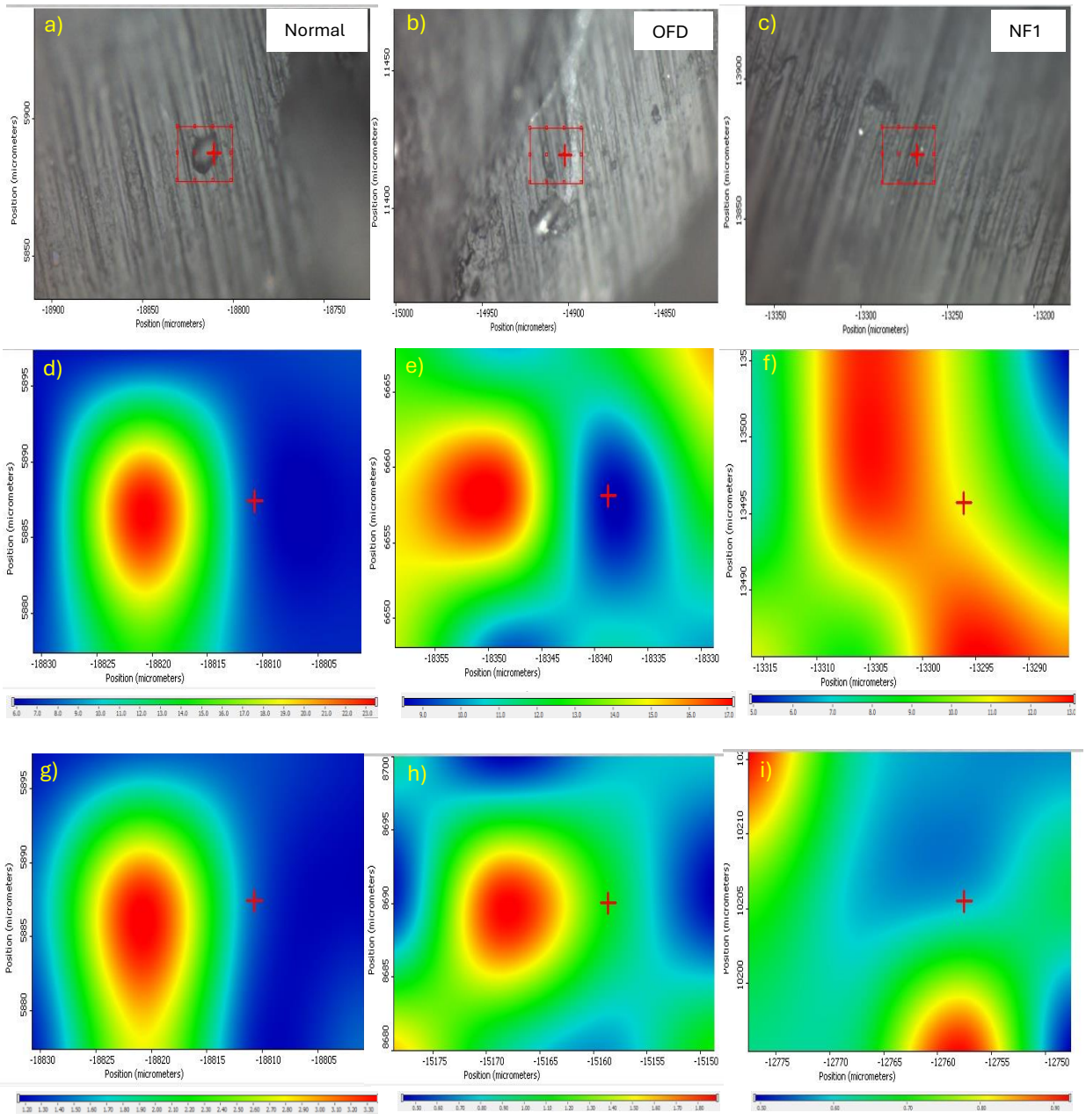

*Figure 4-39. 2D Raman intensity maps for Normal, OFD and NF1 bones cross-section. The intensity maps show; (**a, b, c**) the selected area under the microscope; (**d,e,f**) the Mn/Mx ratio 2d map; (**g,h,i**) the CO/Amide I ratio 2D map.*

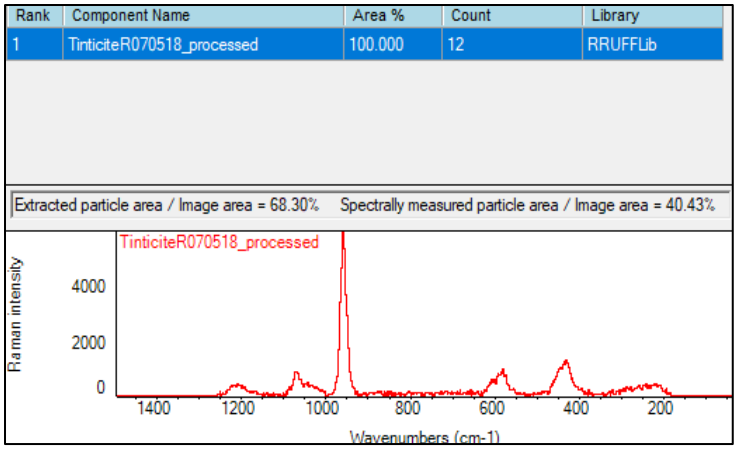

Figure 4-40. 2D Raman particle analysis identification map for Normal bones.

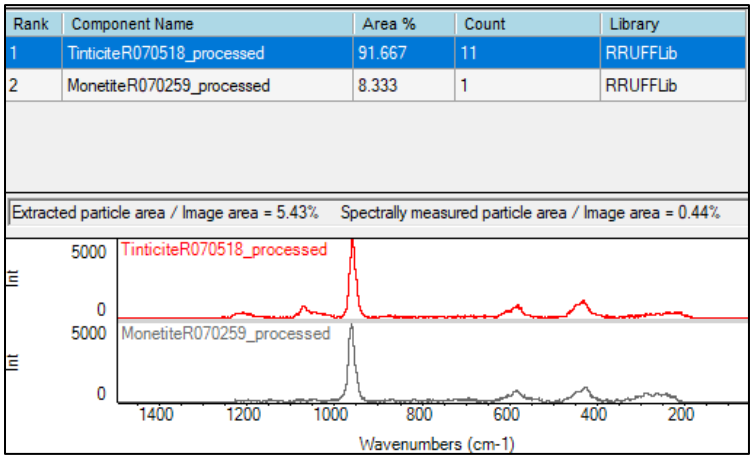

Figure 4-41. 2D Raman particle analysis identification map for OFD knockout bones.

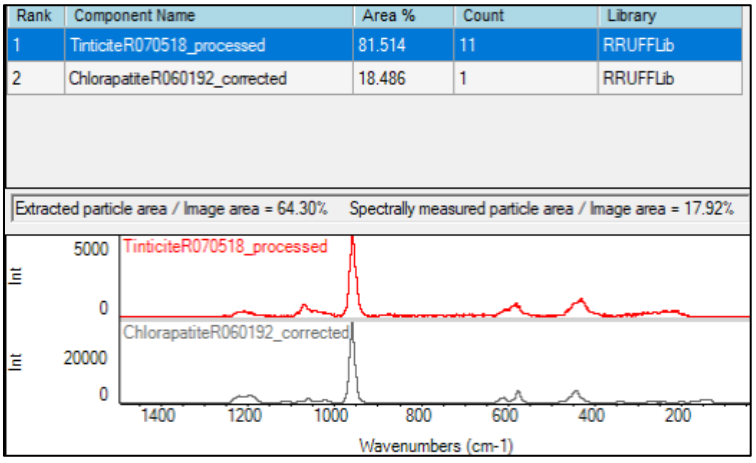

Figure 4-42. 2D Raman particle analysis identification map for NF1 knockout bones.

4.3 Result Discussion of Scanning Electron Microscopy Characterization

The results of the EDS compositional analysis for calcium (Ca) and phosphorus (P) did not indicate lower levels for these two elements in the knockouts, contrary to what might be expected from the Mn/MX ratios measured by Raman spectral peaks. This could be due to a higher amount of inorganic minerals in the knockouts, which is not detected by Raman absorption peaks but is picked up by EDS. This is a new finding that supports a proposed mechanism for NF1 and OFD effects on bone, suggesting that NF1 and OFD loss leads to high production of inorganic mineral pyrophosphate, which then suppresses the formation of hydroxyapatite.

This new finding provides evidence for a possible mechanism for certain steps in the pathway of bone formation disrupted by the NF1 gene and OFD knockout. According to this mechanism: 1) NF1 suppresses the formation of inorganic mineral pyrophosphate, which inhibits normal apatite formation; 2) Loss of NF1 (knockout) results in excess pyrophosphate; 3) Excess pyrophosphate lowers mineralization in knockout bones. The elevated pyrophosphate levels in the knockout do not contribute to mineral-to-matrix measurements by the standard Raman method, as the spectral peaks for phosphorus are shifted. However, phosphorus and calcium in any chemical form can be detected by EDS/SEM analysis.

The Ca/N ratio is presented in the first bar grouping, showing a lower value in the normal compared to the knockouts. This would also be consistent with higher levels of calcium in the knockout due to the accumulation of calcium combined with pyrophosphate. Elevated levels of calcium are also associated with inflammation and tissue damage, consistent with the association of bone abnormalities with tumors in the knockout.

Limitations and Potential Sources of Error

There are several potential sources of variability and error associated with the application of the EDS technique to bone. Different atomic species produce secondary radiation with slightly different efficiencies, resulting in a systematic error in measured abundances. SEM/EDS measures to depths of approximately 10 μm, depending upon the material and electron energies; the measured secondary radiation intensity may be affected by the depth of the atomic species in the material sample. Sample surface roughness may affect the intensity of secondary radiation produced. Bone samples are nominally dry, but not desiccated; some variable amount of residual and trapped water may be present in the samples. This could be a source of variation in oxygen measurement and could lead to outgassing, which could affect resolution. Any further study of biological significance would need to examine several different animals and larger sample sizes to determine the variability and statistical power needed.

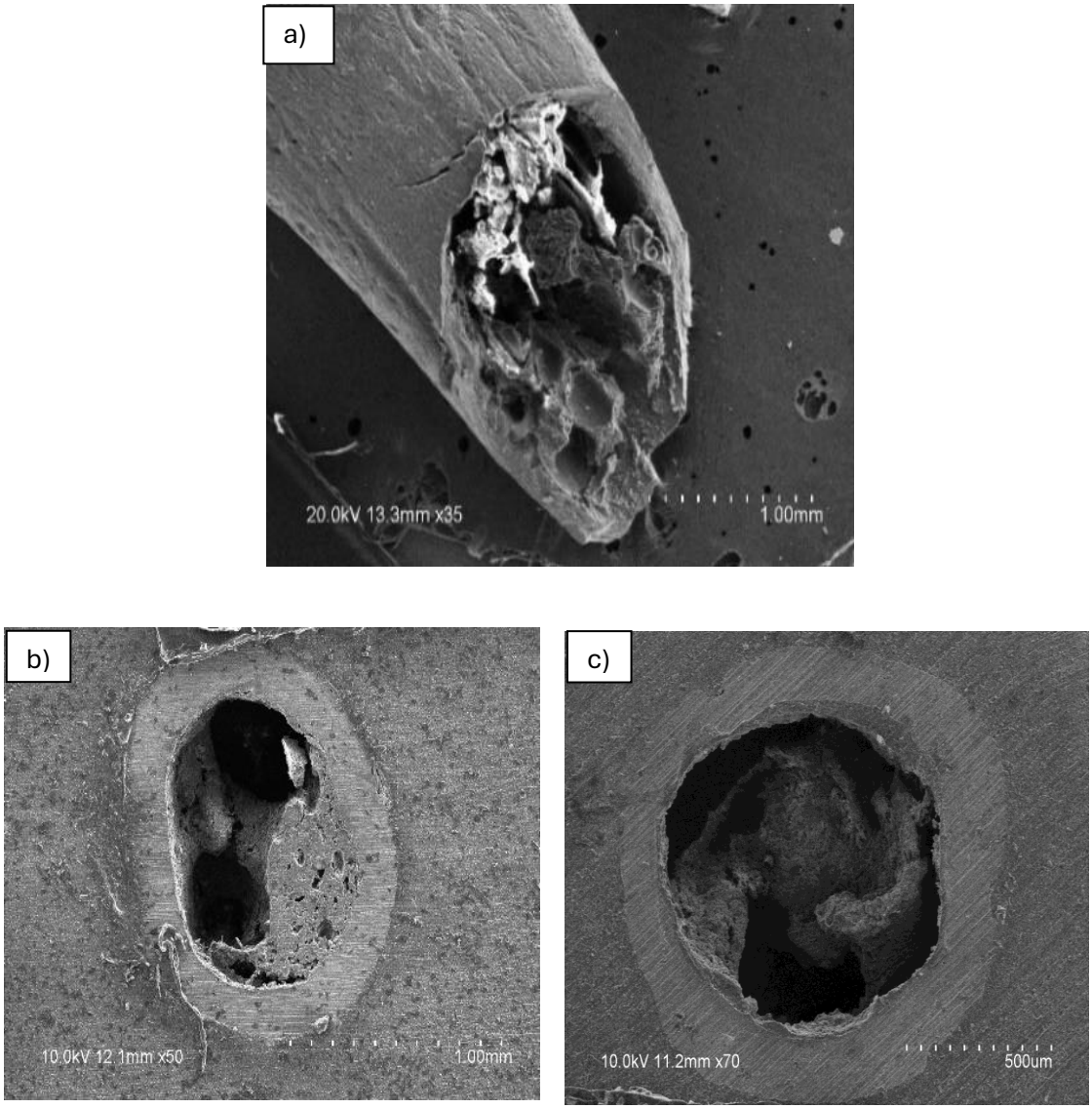

Figure 4-43. SEM Images of a) normal, b) OFD and c) NF1 bones cross-section.

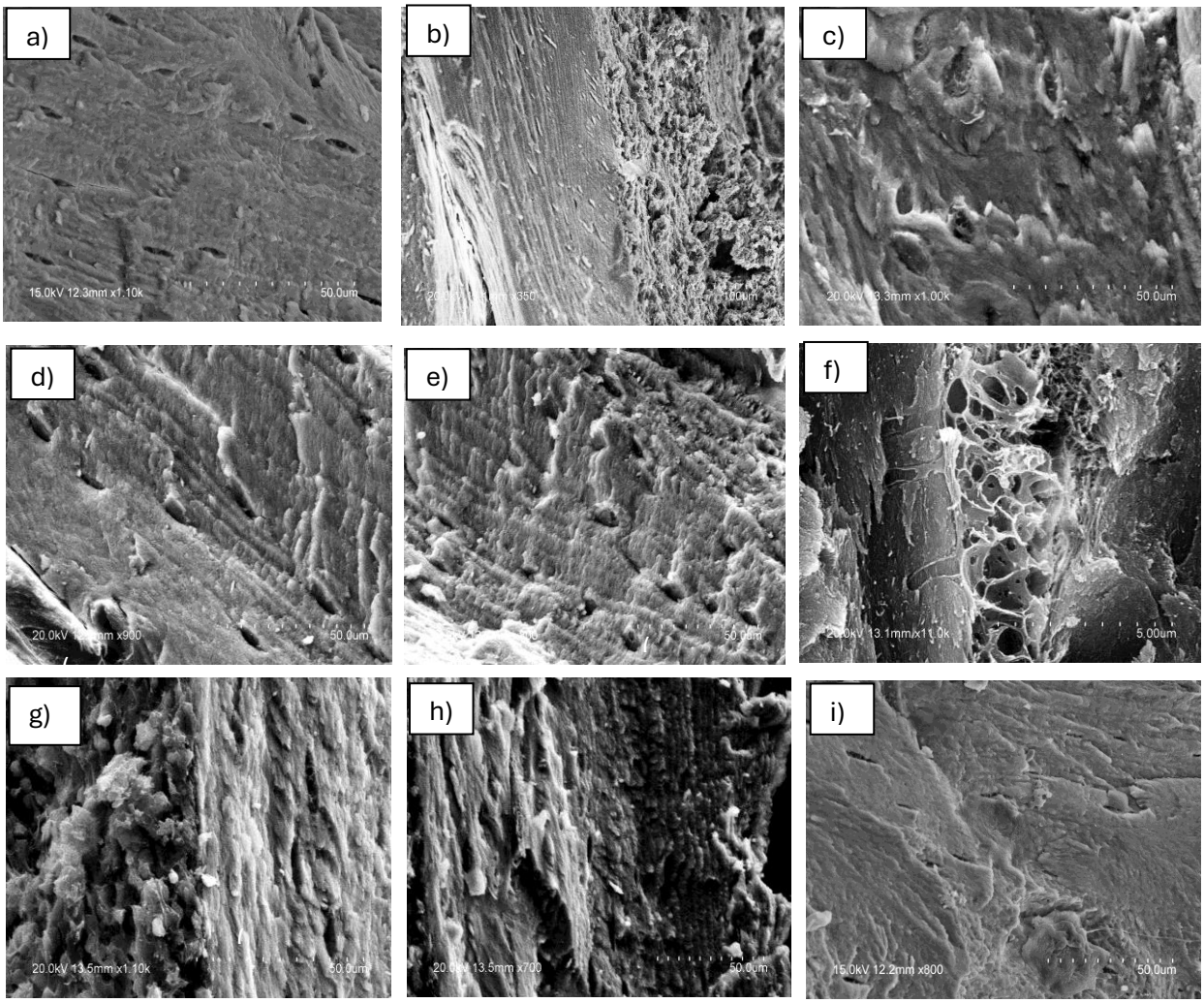

Figure 4-44. Images from cortical midshaft diaphysis(a) Image of surface from OFD sample (b) Image of distinguished the cortical bone from trabecular bone of normal bone (c, d ,e, f) Image of microregion of cortical bone (This SEM micrograph pores feature in the image may correspond to microanatomical and structural features, such as cells and haversian channels ,osteon or osteocyte lacune) (g) Image of distinguished the cortical bone from trabecular bone (h) Image of distinguished the cortical bone from periosteum bone,(I) Image of surface of NF1 sample.

Table 4-7. Average of elemental composition from EDS for Normal, OFD, and NF1 Knockout bones cross-section.

Element Ratio	Significance	Normal	NF1 Knockout	OFD Knockout
Ca/P	Mineral Quality	1.4	1.6	0.8
Ca/N	Mineral/Matrix	0.9	1.3	1.2
P/N	Mineral/Matrix	0.6	0.8	1.4

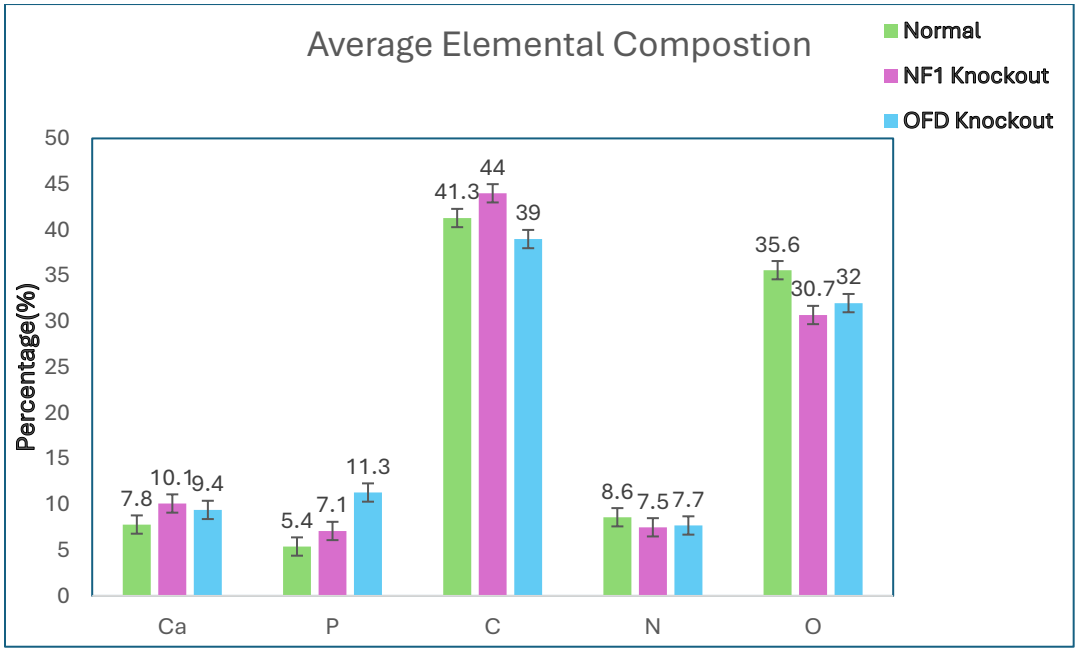

Figure 4-45. Average elemental composition in cortical cross-section of the femur for Normal, OFD, and NF1 bones.

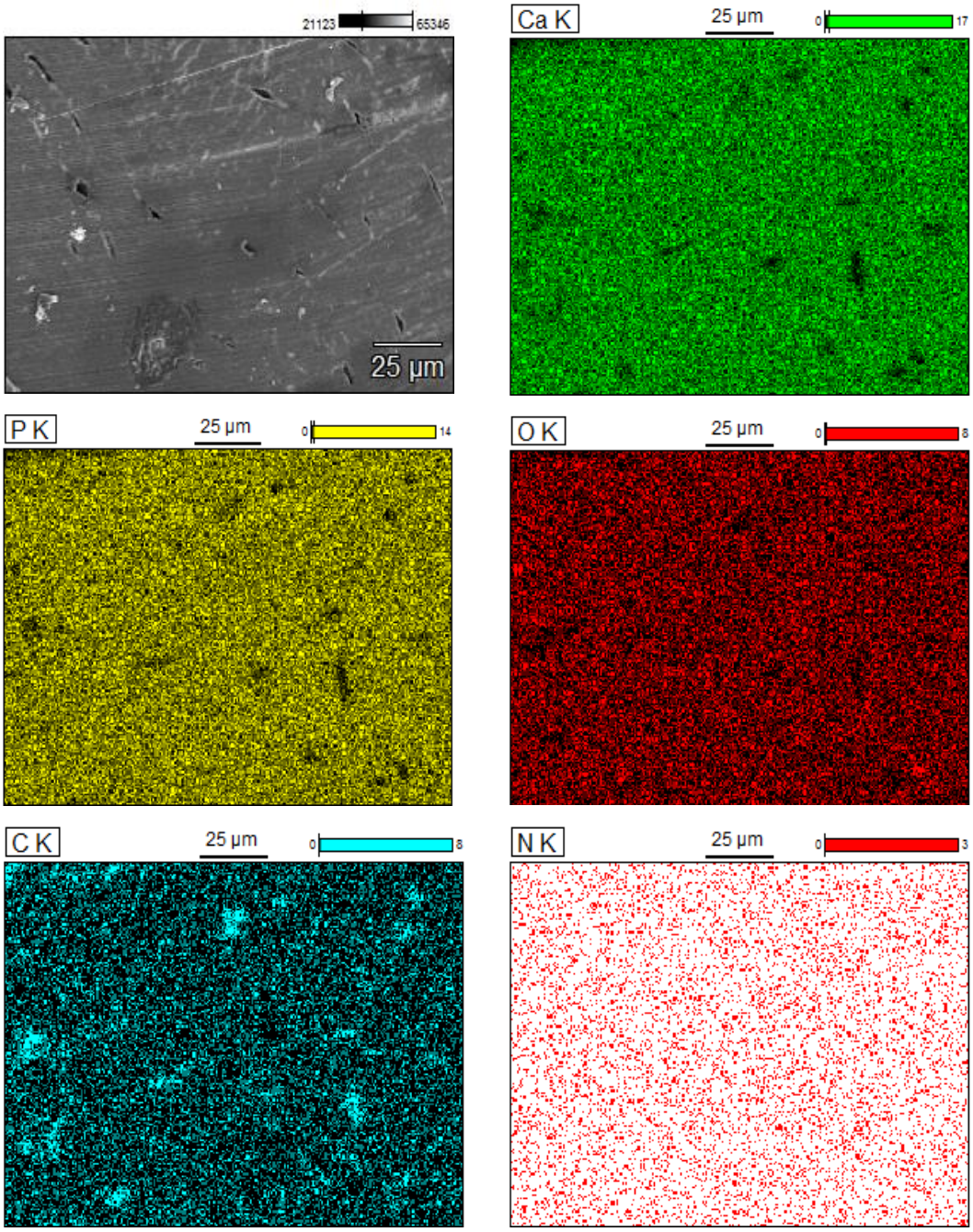

Figure 4-46. Elemental mapping image of Normal bone

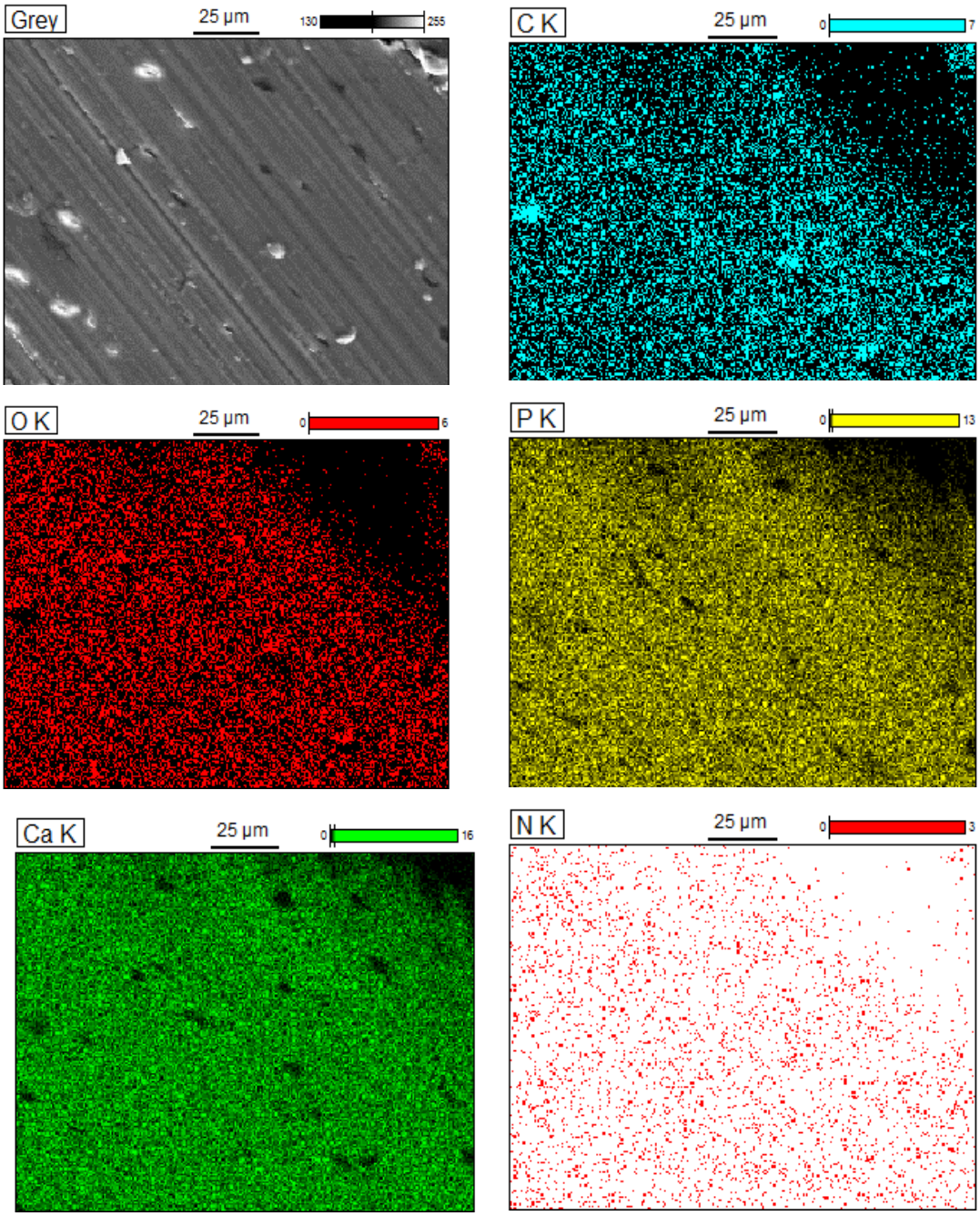

Figure 4-47. Elemental mapping images of OFD Knockout bone.

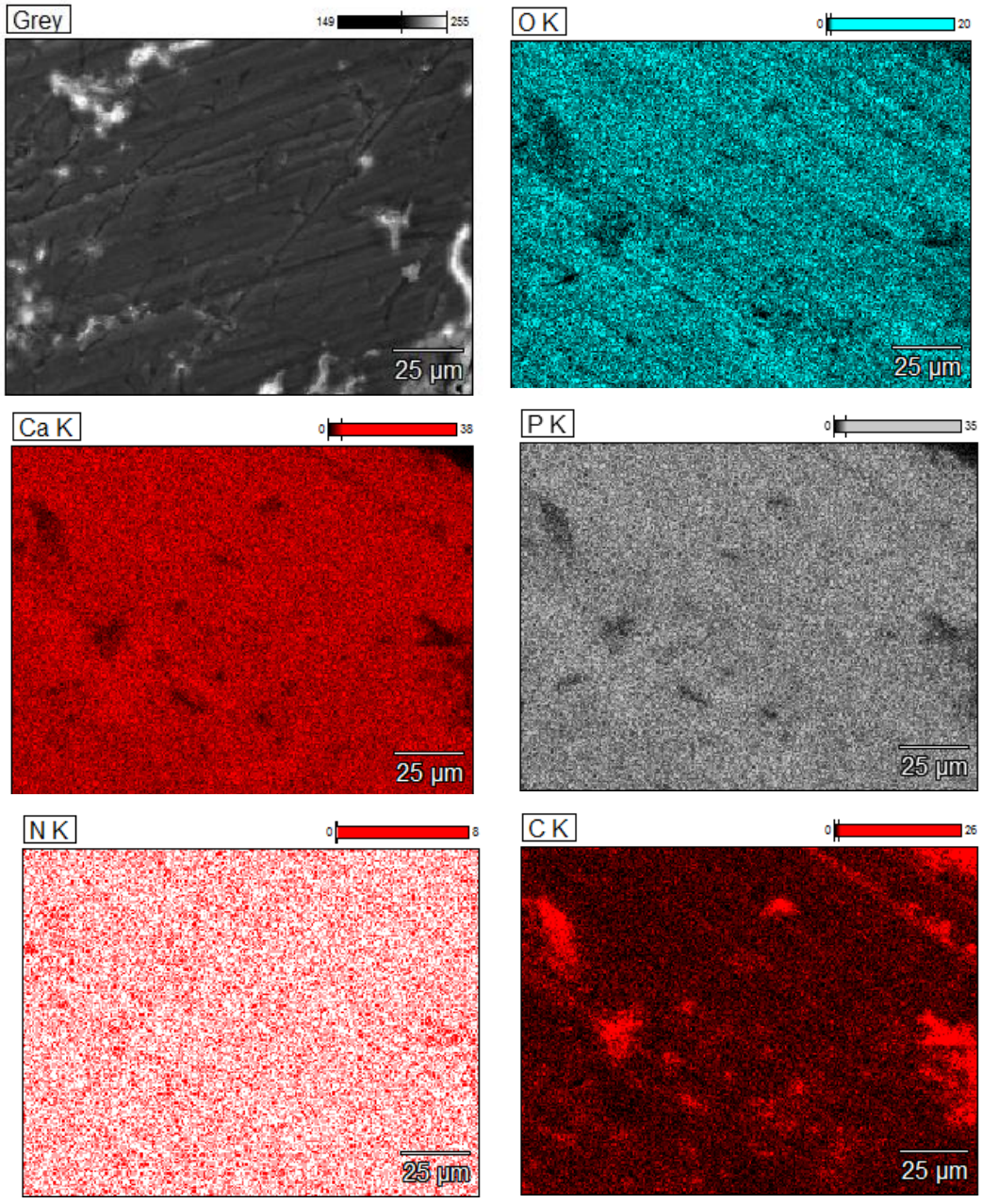

Figure 4-48. Elemental mapping images of NF1 Knockout bone.

4.4 Result Discussion of Micro Hardness Test Characterization

The microhardness measurement of normal and knockout bones is shown in Table 4, with an average of six locations for both normal and knockout bones under varying loads. The average hardness values for normal bones ranged from 75 to 49 HV, for OFD knockout bones from 66 to 41 HV, and for NF1 knockout bones from 62 to 33 HV.

There is a significant variation in hardness between normal and knockout bones, with the hardness value decreasing as the load increases. These differences are statistically significant and indicate a fundamental change in the microstructure of normal and knockout bones. This change is likely due to variations in the mineral content of the extracellular matrix resulting from bone remodeling activities at the surfaces. These results indicate heterogeneity in hardness across the bone cross-section, and it suggests that the organic matrix (collagen) is an important determinant of bone hardness that varies depending on the bone's transgenic changes.

Table 4-8. Vicker hardness microhardness value of Normal, OFD, and NF1 Knockout bones.

Load	Normal	OFD Knockout	NF1 Knockout
50	75±2.6	66±1.3	62±1.6
100	70±2.1	63±2	58±2.3
300	57±1.9	52±1.7	46±2.1
500	49±1.8	41±1.7	33±2

4.5 Result Discussion of Histology Characterization

OFD can be described under a microscope as having two main components: fibrous stroma and bone trabeculae with a characteristic zonation pattern. The lesion is predominantly fibrous, with thin, newly formed woven bone trabeculae. The bone trabeculae are formed by lamellar bone, characterized by parallel layers of calcified matrix, and become more numerous, thicker, and mature (lamellar) as they merge with the outer and inner cortices at the periphery.

The OFD knockout bone showed significant increases in the number of empty osteocyte lacunae compared with normal bone. Since the osteon is the mechanical sensor in bone control and remodeling, the higher number of empty lacunae could indicate the weakness of the OFD knockout bone compared to normal bones. Additionally, the shape of the trabecular bone in the OFD knockout bones suggests that OFD is responsible for the trabeculations of the cortical bone, leading to greater isolation of the bone from the marrow and higher porosity in the OFD knockout bone due to the presence of more marrow elements in the cortical area. This is consistent with the results of cortical porosity from micro-CT, suggesting that OFD knockout bone is more fragile than normal bones, particularly in the cortical area.

Comparing normal bones with OFD bones, differences can be observed in the number of osteocytes, and lacunae, within the same magnification area. Normal bones have a higher number of osteocytes and lacunae. OFD bones may include multinucleated osteoclasts. Additionally, the shape of osteons in normal bones differs from that in OFD bones, with normal osteons being well-shaped and nucleated and having a larger lamellae area. In normal bone, chondrocytes typically contain a single, large, clear vacuole, and their cytoplasm typically only partially fills the lacunar space.

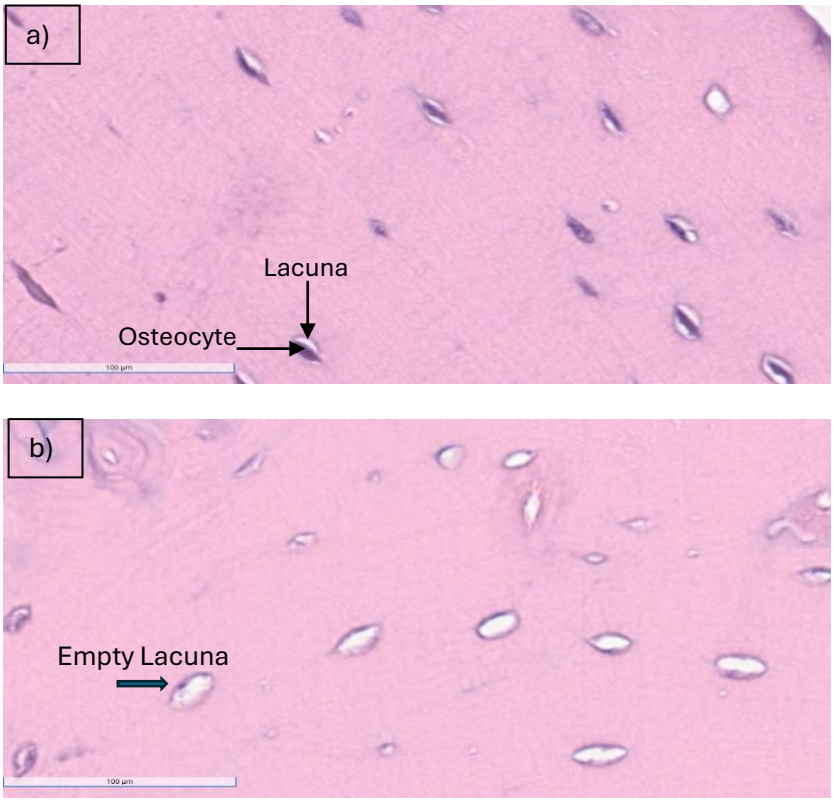

Figure 4-49. Presence of empty osteocyte lacunae in cortical bone. a) Section of Normal bone. b) Section of OFD Knockout bone.

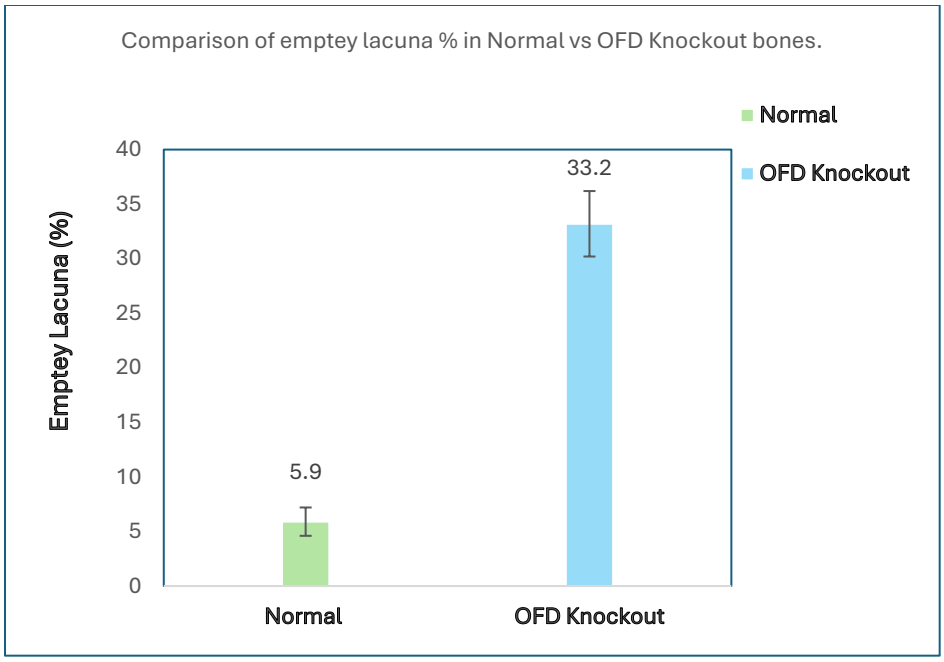

Figure 4-49. percentage of empty lacunae per total lacunae.

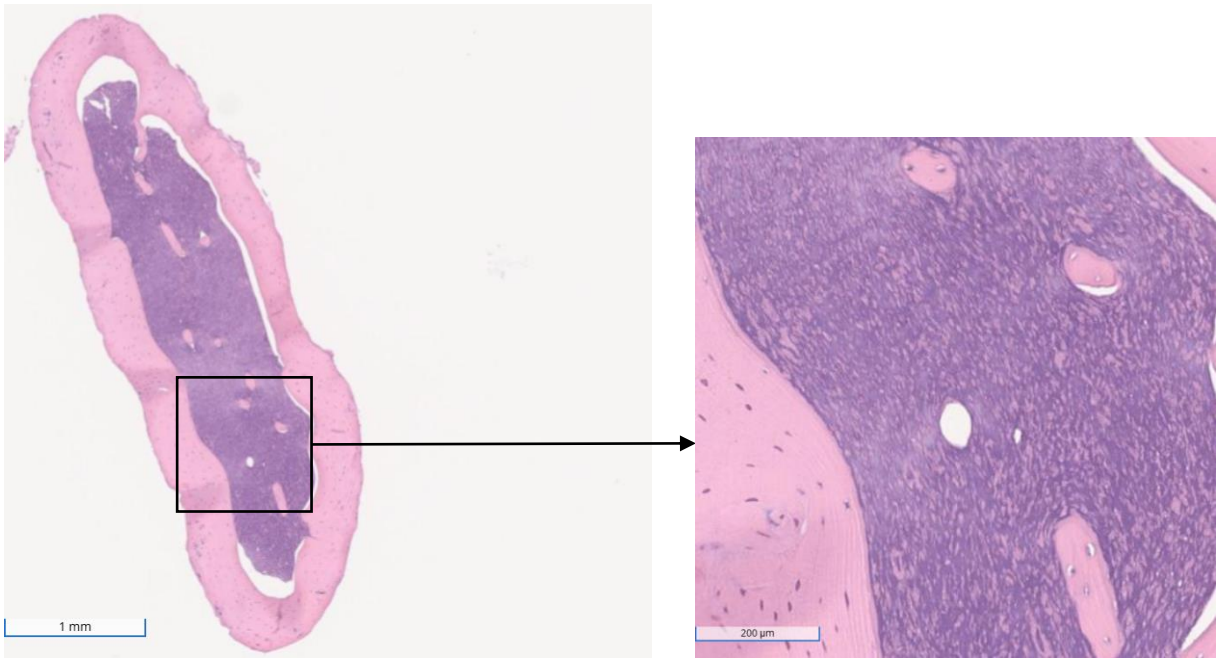

Figure 4-51. Cross-section of OFD Knockout bone (left) and higher magnification of selected area(right). (H&E Stain).

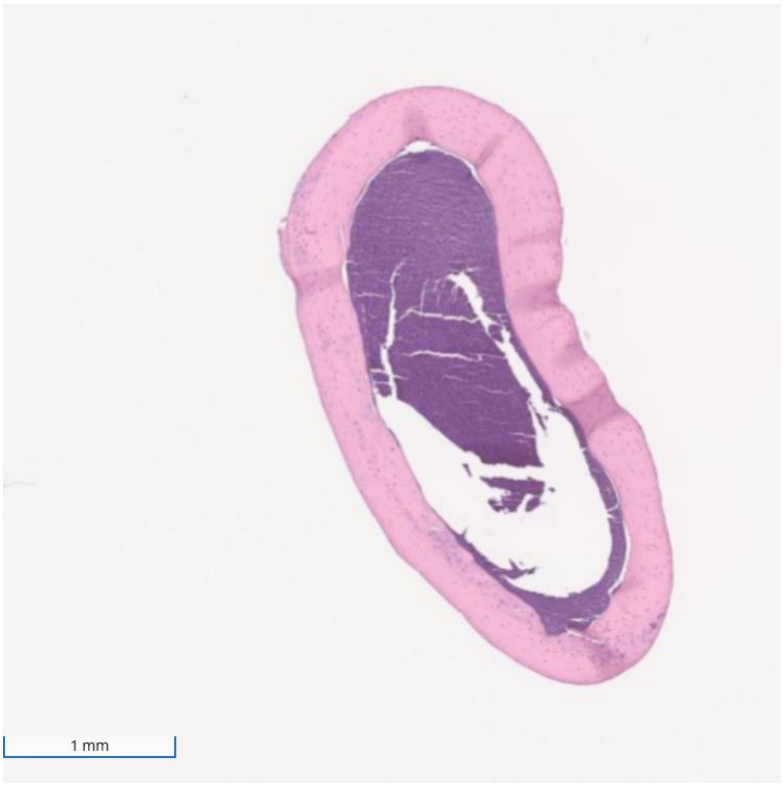

Figure 4-52.Cross-section of Normal bone. (H&E Stain)

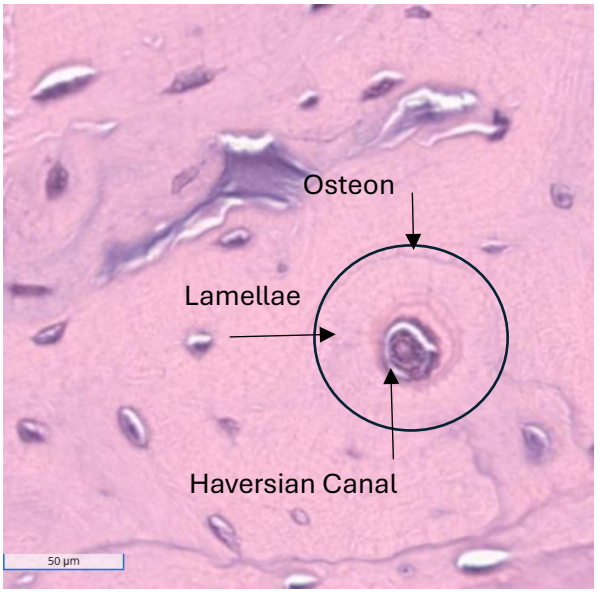

Figure 4-53. Osteon, Haversian canal, and associated structures in Normal bone. (H&E Stain)

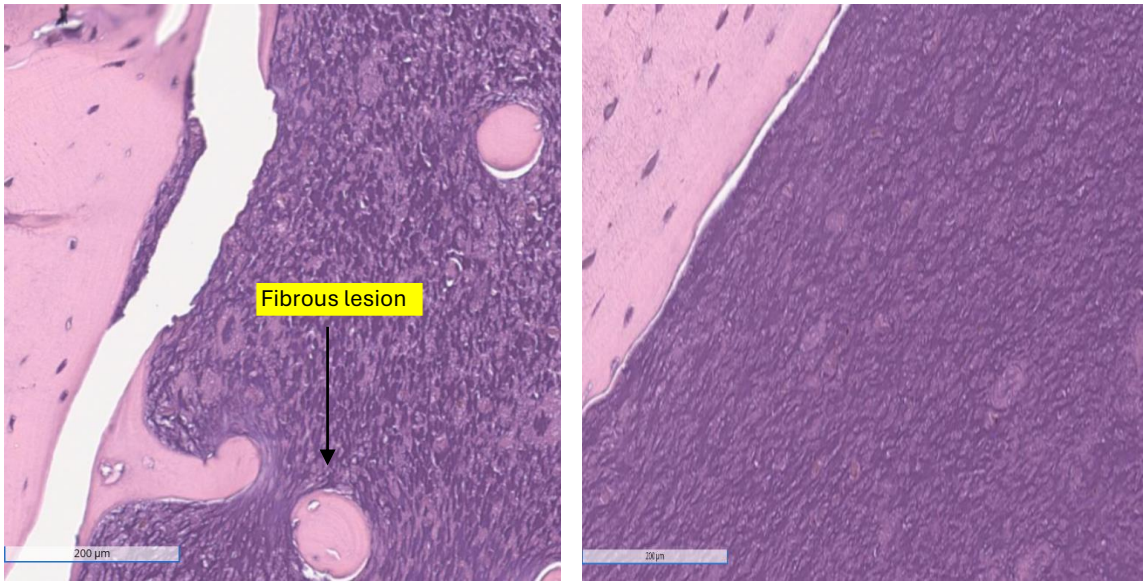

Figure 4-54. The fibrous lesion presented in OFD Knockout bone (left) vs Normal bone (right).

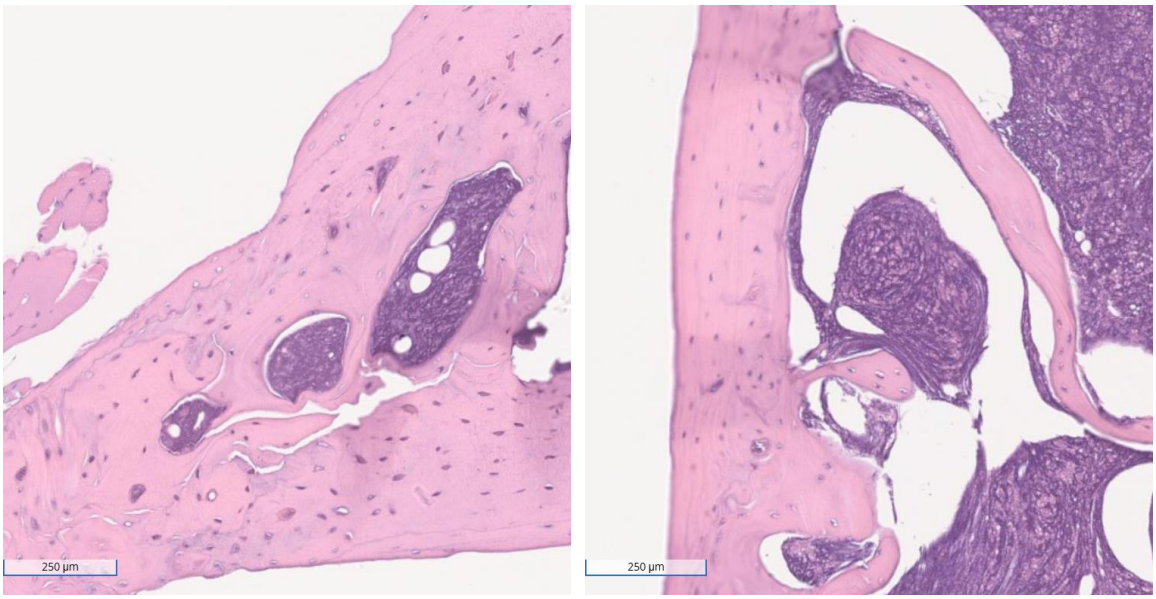

Figure 4- 55. Trabecula bone in OFD Knockout (left) vs Normal bone (right).

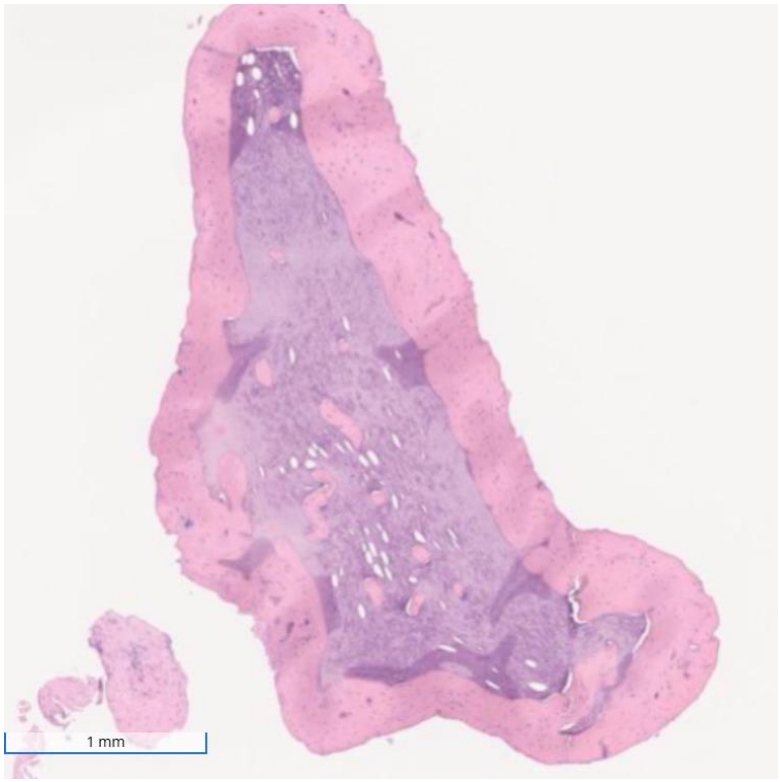

Figure 4-56. Growth plate of OFD bone.

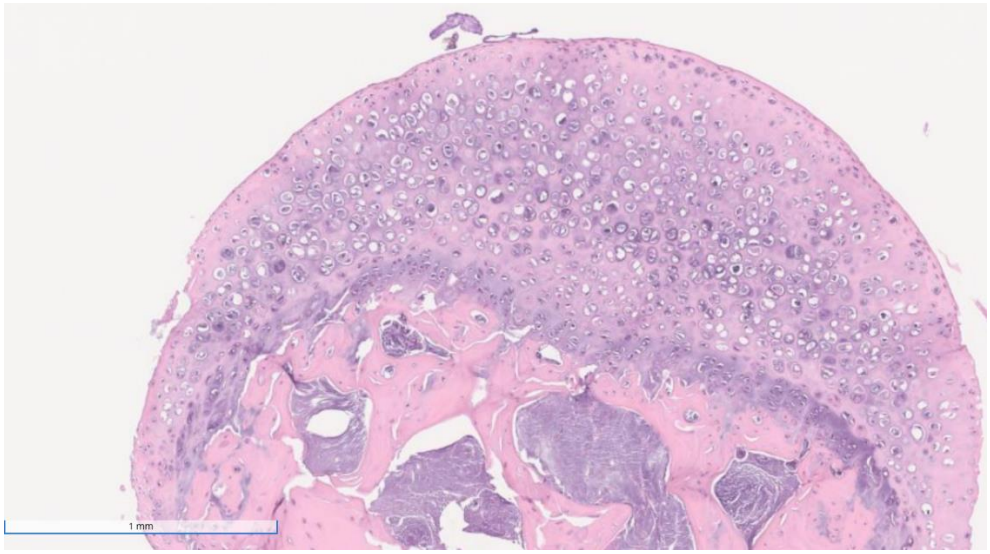

Figure 4-57. The cartilage of OFD bone.

4.6 Results Summary

The Raman spectra analysis showed that the Mn/Mx ratio was higher in normal bone compared to the knockout. Additionally, 2D mapping of mineral composition indicated differences in appetite between normal and knockout bones, with abnormal crystal appetites observed in the knockout bones. Further research with larger samples is needed to confirm this hypothesis.

Micro-CT scans revealed that knockout bones have lower bone density compared to normal bones. Furthermore, normal bones exhibited lower cortical density, but higher trabecular density compared to knockout bones, which is crucial in distinguishing bone development.

SEM/EDS elemental composition analysis showed differences between normal and knockout bones, although this method is less definitive than others. The Vickers Hardness test demonstrated that knockout bones are weaker than normal bones due to their lower mineral content.

Calculation of the mineral-to-matrix ratio showed an increase in normal bones and a decrease in knockout bones, suggesting a decrease in calcium phosphate mineralization in the knockout bones, making them weaker and more prone to breakage. These findings align with the Vickers Hardness test results.

Histological results revealed significant differences between normal bones and OFD bones in terms of bone marrow, number of osteocytes, and lacunae. Additionally, differences in trabecular thickness and number between OFD bones and normal bones were consistent with the micro-CT results also the histology results consistent with micro-CT results about the OFD knockout bone are more fragile than the normal bones.

Table 4-9. Work model diagnosis test related to NF1 Knockout bones.

	Normal Bone	**NF1 Knockout Bone**	**Osteoporosis (OP)**	**Ratio knockout to Normal**	**Ratio OP to Normal**	**NF1 Score**	**NF1 Condition**	**OP Score**	**OP Condition**
AVE Bone mineral Density	1064	983	554-635	1.1	0.5	<1.1 Disease >=1 Normal		<0.5 Disease >=1 Normal	
AVE Mn/Mx	6.8	5.3	2.3-3.4	0.7	0.8	0.7-0.8 OP		0.5-0.8 OP	
HV	49-75	33-62	--	0.8	-				

Table 4-10. Work model diagnosis test related to OFD Knockout bones.

	Normal Bone	OFD Knockout Bone	Osteoporosis (OP)	Ratio knockout to Normal	Ratio OP to Normal	OFD Score	OFD Condition	OP Score	OP Condition
AVE Bone mineral Density	1064	1019	554-635	0.9	0.5	<0.9 Disease >=1 Normal 0.6-0.9 OP		<0.5 Disease >=1 Normal 0.5-0.8 OP	
AVE Mn/Mx	6.8	6	2.3-3.4	0.8	0.8				
HV	49-75	41-66	--	0.8	-				

Chapter 5 Conclusion

5.1 Conclusion

The findings of this study shed light on the impact of OFD (Osteofibrous Dysplasia) and NF1 (Neurofibromatosis type 1) diseases on bone quality and structure in children. The research has provided valuable insights into the significant susceptibility of patients with these conditions to a high risk of fractures and further osteoporosis.

Despite the limitations in sample size, animal subjects, and scope, the study has shown promising potential in utilizing different Raman modalities and measurement approaches for the diagnosis of OFD and NF1. The mineral-to-matrix ratios were found to be lower in both OFD and NF1 knockout bones, with NF1 knockout bones exhibiting the lowest ratios. The practical application of Raman for the diagnosis will depend upon the analysis of the biopsy samples, pending further development of non-invasive Raman methods such as Raman photoacoustic spectroscopic imaging.[43]

Additionally, disruptions in microstructure were observed in OFD and NF1 knockout bones, as indicated by 2D Raman spectral mapping. These findings open new possibilities for the potential usefulness of 2D Raman for histology and pathology diagnosis, offering simpler sample preparation methods. Furthermore, Micro-CT measurements of mineral density and microstructure showcased consistent differences between normal bones, OFD knockout bones, and NF1 knockout bones, corroborating the results obtained from other measurements, including microhardness.

The SEM/EDS measurement of the elemental composition also contributed to our understanding by accounting for the presence of excess phosphate, potentially in the form of pyrophosphates, implicated in bone disorders in OFD and NF1 knockout bones. Moreover, the variation in Mn/Mx and apatite crystal types revealed through Raman spectra and 2D Raman mapping provides new insights that may aid in understanding the etiology of OFD and NF1 diseases.

The histology results revealed significant differences in the OFD knockout bone compared to the normal bones. There was an increase in the number of empty lacunae in the OFD knockout bones, alongside a different shape of trabecular bone and possible

trabeculations of cortical bone. This suggests that the OFD knockout bones are weaker and have a higher risk of fracture compared to the normal bones.

This research resulted in three new findings: 1) evidence from Raman spectra for abnormalities in apatite mineralization in OFD and NF1 knockout bones; 2) evidence from comparison of Raman and EDS/SEM analysis for elevated inorganic mineral forms of calcium and phosphorous in OFD and NF1 knockout bones, which provides support for a mechanism reported in the literature; 3) evidence from 2D Raman mapping for disorganization of bone microstructure in OFD and NF1 knockout bones, which provides a possible mechanism for reported differences in bone density and mineral to matrix ratios between normal, OFD and NF1 affected bone. Also, 2D Raman spectral mapping shows disruptions in bone microstructure consistent with that observed with histology staining. This opens the possibility of the usefulness of 2D Raman for histology and pathology diagnosis, with the benefits of much simpler sample preparation.

These discoveries underscore the critical need for further research to fully optimize the working model and pave the way for the early diagnosis and comprehensive understanding of the effect of OFD and NF1 on bone composition and mineral-to-matrix ratio, thereby potentially enabling quantification of fracture risk and prediction of fracture occurrence.

References

1. Baig, M-A., Bacha, D. Histology, Bone. In: Stat Pearls [Internet]. Treasure Island (FL): Stat Pearls Publishing, (2024).
2. Kelly, P-J. Anatomy, physiology, and pathology of the blood supply of bones. J Bone Joint Surg Am. ;50(4):766-83, (1968).
3. Rockville, (MD). Diseases of Bone. A Report of Office of the Surgeon General (US). Bone Health and Osteoporosis.; (3): (2004).
4. Yoshida, S., Watanuki, M., Hayashi. K., Hosaka. M., Hagiwara, Y., Itoi, E., Hatori M, Hitachi S, Watanabe M. Osteofibrous dysplasia arising in the humerus: A case report. Rare Tumors., (2018).
5. Park, Y-K., Unni, K-K., McLeod, R-A., Pritchard, D-J. Osteofibrous dysplasia: clinicopathologic study of 80 cases. Hum Pathol., 24(12): P1339–47, (1993).
6. Liu, R., Tong, L., Wu, H. et al. Osteofibrous dysplasia: a narrative review. J Ortho Surg Res 19, 204, (2024).
7. Gleason, B-C., et al. Osteofibrous dysplasia and adamantinoma in children and adolescents: a clinicopathologic reappraisal. Am J Surg Pathol.;32(3): P363-76, (2008).
8. Le, C., Bedocs, P-M. Neurofibromatosis. In: Stat Pearls [Internet]. Treasure Island (FL): Stat Pearls Publishing;(2024).
9. Lee, T-J., Chopra, M., Kim, R-H., Parkin, P-C., Barnett-Tapia, C. Incidence and prevalence of neurofibromatosis type 1 and 2: a systematic review and meta-analysis. Orphanet J Rare Dis.,18(1): P 292, (2023).
10. Rasmussen, S-A., Yang, Q., Friedman, J-M. Mortality in neurofibromatosis 1: an analysis using U.S. death certificates. Am J Hum Genet., 68(5): P 1110-8, (2001).
11. Lee, C-A., Einhorn, Th- A. Chapter 1 - The Bone Organ System: Form and Function, Editor(s): Marcus, R., Feldman, D., Kelsey, J. Osteoporosis (Second Edition), Academic Press., P 3-20, (2001).
12. Ortho Info. American Academy of Orthopedic Surgeons. Healthy Bones at Every Age. Archived from the original in 2022. Retrieved (2023).
13. de Buffrénil, V., et al. Vertebrate skeletal histology and paleohistology. First ed. Boca Raton, FL: CRC Press., P 825, (2021).
14. Ott, S-M. Cortical or Trabecular Bone: What's the Difference? American J Nephrol., P 47:373–375, (2018).
15. Zhang, X-Y., Fang, G., Zhou, J. Additively Manufactured Scaffolds for Bone Tissue Engineering, and the Prediction of their Mechanical Behavior. A Review Materials., P 10-50, (2017).
16. Sarker, A., Leary, M., Fox, K. Metallic additive manufacturing for bone-interfacing implants. Bio interphases., P 15, (2020).
17. Parfitt, A-M. Misconceptions (2): turnover is always higher in cancellous than in cortical bone. Bone., 30: P 807–809, (2002).

18. Johannesdottir, F., et al. Comparison of non-invasive assessments of strength of the proximal femur. Bone.,105: P 93–102, (2017).
19. Goda, I., Ganghoffer, J-F. Modeling of anisotropic remodeling of trabecular bone coupled to fracture. Archive of Applied Mechanics., 88: P 2101–2121, (2018).
20. Feng, X. Chemical and Biochemical Basis of Cell-Bone Matrix Interaction in Health and Disease. Curr. Chem. Biol., 3: P189–196, (2009).
21. Šromová, V., Sobola, D., Kaspar, P-A. Brief Review of Bone Cell Function and Importance. Cells.,12(21): P 25-76, (2023).
22. Lü, X., Wang, J., Li B., Zhang, Z., Zhao, L. Gene expression profile study on the Osteo inductive effect of natural hydroxyapatite. J. Biomed. Mater. Res. Part A., 102: P 2833–2841, (2014).
23. Albrektsson, T., Johansson, C. Osteo induction, osteo conduction and osseointegration. Eur. Spine J.,10: P96–101, (2001).
24. Dalla, P-A. Biomechanical Characteristics of the Bone. Hum. Musculoskeletal Bio mech., P 61-86, (2012).
25. Clarke, B. Normal bone anatomy and physiology. Clin. J. Am. Soc. Nephrol., 3: P 131–139, (2008).
26. Mescher, L-A. 15th ed. McGraw Hill/Medical; Chicago, IL, USA: Junqueira's Basic Histology Text and Atlas., (2018).
27. Wittig, N-K., Birkedal, H. Bone hierarchical structure: spatial variation across length scales. Acta Crystallogr., Sect. B: Struct. Sci., Cryst. Eng. Mater., 78: P 305, (2022).
28. Liu, Z., Zhang, Z., Ritchie, R-O. Structural Orientation and Anisotropy in Biological Materials: Functional Designs and Mechanics. Adv. Funct. Mater., 30, (2020).
29. Reznikov, N., Steele, J-A- M., Fratzl, P., Stevens, M-M. A materials science vision of extracellular matrix mineralization. Nat. Rev. Mater. 1: 16041 (2016).
30. Rodriguez-Palomo, A., at el. Bone Hierarchical Structure: Heterogeneity and Uniformity. Advanced Functional Materials., (2023).
31. Brat, Z., Wallace, J. Microcomputed Tomography Applications in Bone and Mineral Research. Advances in Computed Tomography. 2: P 121-127, (2013).
32. Mohamed, A-M. An overview of bone cells and their regulating factors of differentiation. Malays J Med Sci., 15(1): P 4-12, (2008).
33. . Biga, L-M., et al. Anatomy & Physiology: Bone structure. 1st edition, Open Stax, (2019).
34. Dwek, J-R. The periosteum: What Is it, where is it, and what mimics it in its absence? Skelet. Radiol., 39: P319–323, (2010).
35. Ascenzi, M-G., Roe, A-K. The osteon: The micromechanical unit of compact bone. Front. Biosci., 17: P1551–1581, (2012).
36. Jacobs, C-R. The mechanobiology of cancellous bone structural adaptation. J. Rehabil. Res. Dev., 37: P 209–216. (2000).
37. Baig, M-A., Bacha D. Histology, Bone. Stat Pearls., Treasure Island, FL, USA: (2021).
38. Clarke, B. Normal bone anatomy and physiology. Clin. J. Am. Soc. Nephrol. CJASN., 3: P131, (2008).
39. Nahian, A., Chauhan, P-R. Histology, Periosteum and Endosteum. Stat Pearls., Treasure Island, FL, USA: (2021).
40. Gianakos, A., Ni A., Zambrana L., Kennedy J.G., Lane J.M. Bone marrow aspirate concentrate in animal long bone healing: An analysis of basic science evidence. J. Orthop. Trauma.,30: P 1–9 (2016).

41. Fraile-Martínez, O., et al. Applications of Polymeric Composites in Bone Tissue Engineering and Jawbone Regeneration. Polymers (Basel)., 13(19): P 34-29, (2021).
42. Le, B-Q., Nurcombe, V., Cool, S-M. Van Blitterswijk, C-A., de Boer, J., LaPointe, V-L-S. The Components of bone and what they can teach us about regeneration. Materials.,11: P 14, (2018).
43. Meletis, E-I., Sarker, F., Shah, M., Tibbals, H-F., Yadev,S. Nanoscale Characterization of Bone: Mechanical, Ultrasound, Electrical, Spectroscopic Methods in Nanoengineering, Quantum Science, and, Nanotechnology Handbook., First Edition, Sergey E. Lyshevski, editor, CRC Taylor & Francis, Boca Raton, Fl., Chapter 15: P 311-350, (2019).
44. Breeland, G., Sinkler, M-A., Menezes, R-G. Embryology, Bone Ossification. Treasure Island (FL): StatPearls Publishing., (2024).
45. Rye, C., Wise, R., Jurukovski, V., DeSaix, J., Choi, J., Avissar, Y. Biology. OpenStax., (2016).
46. Salhotra, A., Shah, H-N., Levi, B. et al. Mechanisms of bone development and repair. Nat Rev Mol Cell Biol., 21: P 696–711 (2020).
47. Clark, M-A., Choi, J., Douglas, M. Biology 2e. OpenStax Biology 2nd Edition., 13: 978-1-947172-52-4, (2018).
48. Molnar, C., Gair, J. Concepts of Biology – 1st Canadian Edition. BCcampus., 978-1-989623-99-2, (2015).
49. Achar, S., Yamanaka, J. Apophysitis and Osteochondrosis: Common Causes of Pain in Growing Bones. Am a Fam Physician., 15;99(10): P 610-618, (2019).
50. Seiwert, C., et al. Human Biology. Goodwin University. Biology, life sciences., (2019).
51. de Lima Augusto, A-C., et al. Imaging Review of Normal and Abnormal Skeletal Maturation. Radio Graphics., 42: 3, (2022).
52. Rossbach, H-C. Hereditary and familial syndromes of bone and blood. Genetic pathways, diagnostic pitfalls. Fetal and Pediatric Pathology., 26(1): P 1-16, (2007).
53. Teti, A., Teitelbaum, S-L. Congenital disorders of bone and blood. Bone., 109: P 78-103(2018).
54. Wilt, F-H. Developmental biology meets materials science: Morphogenesis of biomineralized structures. Dev. Biol., 280: P 15-25, (2005).
55. Buehler, M-J. Nano- and micromechanical properties of hierarchical biological materials and tissues. J. Mat. S., 42: P 8765–8770, (2007).
56. Abel, R., Hansen U., Cobb, J. Bone nano-mechanics: the big unknown. Orthopaedic Proc., 99-B: (2018).
57. Wang, Y-T., Chang, S-Y., Huang, Y-C., Tsai, T-C., Chen, C-M., Lim, C-T. Nanomechanics insights into the performance of healthy and osteoporotic bones. Nano Lett., 13:P 5247-54, (2013).
58. Morgan, E-F., Gerstenfeld, L-C. The bone organ system: form and function. Chapter 2, Editor(s): David W. Dempster, Jane A. Cauley, Mary L. Bouxsein, Felicia Cosman, Marcus and Feldman's Osteoporosis, Fifth Edition, Academic Press., P 15-35, (2021).
59. Tzaphlidou, M. Bone Architecture: Collagen Structure and Calcium/Phosphorus Maps. J. Biol. Phys, 34:P 39–49, (2008).
60. Burton, J., et al. Bone chemistry and trace element analysis in biological anthropology of the human skeleton, 2nd edition ed., P 443-460, (2008).
61. Peacock, M. Calcium Metabolism in Health and Disease. CJASN, 5, no. Supplement 1: P 23-30, (2010).

62. Dorozhkin, S-V., Matthias, E. Biological and medical significance of calcium phosphate. Angew. Chem. Int. Ed., 41, 17: P 3130-3146, (2002).
63. Burr, D-B. The contribution of the organic matrix to bone's material properties. Bone, 31,1: P8-11, (2002).
64. Burr, D-B. The contribution of the organic matrix to bone's material properties. Bone, 31,1: P8-11, (2002).
65. Yerramshetty, J-S., Ozan, A. The associations between mineral crystallinity and the mechanical properties of human cortical bone. Bone, 42(3): P 476-482, (2008).
66. Vokes, T., Favus, M. Noninvasive assessment of bone structure. Curr. Osteo. Rep., 1(1): P 20-24, (2003).
67. Link, T-M., Osteoporosis imaging: state of the art and advanced imaging. Radiology, 263(1): P 3-17, (2012).
68. Paschalis, E-P., Mendelsohn, R., Boskey, A-L. Infrared assessment of bone quality: a review. Clin. Orthop. Relat. Res., 469(8): P 2170-2178, (2011).
69. Matousek, P., Draper, E-R-C., Goodship, A-E., Clark, L-P. Noninvasive Raman spectroscopy of Human Tissue In Vivo. Appl. Spectroscope., 60 (7): P 758–763, (2006).
70. Lee, R-S., Weitzel, S., Eastwood, D-M., Monsell, F., Pringle, J., Cannon, S-R., Briggs, T-W. Osteofibrous dysplasia of the tibia. Is there a need for a radical surgical approach? Bone Joint Surg Br.;88(5): P 658-64, (2006).
71. Ciesielski, T-H., Sirugo, G., Iyengar, S-K. et al. Characterizing the pathogenicity of genetic variants: the consequences of context. Genom. Med. 9(3): (2024).
72. Takahiro, G., et al. Osteofibrous dysplasia of the ulna. Journal of Orthopaedic Science., 6: P 608-611, (2001).
73. Liu, Y-B., Zou, T-M. Giant monostotic Osteofibrous dysplasia of the ilium: A case report and review of the literature. World J Clin Cases.; 6(14): P 830-835, (2018).
74. Jung, J-Y., Jee, W-H., Hong, S-H., Kang, H-S. et al. MR findings of Osteofibrous dysplasia. Korean J Radiol.;15(1): P 114-22, (2014).
75. Saber, A-Y, Patel, B-C. Osteofibrous Dysplasia. In: Stat Pearls [Internet]. Treasure Island (FL): Stat Pearls Publishing; (2024).
76. Ozaki, T., Hamada, M., Sugihara, S., Kunisada, T., Mitani, S., Inoue, H. Treatment outcome of Osteofibrous dysplasia. Pediatr Orthop B. 7(3): P 199-202, (1998).
77. Scholfield, D-W., et al. Does Osteofibrous dysplasia progress to adamantinoma and how should they be treated? Bone Joint J.; 99-B (3): P 409-416, (2017).
78. Rios, J-J., Wise, C-A., Robertson, S-P. Mutations Preventing Regulated Exon Skipping in MET Cause Osteofibrous Dysplasia. Am J Hum Genet. 3; 97(6): P 837-47, (2015).
79. Park, J-W., Lee, C., Han, I., Cho, H-S, Kim, H-S. Optimal Treatment of Osteofibrous Dysplasia of the Tibia. J Pediatr Orthop; 38(7): P 404-410, (2018).
80. Kang, E., Kim, Y-M., Choi. Y., Lee, Y., Kim, J., Choi, I-H., Yoo, H-W., Yoon, H-M., Lee, B-H., Whole-body MRI evaluation in neurofibromatosis type 1 patient younger than 3 years old and the genetic contribution to disease progression. Orphanet J Rare Dis. 29;17(1): P 24, (2022).
81. Bergoug, M., Doudeau, M., Godin, F., Mosrin, C., Vallée, B., Bénédetti, H. Neurofibromin Structure, Functions and Regulation. Cells. 9(11): P 23-65, (2020).
82. Williams, V-C., Lucas, J., Babcock, M-A., Gutmann, D-H., Korf, B., Maria, B-L. Neurofibromatosis type 1 revisited. Pediatrics. 123(1): P 124-33, (2009).
83. Gutmann, D-H., Ferner, R-E., Listernick, R-H., Korf, B-R., Wolters, P-L., Johnson, K-J. Neurofibromatosis type 1. Nat Rev Dis Primers. 3: P 170-04, (2017).

84. Kunc, V., Venkatramani, H., Sabapathy, S-R. Neurofibromatosis 1 Diagnosed in Mother Only after a Follow-up of Her Daughter. Indian Journal of Plastic Surgery, 52 (2): P 260, (2019).
85. Ferner, R-E., Huson, S-M., Thomas, N., Moss, C., Willshaw, H., Evans, D-G., Upadhyaya, M., Towers, R., Gleeson, M., Steiger, C., Kirby, A. Guidelines for the diagnosis and management of individuals with neurofibromatosis 1. J Med Genet. 44(2): P 81-8, (2007).
86. Pannier, S. Congenital pseudarthrosis of the tibia. Orthop Traumatol Surg Res.97(7): P 750-61, (2011).
87. Bäumlein, M., Hanke, A., Gueorguiev, B., Nerlich, M., Liodakis, E., Perren, T., Rillmann, P., Ryf, C., Loibl, M. Long-term outcome after surgical treatment of intra-articular tibial plateau fractures in skiers. Arch Orthop Trauma Surg. 139(7): P 951-959, (2019).
88. Gross, A-M., Plotkin, S-R., Watts, N-B., Fisher, M-J., Klesse, LJ., Lessing, A-J., McManus, M-L., Larson, A-N., Oberlander, B., Rios, J-J., Sarnoff, H., Simpson, B-N., Ullrich, N-J., Stevenson, D-A. Potential endpoints for assessment of bone health in persons with neurofibromatosis type 1. Clin Trials. 21: P 29-39, (2024).
89. Gutmann, D., Ferner, R., Listernick, R. et al. Neurofibromatosis type 1. Nat Rev Dis Primers.; 3: P 170-04, (2017).
90. Elefterious, F., Kolanczyk, M., Schindeler, A., et al. Skeletal abnormalities in neurofibromatosis type 1: approaches to therapeutic options. Am J Med Genet A. 149A (10): P 2327-38, (2009).
91. de la Croix Ndong, J., et al. Asfotase-alpha improves bone growth, mineralization, and strength in mouse models of neurofibromatosis type-1. Nat. Med. 20: P 904–910, (2014).
92. Elefteriou, F. et al. ATF4 mediation of NF1 functions in osteoblast reveals a nutritional basis for congenital skeletal dysplasia. Cell Metab.; 4: P 441–451, (2006).
93. Lammert, M. et al. Decreased bone mineral density in patients with neurofibromatosis 1. Osteoporos. Int.; 16: P 1161–1166, (2005).
94. Zessis, N-R., Gao, F., Vadlamudi, G., Gutmann, D-H., Hollander, A-S. Height growth impairment in children with neurofibromatosis type 1 is characterized by decreased pubertal growth velocity in both sexes. J. Child Neurol.; 33(12): P 762–766, (2018).
95. Clementi, M. et al. Neurofibromatosis type 1 growth charts. Am. J. Med. Genet.; 87(4): P 317–323, (1999).
96. Caffarelli, C. et al. Quantitative ultrasound and dual-energy X-ray absorptiometry in children and adolescents with neurofibromatosis of type 1. J. Clin. Densitom.; 13(1), 77–83 (2010).
97. Seitz, S., et al. High bone turnover and accumulation of osteoid in patients with neurofibromatosis 1. Osteoporos. Int., 21: P 119–127, (2010).
98. Riccardi, V-M. Neurofibromatosis: Clinical heterogeneity. Curr. Probl. Cancer. 7(2): P 1–34, (1982).
99. Lee, P-H., Macfarlane, D-J., Lam, T-H., Stewart, S-M. Validity of the International Physical Activity Questionnaire Short Form (IPAQ-SF): A systematic review. J. Behav. Nutr. Phys. Act. 8: P 115, (2011).
100. Willet, W-C. et al. Reproducibility and validity of a semiquantitative food frequency questionnaire. Am. J. Epidemiol. 122(1): P 51–65, (1985).
101. Salari, N., Ghasemi, H., Mohammadi, L., Behzadi, M-H, Rabieenia, E., Shohaimi, S., Mohammadi, M. The global prevalence of osteoporosis in the world: a comprehensive systematic review and meta-analysis. J Orthop Surg Res.;16(1): P 609, (2021).

102. Rios, J-J., et al. A molecular basis for neurofibroma-associated skeletal manifestations in NF1. Genet Med. 22(11): P1786-1793, (2020).
103. Dombi, E., Baldwin, A., Marcus, L-J., et al. Activity of Selumetinib in Neurofibromatosis Type 1-Related Plexiform Neurofibromas. N Engl J Med. 375(26): P 2550–2560, (2016).
104. Gross, A-M., Wolters, P-L., Dombi, E., et al. Selumetinib in Children with Inoperable Plexiform Neurofibromas. N Engl J Med, (2020).
105. Miller, S-J., Jessen, W-J., Mehta, T., et al. Integrative genomic analyses of neurofibromatosis tumors identify SOX9 as a biomarker and survival gene. EMBO Mol Med.,1(4): P236–248 (2009).
106. Murshed, M. Mechanism of Bone Mineralization. Cold Spring Harb Perspect Med. 3, 8(12): (2018).
107. Rey, C., Miquel, J-L., Facchini, L., Legrand, A-P., Glimcher, M-J. Hydroxyl groups in bone mineral. Bone.,16: P 583–586 (1995).
108. Rey, C., Combes, C., Drouet, C., Glimcher, M-J. Bone mineral: Update on chemical composition and structure. Osteoporos Int., 20: P 1013–1021, (2009).
109. Yan, X., et al. The mechanism of biomineralization: Progress in mineralization from intracellular generation to extracellular deposition. J Dent Sci Rev. 59: P 181-190, (2023).
110. Rios, J-J., et al. MEK inhibitors for neurofibromatosis type 1 manifestations: Clinical evidence and consensus. Neuro Oncol. 2, 24(11),1845-1856 (2022).
111. Elefteriou, F., et al. Skeletal abnormalities in neurofibromatosis type 1: Approaches to therapeutic options. Am J Med Genet Part A.; 149A: P 2327–2338, (2009).
112. Orhan, K. Introduction to Micro-CT Imaging. In: Orhan, K. (eds) Micro-computed Tomography (micro-CT) in Medicine and Engineering. Springer, Cham, (2020).
113. Boerckel, J-D, Mason, D-E, McDermott, A-M, Alsberg, E. Microcomputed tomography: approaches and applications in bioengineering. Stem Cell Res Ther. 29; 5(6): P 144, (2014).
114. Bouxsein, M-L., Boyd, S-K., Christiansen, B-A., Guldberg, R-E, Jepsen, K-J., Muller, R. Guidelines for assessment of bone microstructure in rodents using micro-computed tomography. J Bone Miner Res. 25(7): P 1468–1486, (2010).
115. Kim, Y., Brodt, M-D., Tang, S-Y., Silva, M-J. Micro-CT for Scanning and Analysis of Mouse Bones. Methods Mol Biol.; 22(30): P 169-198, (2021).
116. Ruchita, S., Das, Y-K., Agrawal. Raman spectroscopy: Recent advancements, techniques and applications, Vibrational Spectroscopy, 57(2): P163-176 (2011).
117. Bumbrah, G., Sharma, R-M. Raman spectroscopy – Basic principle, instrumentation and selected applications for the characterization of drugs of abuse, Egyptian Journal of Forensic Sciences, 6(3): P 209-215 (2016).
118. Skoog, D-A., Holler, F-J., Crouch, S-R. Principles of instrumental analysis. Cengage Learning 6th ed., (2006).
119. Willard, H-H., Meritt. et al. Instrumental methods of analysis. CBS Publisher & Distributors, 7th ed., New Delhi, (1988).
120. Kunxiang, L., et al. Raman Spectroscopy: A Novel Technology for Gastric Cancer Diagnosis,8(10): P 5659, (2022).
121. Qiang, Tu., Chang Diagnostic applications of Raman spectroscopy., Nanomedicine: nanotechnology, biology, and medicine, 8(5) P 545-58, (2012).
122. Wei, D., Chen, S., Liu, Q. Review of fluorescence suppression techniques in Raman spectroscopy. Appl, Spectrosc, Rev. (50): P 387-406, (2015).

123. Tomasz Buchwald, M., Kozielski, M., Szybowicz, M. Determination of Collagen Fibers Arrangement in Bone Tissue by Using Transformations of Raman Spectra. Hindawi Publishing Corporation Spectroscopy: An International Journal. 27: P 107–117,(2012).
124. Awonusi, A., Morris, M-D., Tecklenburg, M-J. Carbonate assignment and calibration in the Raman spectrum of appetite. Calcif. Tissue Int., 81(1): P 46-52, (2007).
125. Yerramshetty, J-S., Ozan, A. The associations between mineral crystallinity and the mechanical properties of human cortical bone. Bone, 42(3): P 476-482, (2008).
126. Mandair, G-S., Morris, M-D. Contributions of Raman spectroscopy to the understanding of bone strength. Bone key Rep. 4: 620 (2015).
127. Jones, R-R., Hooper, D-C., Zhang, L., Wolverson, D., Valev, V-K. Raman Techniques: Fundamentals and Frontiers. Nanoscale Res Lett. 12, 14(1): 231(2019).
128. Wang, F., Zheng, L., Theopold, J., Schleifenbaum, S., Heyde, C-h., Osterhoff, G. Methods for bone quality assessment in human bone tissue: a systematic review. Journal of Orthopedic Surgery and Research. 17: P 174, (2022).
129. Rios, J., et al., Genetic association and characterization of FSTL5 in isolated clubfoot. Hum Mol Genet. 29(22): P 3717-3728, (2021).
130. Krumeich, F. Properties of Electrons, their Interactions with Matter and Applications in Electron Microscopy. Laboratory of Inorganic Chemistry, ETH Zurich, Zurich, Switzerland, (2011).
131. Zhou, W., Wang, Z-L. Scanning Microscopy for Nanotechnology-Techniques and Applications. Springer, (2006).
132. Leng, Y. Materials Characterization-Introduction to Microscopic and Spectroscopic Methods. John Wiley & Sons, (2008).
133. Ameruddin, A. Growth and Characterization of Gold-seeded Indium Gallium Arsenide Nanowires for Optoelectronic Applications, THES, (2015).
134. Guerri, S., Mercatelli, D., Aparisi Gómez, M. P., Napoli, A., Battista, G., Guglielmi G., Bazzocchi, A. Quantitative imaging techniques for the assessment of osteoporosis and sarcopenia. Quant. Imaging Med. Surg., 8(1): P 60-85, (2018).
135. Kendler, D-L., Compston, J., Carey, J-J., Wu, C-H., Ibrahim, A., Lewiecki, E-M. Repeating Measurement of Bone Mineral Density when Monitoring with Dual-energy X-ray Absorptiometry: ISCD Official Position," J. Clin. Densitom., 22(4): P 489-500, (2019).
136. Kanis, J-A., Harvey, N-C., Johansson, H., Liu, E., Vandenput, L., Lorentzon, M., Leslie, W-D., McCloskey, E-V. A decade of FRAX: how has it changed the management of osteoporosis? Aging. Clin. Exp. Res., 32(2): P 187-196, (2020).
137. Schmidt, G-P., Schoenberg, S-O., Reiser, M-F., Baur-Melnyk, A. Whole-body MR imaging of bone marrow. Eur. J. Radiol., 55(1): P 33-40, (2005).
138. Lee, D., Velander, J., Blokhuis, T-J., Kim, K., Augustine, R. Preliminary study on monitoring the progression of osteoporosis using UWB radar technique in distal femur model. Electron. Lett., 52: P 589-590, (2016).
139. Feng, T., Kozloff, K., Cao, M., Cheng, Q., Yuan, J., Wang, X. Study of photoacoustic measurement of bone health based on clinically relevant models. Proc. SPIE, 4(F): P 89-96, (2016).
140. Zhang, X., Specht, A-J., Wells, E., Weisskopf, M-G., Weuve, J., Nie, L-H. Evaluation of a portable XRF device for in vivo quantification of lead in bone among a US population. Sci. Total Environ., 753: P 142351, (2021).

141. Nyman, J-S, Granke, M., Singleton, R-C, Pharr, G-M. Tissue-level mechanical properties of bone contributing to fracture risk. Curr Osteoporos Rep. Springer US. 14(4): P 138–50, (2016).
142. McKee, T-J., Perlman, G., Morris M., Komarova, S-V. Extracellular matrix composition of connective tissues: a systematic review and meta-analysis. Sci. Rep., 9(1): P 10542, (2019).
143. Ghorbani, S., Hosseini, S-H., Ghasemi, E. et al. A review of rock hardness testing methods and their applications in rock engineering. Arab J Geosci 15: P 1067, (2022).
144. Smith, R-L., Sandland, G-E. An Accurate Method of Determining the Hardness of Metals, with Particular Reference to Those of a High Degree of Hardness. Proceedings of the Institution of Mechanical Engineers, I: P 623–641, (2022).
145. Alhashmy, Hasan. Fabrication of Aluminium Matrix Composites (AMCs) by Squeeze Casting Technique Using Carbon Fiber as Reinforcement. (2012).
146. Hodgkinson, R., Currey, J-D., Evans, G-P. Hardness is an indicator of the mechanical competence of cancellous bone. J Orthop Res, 7: P 754–758, (1989).
147. Zysset, P-K., Guo, X-E., Hoffle, C-E., Moore, K-E., Goldstein, S-A. Elastic modulus and hardness of cortical and trabecular bone lamellae measured by nanoindentation in the human femur. J Biomech, 32: P 1005–1012, (1999).
148. Weaver, J-K. The microscopic hardness of bone. J Bone Joint Surg Am, 48: P 273–288, (1966).
149. Katoh, T., Griffin MP., Wevers, H-W., Rudan J. Bone hardness testing in the trabecular bone of the human patella. J Arthroplasty, 1996, 11: 460–468.
150. Nakabayashi, Y., Wevers, H.-W., Cooke, T-D, Griffin, M. Bone strength and histomorphometry of the distal femur. J Arthroplasty, 9: P 307–315, (1994).
151. Alturkistani, H-A., Tashkandi, F-M., Mohammedsaleh, Z-M. Histological Stains: A Literature Review and Case Study. Glob J Health Sci. 25; 8(3) :P 72-9, (2015).
152. Black, J. Microbiology: Principles and exploration. John Wiley Sons. 8th ed. P 68, (2012).
153. Musumeci, G. Past, present and future: overview on Histology and histopathology. J Histol Histopathol. 1: P 5, (2014).
154. Nadworny, P-L, Wang, J-F, Tredget, E., Robert, E. Anti-inflammatory activity of nanocrystalline silver-derived solutions in porcine contact dermatitis. Burrel J. Inflammation. (2010).
155. Ntziachristos, V., Going deeper than microscopy: the optical imaging frontier in biology. Nat Methods. 7: P 603–614, (2010).
156. Rotimi, O., Cairns, A., Gray, S., Moayyedi, P., Dixon, M-F. Histological identification of Helicobacter pylori: comparison of staining methods. Clin Pathol. 2000 53: P 756–759, (2014).
157. Titford, M. The long history of hematoxylin. Biotechnic & Histochemistry. 80 (2): P 73–80. (2005).
158. Smith, C. Our debt to the logwood tree: the history of hematoxylin. MLO Med Lab Obs. 38 (5): P 18, 20–2, (2006).
159. Dapson, R-W, Horobin, R-W. Dyes from a twenty-first-century perspective. Biotech Histochem. 84 (4): 135–7, (2009).
160. Wittekind, D. Traditional staining for routine diagnostic pathology including the role of tannic acid. 1. Value and limitations of the hematoxylin-eosin stain. Biotech Histochem. 78 (5): P 261–70 (2003).
161. Schulte, E-K. Standardization of biological dyes and stains: pitfalls and possibilities. Histochemistry. 95 (4): P 319–28, (1991).

162. Stevens, A. The Theory and Practice of Histological Techniques (2nd ed.). Longman Group Limited. P 109, (1982).
163. Mariano, S-H. et al. Atlas of Histology with Functional Correlations. 11th ed. Philadelphia: Lippincott Williams & Wilkins, (2008).
164. Robbins, Stanley L et al. Pathologic Basis of Disease. 9th ed. Philadelphia, PA: Saunders Elsevier, 2015.
165. Baig, M-A., Bacha, D. Histology, Bone. In: Stat Pearls [Internet]. Treasure Island (FL): Stat Pearls Publishing; (2024).